Optimal Configuration of a Planet-Finding Mission Consisting of a Telescope and a Constellation of Occulters

Egemen Kolemen

A Dissertation
Presented to the Faculty
of Princeton University
in Candidacy for the Degree
of Doctor of Philosophy

Recommended for Acceptance
by the Department of
Mechanical and Aerospace Engineering
Adviser: N. Jeremy Kasdin

SEPTEMBER 2008

Abstract

Occulter-based telescopy offers a promising new terrestrial planet-finding methodology that involves the formation flying of a conventional space telescope with a large external occulter, which will block the light of a star and allow imaging of its dim, close-by planetary companion. Recent advances in shaped-pupil technology have enabled the design of occulters that have superior diffraction performance and that can be manufactured easily. This approach is attractive because it eliminates the precision-optical requirements of the alternative coronagraphic or interferometric approaches. However, it introduces new scientific challenges in the area of precise dynamics and control, which is the topic of this dissertation.

Due to the large distances between satellites, realignment is fuel intensive, which increases the mission cost and reduces its lifetime. In order to overcome this problem, this dissertation focuses on the trajectory design of the mask satellite and conducts an optimization study to select the order and timing of imaging sessions.

The optimal configuration of satellite formations consisting of a telescope and multiple occulters around Sun-Earth L2 Halo orbits is studied first. Focusing on the Quasi-Halo orbits, which are of interest for fuel-free occulter placement, the phase space around L2 is examined. The periodic orbits of interest around L2 are numerically computed and their stability properties analyzed.

Quasi-Halos are good candidates for occulter placement, as they are fuel-free orbits and have large sky coverage with respect to the Halo orbit, where the telescope is placed. With the aim of identifying these orbits, a new fully numerical method that employs multiple Poincaré sections to find quasi-periodic orbits is developed. This methodology has the advantage of very fast execution times and robust behavior near chaotic regions that leads to full convergence. Its numerical implementations for Lissajous and Quasi-Halo orbits are explained. These results are then extended from the simplified three body model to find the orbits in the real solar system that have

the same characteristics.

Trajectory optimization of the occulter motion between imaging sessions of different stars is performed using a range of different criteria and methods. This enables the transformation of the global optimization problem into a Time-Dependent Traveling Salesman Problem (TSP). The TSP is solved first for a formation consisting of a telescope and a single occulter. Then, with the insight from the dynamical analysis, multiple-occulter formations are analyzed and the global optimization is performed for the multiple-occulter case.

For a concrete understanding of the feasibility of the mission, the performance of an example spacecraft, SMART-1, is analyzed. The mission is shown to be feasible with the current technology.

Acknowledgements

It has been a great pleasure to work on this project in the Department of Mechanical and Aerospace Engineering at Princeton University. I owe a great debt of gratitude to my advisor, Jeremy Kasdin. Jeremy has been a truly inspiring mentor, allowing me significant freedom in my choice of research topics, even in my first year, and always encouraging me to explore side research interests. I deeply appreciate his advice, support, and encouragement over the years. Jeremy has the true spirit of a researcher; a quality, which I hope I will be able to emulate.

I would also like to acknowledge several other individuals who have influenced and supported me in different ways.

Pini Gurfil was very kind to host me at Technion, where, with his support, I developed the most important ideas of this thesis. I have worked well with him on several publications, and I look forward to continue to collaborate with him.

Jerry Marsden welcomed me as a visiting scholar at Caltech, where I had the opportunity to benefit from an amazing creative atmosphere.

Bob Vanderbei has shared his love for astronomy with me and sparked my interest in celestial mechanics. I enjoyed our collaboration on the rings of Saturn and I hope to work with him again on other topics in the future. Bob also very kindly agreed to read my thesis.

Dave Gates has been a wonderful boss at PPPL, where, as a postdoctoral fellow, I will continue my research on plasma control.

Clancy Rowley has been there from the first day and has helped shape my Princeton experience. I look forward to working with both Clancy and Dave next year.

Rob Stengel very kindly agreed to be my reader. He sent me extensive and much appreciated comments during what should have been his holiday. For this, I am very grateful.

Naomi Leonard taught me the foundations of controls and dynamics and has been

very supportive over the years.

As my examiner, Dick Miles asked me very interesting and challenging questions.

The members of the TPF group at Princeton have been great colleagues and friends. I will miss them all.

Finally, I would like to thank Jessica O'Leary for holding the MAE Department together.

To each of the above, I extend my deepest appreciation.

I dedicate this dissertation to Barbara Buckinx, my wonderful girlfriend, best friend, and confidante, without whom this work wouldn't have been possible, and to my loving family, my parents Nilgün and Osman and my sister Aysuda, who never cease to support me, and who are proud of me from a distance.

This thesis carries the number 3185-T in the records of the Department of Mechanical and Aerospace Engineering.

Barbara, Nilgün, Osman ve Aysuda'ya

Contents

Abstract iii

Acknowledgements v

1 Extrasolar Planet Imaging and Occulter-Based Telescopy 1

1.1 Finding Extrasolar Life 3

1.1.1 Life-Sustaining Planets 3

1.1.2 Signs of Life 3

1.1.3 Challenges associated with imaging planets in the habitable zone 5

1.2 External Occulter for Exoplanet Imaging 8

1.3 Dissertation Outline 10

2 Dynamical Analysis of the L2 Region 13

2.1 Circularly Restricted Three Body Problem - Equations of Motion . . 15

2.2 Equilibrium Points 19

2.3 Series Expansion around L2 21

2.3.1 Translation of L_2 to the origin, and rescaling 21

2.3.2 Series Expansion of the Equations 23

2.4 Analysis of the Linear Part around L2 24

2.5 High-Order Analysis (The Lindstedt-Poincaré Procedure and Halo Orbits) 27

2.6 Reduction to Center Manifold 31

2.6.1 Transformation into complex normal form 31
2.6.2 The Procedure Explained 34
2.6.3 Implementation of the Lie Series Method 35

3 Periodic Orbits of Interest around L2: Numerical Methods 38

3.1 Numerical Tools for Periodic Libration Orbits around L2 39
3.1.1 Collocation as a Numerical Tool to Find Periodic Orbits . . . 40
3.1.2 Stability Analysis of Periodic Orbits 43
3.2 Application to the Periodic Orbits of the CRTBP Around L2 46
3.2.1 Horizontal Lyapunov Orbits 49
3.2.2 Vertical Lyapunov Orbits 52
3.2.3 Halo Orbits 55

4 Multiple Poincaré Sections Method for Finding the Quasi-Halo and Lissajous Orbits 58

4.1 Procedure 60
4.1.1 Finding Invariant Tori via a Single Poincaré Section 60
4.1.2 Extension to Multiple Poincaré Sections 65
4.1.3 Different Implementations 67
4.1.4 Continuation Procedure 69
4.2 Numerical Application for the Quasi-Periodic Orbits Around the L2 Region of the CRTBP 70
4.2.1 Initial estimate for **Q** 72
4.2.2 Choosing the Poincaré Section Surfaces 74
4.2.3 Choosing θ and computing its derivative $\frac{d\theta_{\mathbf{X}_\tau}}{dX_\tau}$ 75
4.2.4 Computing A_θ and DA 78
4.2.5 Augmenting the error vector **F** and its derivative DF 80
4.2.6 Numerical Integration of the Orbits 82

4.2.7 Numerical computation of the Poincaré map 83
4.2.8 Numerical Computation of the Derivative of the Poincaré map 84
4.2.9 Continuation 85
4.3 Results 87
4.3.1 Lissajous Orbits 88
4.3.2 Quasi-Halo Orbits 90
4.3.3 Complete Periodic Family around L2 91
4.3.4 Comparison of the Results with the Literature 92
4.4 Extension of the CRTBP Results to the Full Ephemeris Model 93

5 Finding the Optimal Trajectories 101

5.1 Different Optimal Control Approaches 102
5.1.1 The Euler-Lagrange Formulation of the Optimal Control Problem (Indirect Method) 104
5.1.2 The Sequential Quadratic Programming Formulation of the Optimal Control Problem (Direct Method) 106
5.2 Unconstrained Minimum Energy Optimization 109
5.3 Constrained Minimum Energy Optimization 114
5.4 Free-End Condition Optimization 120
5.5 Minimum-Time Optimization 123
5.6 The Minimum-Fuel Optimization 129
5.7 Impulsive Thrust: Minimum-Fuel Optimization 134
5.8 Conclusion 136

6 Global Optimization of the Mission: The Traveling Salesman Problem 138

6.1 Realignment Cost Analysis 140
6.2 Defining the Global Optimization Problem 141

6.3 The Classical Traveling Salesman Problem 143
6.4 Mathematical Formulation of the Global Optimization Problem . . . 146
6.4.1 Cost function 146
6.4.2 Including the revisits into the formulation 147
6.4.3 Full Formulation 149
6.5 Numerical Methods Employed for Solving the Global Optimization Problem 150
6.5.1 Simulated annealing 151
6.5.2 Branching for time-optimal case 155
6.5.3 Results 156
6.6 Performance of SMART-1 as an Occulter 159
6.7 Multiple Occulters 162
6.7.1 Multiple Occulters on Quasi-Halo Orbits 163
6.7.2 Global Optimization with Constraints 164

7 Conclusion **170**

Chapter 1

Extrasolar Planet Imaging and Occulter-Based Telescopy

Studying terrestrial and giant planets outside the solar system is one of the primary goals of NASA's Origins Program. It is likely that the next decade will see NASA launch the first in a series of missions dubbed Terrestrial Planet Finders (TPF) to detect, image, and characterize extrasolar earthlike planets [1]. Current work is directed at studying a variety of architecture concepts and the associated optical engineering in order to prove the feasibility of such a mission. One such concept involves the formation flying of a conventional space telescope on the order of 2 to 4 meter diameter, in a Sun-Earth L2 Halo orbit, with a single or multiple large occulters, roughly 60 m across and 50,000 km away. The occulter blocks the light of a star and allows imaging of its dim, close-by planetary companion. Recent results in shaped-pupil technology at Princeton have made the manufacture of such a starshade feasible [2, 3]. This approach to planet imaging eliminates all of the precision optical requirements that exist in the alternate coronagraphic or interferometric approaches. However, it introduces the difficult problem of controlling and realigning the satellite formation. This approach introduces scientific challenges in the area of precise dynamics and control, which is my dissertation topic.

In this chapter, I first explain what a life-sustaining planet is and how such a planet can be differentiated from other planets based on the spectra of the light that is obtained via telescope imaging. Next, I discuss the scientific requirements and the technological challenges associated with a planet-imaging telescopy mission. Then, I describe a new approach, occulter-based coronagraphy, and I explain why it is a good candidate for planet-imaging missions. Finally, I outline the organization of the dissertation and explain how I approached the problems associated with the dynamics and control of the telescope and the occulter formation.

1.1 Finding Extrasolar Life

1.1.1 Life-Sustaining Planets

In order to search for extrasolar life, we must first define what it means for a planet to be life sustaining. The general astronomical understanding of a habitable planet is a planet which can accommodate "life as we know it"; in other words, where conditions are favorable for life as it can be found on Earth. This region is called the habitable zone and occurs in a star system where liquid water can exist. Figure 1.1 shows the habitable zone parameterized in terms of the distance from a star and the mass of a planet. As can be seen from the figure, new NASA missions such as the Kepler mission [4] and the Space Interferometry Mission (SIM) [5] will be able to discover possible life-sustaining extrasolar planets in the habitable zone.

1.1.2 Signs of Life

Today, over 270 planets have been discovered, starting with the first detection of a planet several times the size of Jupiter by Mayor & Queloz in 1995 [7]. These planets range in size from many earth masses, i.e., so called super-Earths, to many times the mass of Jupiter. Of course, a distinction must be made between discovering the existence of a planet and determining whether it supports life. Obtaining the orbital parameters and mass of a planet through indirect observations will not suffice for determining whether a planet sustains life. Instead, we must be able to directly image the planet, so that the full spectrum, which gives the characteristics of the planet, can be obtained.

Figure 1.2 shows the light spectrum data and the breakdown of the spectrum to its components that would be obtained if we were to image Earth from an extrasolar system [8]. In this figure we can see the spectroscopic biomarkers; the features in an exoplanet spectra that a life-sustaining planet is expected to have. The main

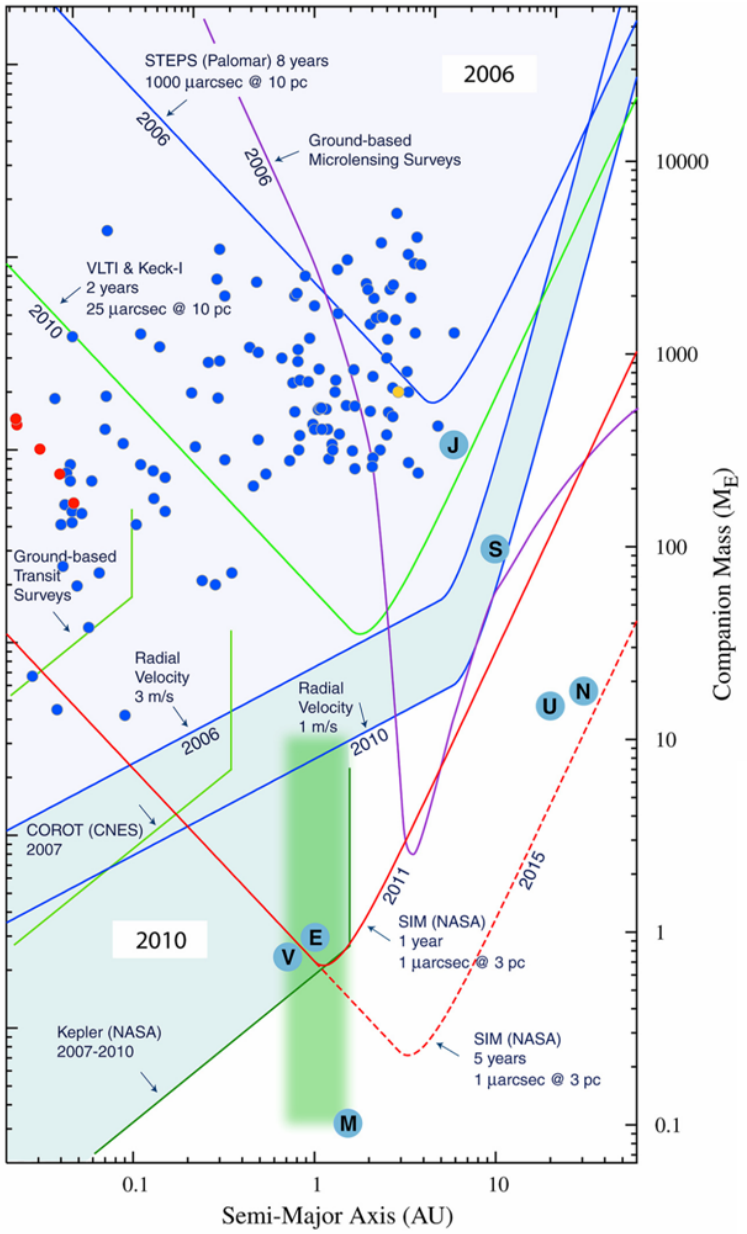

Figure 1.1: Semi-major axis vs mass of extrasolar planets. Shown in green is the habitable zone. The capabilities of current and proposed NASA missions are overlayed [6].

spectroscopic biomarkers are the existence of water, oxygen, ozone, and methane, and the occurrence of a vegetation red edge. A habitable planet is expected to contain large water bodies, which would lead to strong variability at 700 nm of the spectroscopic data due to the presence of water clouds. An active plant life would lead to the presence of free oxygen, which would in turn result in the presence of ozone.

The atmosphere of planets with a low mass like Earth but without vegetation should not contain methane due to stellar ultraviolet photodissociation; thus, its existence would suggest a biological presence. As seen in figure 1.2, at around 750 nm, we observe a vegetation red edge, which an Earth-like exoplanet might also exhibit [9] [10].

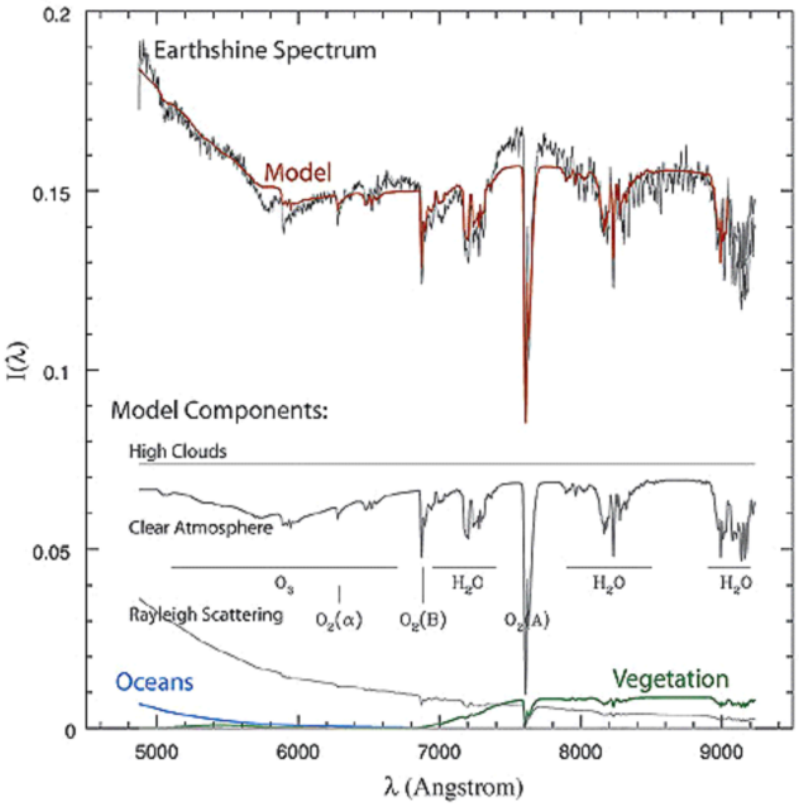

Figure 1.2: Earthshine spectrum and its components Woolf et al. [8]. In the figure, I represents light intensity and λ wavelength.

1.1.3 Challenges associated with imaging planets in the habitable zone

Most astronomers now suspect that rocky and possibly Earth-like planets orbit around nearby stars. To date, all known planets have been discovered by indirect means, that is, by measuring the motion of light from the parent star. These methods are

insensitive to the smaller terrestrial planets of interest and do not allow the most ambitious characterization. In order to capture the signs of life from a planet we need direct imaging of that planet.

As seen in figure 1.3, which simulates how the Solar System would be seen from a distant star, the direct observation of Earth-like planets is extremely challenging because their parent stars are about 10^10 times brighter (in the visible spectrum) but lie a fraction of an arcsecond away. Since the Earth atmosphere blurs the view of the stars, telescopes that are stationed on Earth do not enable such high precision imaging. Instead, space-based telescopy is required.

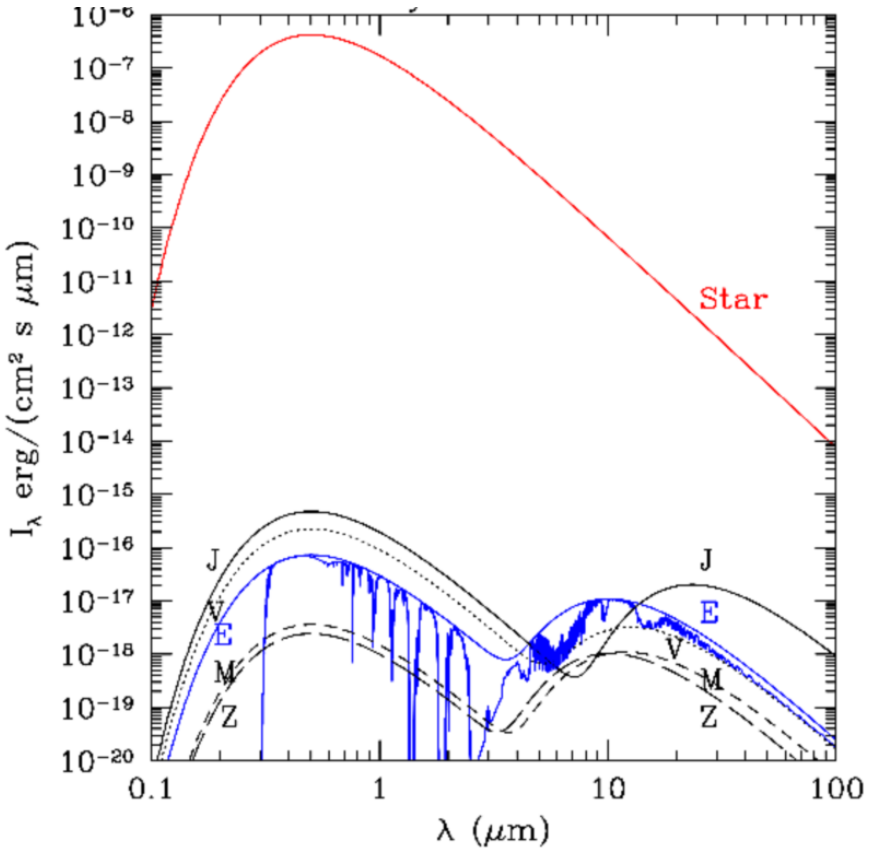

Figure 1.3: Simulation of light spectrum of the Sun and planets as seen from a distant star Des Marais et al. [11]. In the figure, I represents light intensity and λ wavelength. 'Star' stands for the Sun, and the solar planets are identified by their initial letters.

Many difficulties are involved in trying to achieve the high contrast necessary to

image a dim planet orbiting its parent star. Coronagraphy methods have been the most promising solution to this problems to this date. Shown in figure 1.4 is the drawing of the proposed NASA TPF-C mission (C stands for Coronagraph). Originally invented by Bernard Lyot to image the corona of the sun [12], coronagraphy is an optical technique which removes the starlight from the final image, while minimally affecting the planet, or which modifies the point spread function of the system so that the contrast is unity at the planet location. It consists of a dark spot at the image used to block the central core of the Airy pattern and a smaller aperture at a reimaged pupil to remove the residual stellar light. Building on this idea, different types of coronagraph designs that would give the needed high-contrast images have recently been designed at Princeton's TPF group, which is headed by Jeremy Kasdin. An example is shown in figure 1.4.

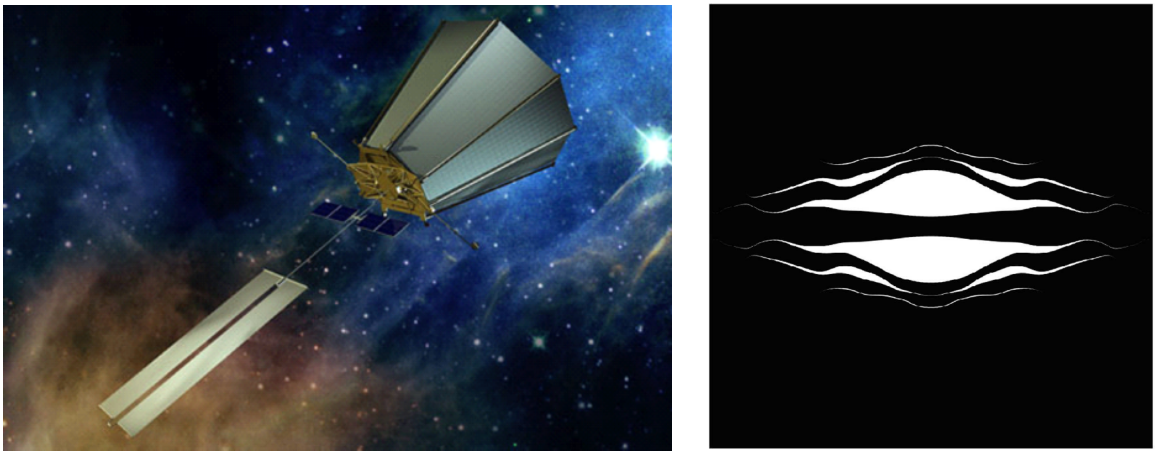

Figure 1.4: On the left, an artist's illustration of the TPF-C spacecraft [13]. On the right, an optimized coronagraph pupil design by Vanderbei that can achieve the needed contrast for exoplanet imaging if used with TPF-C [3].

The main challenge associated with designing a high-contrast imaging system is the scattered light problem, which denotes the scattering of light in the final image into the location of the planets point spread function due to aberrations in the optics. Due to manufacturing imperfections, the surface figure of all mirrors and lenses contains small variations from the desired shape, known as aberrations. This

negatively impacts imaging performance. Minor errors in reflectivity also affect the quality of the final image. The combined amplitude and phase errors in the optics typically degrade contrast by five or more orders of magnitude from the perfect optics assumption. This becomes the critical design driver in any planet imaging telescope. Until recently, solutions primarily focused on including an adaptive optics system in the telescope. Such a system consists of multiple deformable mirrors that correct the aberrated wavefront [14, 15]. Such a system measures the errors in the final image, estimates the electric field, and computes corrections for the deformable mirrors. Notwithstanding the recent progress in adaptive optics, such systems remain costly and complex.

1.2 External Occulter for Exoplanet Imaging

An alternative approach to high-contrast imaging of extrasolar planets has been proposed by Cash and Kasdin [9, 10, 16]. In this approach, an external screen or occulter is used to block the wavefront from the star before it ever enters the telescope. The poor diffraction performance of simple occulters has hitherto been an obstacle to the wide acceptance of this approach. Fortunately, recent results in shaped-pupil technology at Princeton have shown that these problems can be overcome with the manufacture of a special starshade occulter. An example of a promising new occulter design by Vanderbei, with a symmetric flower-shaped starshade, is shown in figure 1.5 [2]. This starshade is optimized for planet imaging by creating very high contrast at small angles and suppressing the parent stars competing light. Since no starlight can reflect off the surface aberrations, the need for wave-front control is eliminated.

Figure 1.6 shows a sketch of a sample occulter-based telescopy mission, consisting of a roughly 50-m starshade flying 50,000 km from a conventional, 2-4-m diameter telescope observatory [10]. The occulter significantly enhances the observatorys ca-

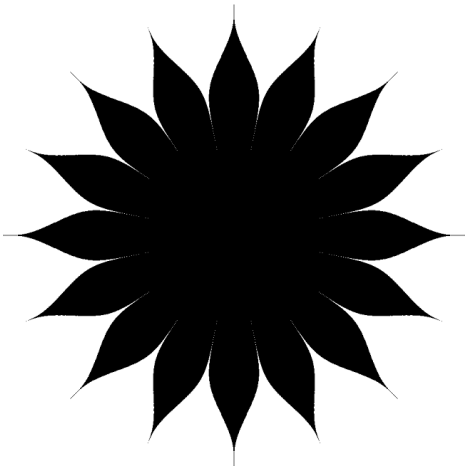

Figure 1.5: A multi-petal occulter design optimized for maximization of starlight suppression [2].

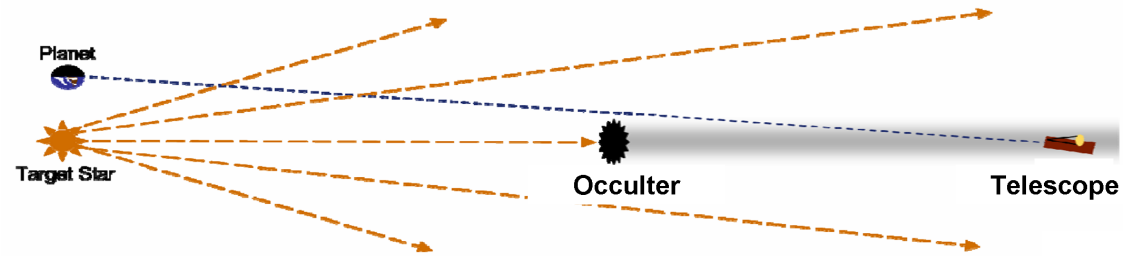

Figure 1.6: Occulter-based extra-solar planet-finding mission diagram [16]

pabilities and lowers the exoplanet mission cost by avoiding the need for expensive telescopes such as those required for suggested coronagraph and interferometer missions such as TPF-C and TPF-I. Because the occulter is not built into the telescope as an add-on instrument, scattered light is reduced due to the existence of fewer optical surfaces. This is due mainly to the fact that, as indicated above, the external occulter circumvents the use of high-precision wavefront control in the optical design. There are no unwanted diffraction spikes resulting from coronagraph supports, and the complexity of telescope instruments, such as the small-scale imperfections in the manufacturing and surfaces, is reduced. However, it introduces the difficult problem of controlling and realigning the satellite formation.

As shown in figure 1.7, the baseline design of this mission suggests the placement of

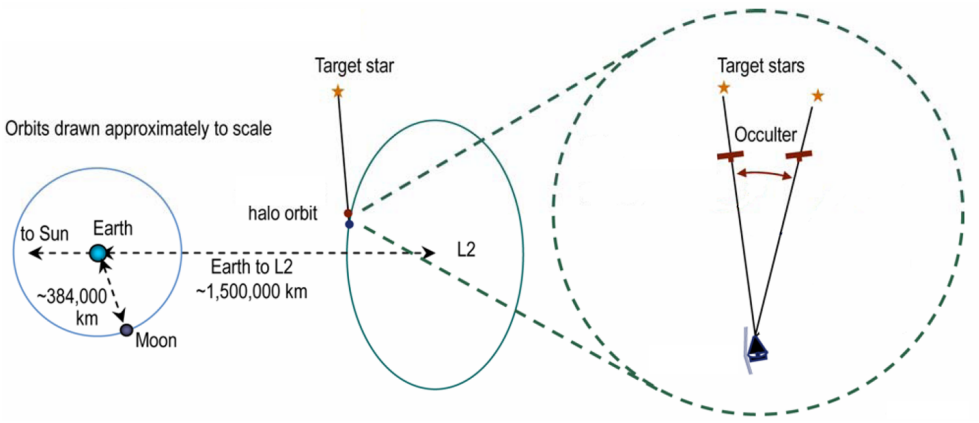

Figure 1.7: A schematic diagram of occulter mission orbits projected into the ecliptic plane [16]

.

an occulter satellite and a telescope near a Halo orbit about the Sun-Earth L2 point. Spacecraft mission design around the L2 libration point has been used since the ISEE3 mission in 1978 due to its several advantages (see publications by Farquhar et al. for more details [17, 18, 19, 20]). The energy level of the libration point orbits are close to that of the Earth and the unstable manifold of L2 Halo orbits passes very close to Earth. As a result, reaching these orbits is easy and requires minimal fuel. Since the Sun, Earth and Moon are all in the same direction with respect to Sun-Earth L2 point, half of the celestial sphere is available for imaging at any given time. The constant distance to Earth also makes it relatively easier to keep communication with spacecraft on L2 libration orbits than if it were on heliocentric drift-away orbits. Finally, L2 has a stable thermal environment, which is a requirement for the temperature-sensitive equipment – optical systems, lenses, and mirrors – on the telescopy mission under study.

1.3 Dissertation Outline

This dissertation is presented in six chapters, the first of which is this introduction. The remaining chapters are outlined below:

Chapter 2: Dynamical Analysis of the L2 Region

This chapter focuses on the underlying physics and qualitative behavior of the natural dynamics of this system. I review the relevant literature on the bounded motion of a small point-mass particle near the L2 point of the Circularly Restricted Three Body Problem (CRTBP). These fuel-free orbits are useful as the point of departure for the occulter mission design.

Chapter 3: Periodic Orbits of Interest Around L2: Numerical Methods

The horizontal Lyapunov, the vertical Lyapunov, and the Halo periodic orbits around the L2 point are obtained numerically, and their stability properties are examined. The real orbits in our solar system that correspond to these periodic orbits of interest are then computed.

Chapter 4: Multiple Poincaré Sections Method for Finding the Quasi-Halo and Lissajous Orbits

Quasi-Halo orbits are good candidates for occulter placement, as they are fuel-free orbits and have large sky coverage with respect to the Halo orbit, where the telescope is placed. With the aim of identifying these orbits, I develop a new numerical method that employs multiple Poincaré sections to find quasi-periodic orbits. This method converges to the desired orbits quickly, and it exhibits robust behavior near chaotic regions. Its numerical implementation for Lissajous and Quasi-Halo orbits are explained. These results are then extended from the simplified three body model to find the orbits in the real solar system that have the same characteristics.

Chapter 5: Finding the Optimal Trajectories

The optimal control problem of the realignment and Earth to Halo transfers is solved. Different implementations, including the fuel- and time-optimal trajectories that take the occulter from a given star Line-Of-Sight (LOS) to another

LOS, and from Earth to Halo, are numerically calculated using Euler Lagrange, shooting and nonlinear programming approaches.

Chapter 6: Global Optimization of the Mission: The Traveling Salesman Problem

The global optimization problem of finding the sequencing and timing of the imaging sessions is examined. By including the telescopy constraints, the problem becomes a Dynamic Time-Dependent Traveling Salesman Problem (TSP) with dynamical constraints. Simulated annealing and branching heuristic methods are employed to solve the TSP. Global optimization is performed for both the single and multiple occulter missions. A feasibility study of the mission is performed by analyzing possible scenarios with the capabilities of the SMART-1 spacecraft.

Chapter 2

Dynamical Analysis of the L2 Region

As discussed previously, the aim of this dissertation is to find the "best" trajectories for each spacecraft that is part of the occulter-based telescopy mission. In three-dimensional space, this translates into the optimization of $3 \times N_{s/c}$ control forces in a $6 \times (N_{s/c} + N_{gb})$ dimensional dynamical system, where $N_{s/c}$ and N_{gb} are the number of spacecraft and gravitational bodies, respectively. In order to reduce the complexity of the problem, I first analyze the control-free natural dynamics of a single spacecraft under the simpler gravitational model.

This chapter focuses on the underlying physics and qualitative behavior of the natural dynamics of this system. More specifically, I review the relevant literature on the bounded motion of a small point-mass particle near the second Lagrange point (also referred to as the libration point) of the Circular Restricted Three Body Problem (CRTBP). This analysis helps identify the suitable regions of the phase space for spacecraft placement.

In this chapter, I first derive the equations of motion for the CRTBP system in a rotating frame. I then find the equilibrium points of this system. Linearizing the equations of motion around the L2 equilibrium point, I categorize the types of motion in the vicinity of the L2 point. Expanding the equations of motion in higher-order Legendre polynomials, I apply the Lindstedt-Poincaré procedure to obtain the periodic halo orbits, which do not exist in the linearized system. I then apply the center manifold reduction procedure to obtain the complete periodic phase space in the extended L2 neighborhood. These fuel-free orbits provides the point of departure for the occulter mission design.

2.1 Circularly Restricted Three Body Problem - Equations of Motion

The Two-Body Problem, which can be solved analytically, describes the motion of two bodies under the effect of their mutual gravitation interaction given their initial conditions and masses [21, 22, 23]. There is no closed-form solution for the extension of this problem to three bodies. Euler suggested a simplification of this Three-Body Problem called the Circularly Restricted Three Body Problem (CRTBP) [24]. In the CRTBP, the first two bodies, m_1 and m_2, called the primaries, are in circular motion around their center of mass, which is the result of their mutual interaction based on two-body gravitational dynamics. The third body, m_3, which is free to move, is assumed to be massless and hence to have no effect on the motion of the other two bodies. The problem is to find the motion of the third body as determined by the other two constrained bodies' gravitational force. These assumptions reduce the system's degrees of freedom from nine to three, thereby increasing the tractability of the solutions while still giving insightful information. The CRTBP is a useful model for spacecraft mission design since the eccentricities of major planets in the Solar system are small, and the mass of a spacecraft is negligible in comparison to the celestial bodies.

In order to write the equations of motion under Newton's law of gravitation, an inertial frame of reference must be specified. The origin of the Newtonian inertial frame, I, is located at the center of mass of m_1 and m_2, O. I has coordinates X, Y, Z, such that the circular motion of the primaries is in the X, Y plane and the angular rotation of the primaries is in the positive Z direction. Without loss of generality, we assume that the first primary is heavier than the second primary, $m_1 > m_2$. In the inertial frame I, the equation of motion of m_3 under the gravitational forces of m_1

and m_2 is

$$m_3 \frac{d^2\vec{\mathbf{r}}^I}{dt^2} = -\frac{Gm_1m_3}{\|\vec{\mathbf{r_1}}\|^3}\vec{\mathbf{r_1}} - \frac{Gm_2m_3}{\|\vec{\mathbf{r_2}}\|^3}\vec{\mathbf{r_2}} \,, \tag{2.1}$$

where $\vec{\mathbf{r_1}}$ and $\vec{\mathbf{r_2}}$ are the relative positions of m_3 with respect to m_1 and m_2, respectively, and G is the universal gravitational constant.

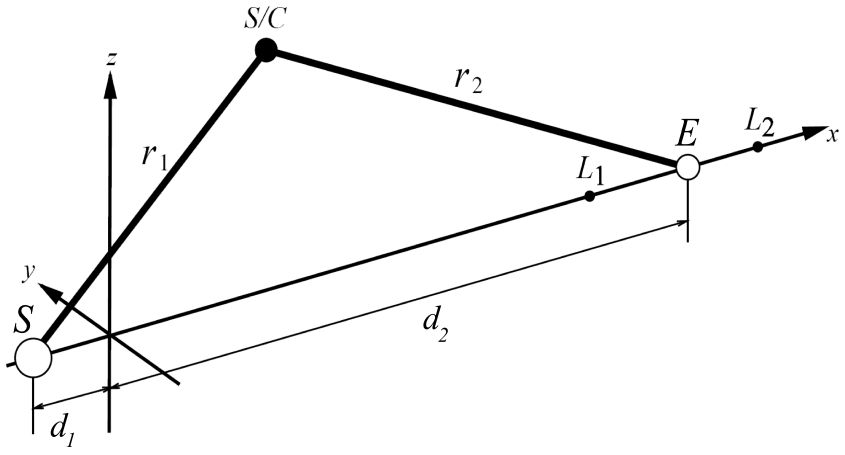

Figure 2.1: Sketch of the CRTBP in the rotating frame R, where the Sun, S, is m_1 and the Earth, E, is m_2, and S/C refers to the spacecraft, m_3.

In order to reduce the number of parameters and to generalize the solutions, the variables of the problem are typically nondimensionalized. The unit of mass is chosen as the total mass of the two main bodies, $M = m_1 + m_2$; the distance unit is chosen as the distance between the two main bodies, $D = \|\vec{\mathbf{d_1}}\| + \|\vec{\mathbf{d_2}}\|$; and the time unit is chosen such that the period, T, of the circular motion is 2π. Under these choices, the universal gravitational constant, G, becomes unity in order to enforce the two-body period equality, $T = 2\pi\frac{D^{3/2}}{M^{1/2}G^{1/2}}$. Angular velocity, $w = \frac{2\pi}{T}$, becomes unity as well. As a result, the nondimensional system depends only on a single parameter. This is the mass parameter, μ, defined as the ratio of the small body's mass to the total mass:

$\mu = \frac{m_2}{M}$. Then, the nondimensional masses of the primaries can be expressed as

$$m_1 = 1 - \mu \tag{2.2}$$

$$m_2 = \mu\,. \tag{2.3}$$

Since the distances of the primaries from the center of mass are inversely proportional to their masses, the nondimensional distances can be expressed as

$$\|\vec{\mathbf{d_1}}\| = \mu \tag{2.4}$$

$$\|\vec{\mathbf{d_2}}\| = 1 - \mu\,. \tag{2.5}$$

The nondimensionalized equation of motion becomes

$$\frac{d^2\vec{\mathbf{r}}^I}{dt^2} = -\frac{1-\mu}{\|\vec{\mathbf{r_1}}\|^3}\vec{\mathbf{r_1}} - \frac{\mu}{\|\vec{\mathbf{r_2}}\|^3}\vec{\mathbf{r_2}}\,. \tag{2.6}$$

In the inertial frame, I, the positions of the primaries are time dependent, making the motion difficult to analyze. The time dependence of the equations of motion can be eliminated by employing a rotating frame, R, with coordinates x, y, z. R is defined with the origin at O; x directs from m_1 to m_2; y is perpendicular to x and lies in the plane of the primaries' motion; and z coincides with Z (see figure 2.1). R is called the *synodical frame*.

In order to write the equations in R, the acceleration of m_3 in the inertial coordinates, $\frac{d^2\vec{\mathbf{r}}^I}{dt^2}$, should be expressed in terms of the rotating coordinate elements, x, y, and z. The kinematical relationship between the acceleration in the inertial frame I and the rotating frame R is

$$\frac{d^2\vec{\mathbf{r}}^I}{dt^2} = \dot{\vec{\omega}} \times \vec{\mathbf{r}} + \vec{\omega} \times (\vec{\omega} \times \vec{\mathbf{r}}) + 2\vec{\omega} \times \frac{d\vec{\mathbf{r}}^R}{dt} + \frac{d^2\vec{\mathbf{r}}^R}{dt^2}\,, \tag{2.7}$$

where $\vec{\omega}$ is the angular velocity of the rotating frame. In the nondimensional units, $\vec{\omega}$ is equal to $1 \cdot \hat{z}$; thus, the first term on the right hand side of equation 2.7 is nullified, and the inertial acceleration is simplified to

$$\frac{d^2\vec{\mathbf{r}}^I}{dt^2} = (\ddot{x} - 2\dot{y} - x)\,\hat{x} + (\ddot{y} + 2\dot{x} - y)\,\hat{y} + \ddot{z}\,\hat{z} \tag{2.8}$$

where the short-hand notation $\dot{}$ is used for the time derivative of a scaler. Plugging equation 2.8 into equation 2.6, the final form of the equation of motion is obtained,

$$\begin{aligned}
\ddot{x} &= 2\dot{y} + x - \frac{(1-\mu)(x+\mu)}{\|\vec{\mathbf{r_1}}\|^3} - \frac{\mu(x-1+\mu)}{\|\vec{\mathbf{r_2}}\|^3} \\
\ddot{y} &= -2\dot{x} + y - \frac{(1-\mu)y}{\|\vec{\mathbf{r_1}}\|^3} - \frac{\mu y}{\|\vec{\mathbf{r_2}}\|^3} \\
\ddot{z} &= -\frac{(1-\mu)z}{\|\vec{\mathbf{r_1}}\|^3} - \frac{\mu z}{\|\vec{\mathbf{r_2}}\|^3}\,.
\end{aligned} \tag{2.9}$$

In these equations, the nondimensional positions with respect to the primaries are

$$\vec{\mathbf{r_1}} = (x+\mu)\hat{x} + y\hat{y} + z\hat{z} \tag{2.10}$$

$$\vec{\mathbf{r_2}} = (x-1+\mu)\hat{x} + y\hat{y} + z\hat{z}\,. \tag{2.11}$$

Defining an effective potential, $\bar{U}(x,y,z)$, as

$$\bar{U}(x,y,z) = \frac{1-\mu}{\|\vec{\mathbf{r_1}}\|} + \frac{\mu}{\|\vec{\mathbf{r_2}}\|} + \frac{x^2+y^2}{2}\,, \tag{2.12}$$

the equations can be expressed in a simpler form,

$$\begin{aligned}
\ddot{x} &= 2\dot{y} + \frac{\partial \bar{U}(x,y,z)}{\partial x} \\
\ddot{y} &= -2\dot{x} + \frac{\partial \bar{U}(x,y,z)}{\partial y} \\
\ddot{z} &= \frac{\partial \bar{U}(x,y,z)}{\partial z}\,.
\end{aligned} \tag{2.13}$$

Defined by the differential equation 2.13, CRTBP has a first integral called the *Jacobi Constant*, C, which is given by

$$C(x, y, z, \dot{x}, \dot{y}, \dot{z}) = -(\dot{x}^2 + \dot{y}^2 + \dot{z}^2) + 2\bar{U} + \mu(1-\mu). \tag{2.14}$$

Differentiating C with respect to time, it can be observed that it is time invariant and thus a constant of motion:

$$\begin{aligned} \frac{d}{dt}C &= -2(\dot{x}\ddot{x} + \dot{y}\ddot{y} + \dot{z}\ddot{z}) + 2\frac{d}{dt}\bar{U} \\ &= -2\left((2\dot{y} + \frac{\partial \bar{U}}{\partial x})\dot{x} + (-2\dot{x} + \frac{\partial \bar{U}}{\partial y})\dot{y} + \frac{\partial \bar{U}}{\partial z}\dot{z}\right) + 2\frac{d}{dt}\bar{U} \\ &= -2\left(\frac{\partial \bar{U}}{\partial x}\dot{x} + \frac{\partial \bar{U}}{\partial y}\dot{y} + \frac{\partial \bar{U}}{\partial z}\dot{z}\right) + 2\frac{d}{dt}\bar{U} = 0 \end{aligned} \tag{2.15}$$

The existence of this integral of motion is due to the time-independent Lagrangian nature of the CRTBP differential equation system (equation 2.13), which leads to energy conservation (see [25] for details).

2.2 Equilibrium Points

At the equilibrium of a differential system, the state variables stay constant for all time. Thus, in order to find the equilibrium points of CRTBP, all derivative terms in equation 2.13 are set equal to zero:

$$0 = \frac{\partial \bar{U}}{\partial x} = x - \frac{(1-\mu)(x+\mu)}{\|\vec{\mathbf{r_1}}\|^3} - \frac{\mu(x-1+\mu)}{\|\vec{\mathbf{r_2}}\|^3} \tag{2.16}$$

$$0 = \frac{\partial \bar{U}}{\partial y} = y\left(1 - \frac{(1-\mu)}{\|\vec{\mathbf{r_1}}\|^3} - \frac{\mu}{\|\vec{\mathbf{r_2}}\|^3}\right) \tag{2.17}$$

$$0 = \frac{\partial \bar{U}}{\partial z} = z\left(-\frac{(1-\mu)}{\|\vec{\mathbf{r_1}}\|^3} - \frac{\mu}{\|\vec{\mathbf{r_2}}\|^3}\right). \tag{2.18}$$

The five sets of values that satisfy these equations are called the Lagrange or the libration equilibrium points. It is apparent from equation 2.18 that, at any equilibrium point, z should be equal to zero. There are two possible solutions for equation 2.17; $y = 0$ or $y \neq 0$. In the former case, there are three x values that satisfy equation 2.16 ([24]). These are the collinear Lagrange points L_1, L_2, and L_3 with coordinates

$$L_1 = \{1 - \mu - \gamma_1, 0, 0\}\,, \tag{2.19}$$

$$L_2 = \{1 - \mu + \gamma_2, 0, 0\}\,, \tag{2.20}$$

$$L_3 = \{-\mu - \gamma_3, 0, 0\}\,. \tag{2.21}$$

where γ_1, γ_2, and γ_3 refer to the distances between the collinear Lagrange points and their closest primaries. These are uniquely given by the positive roots of the following quintic equations:

$$\gamma_1^5 - (3-\mu)\gamma_1^4 + (3-2\mu)\gamma_1^3 - \mu\gamma_1^2 + 2\mu\gamma_1 - \mu = 0\,, \tag{2.22}$$

$$\gamma_2^5 + (3-\mu)\gamma_2^4 + (3-2\mu)\gamma_2^3 - \mu\gamma_2^2 - 2\mu\gamma_2 - \mu = 0\,, \tag{2.23}$$

$$\gamma_3^5 + (2+\mu)\gamma_3^4 + (1+2\mu)\gamma_3^3 - (1-\mu)\gamma_3^2 - 2(1-2\mu)\gamma_3 - (1-\mu) = 0\,. \tag{2.24}$$

The other set of equilibrium points arise when $y \neq 0$. In this case, $r_1 = r_2 = 1$ should be satisfied for equation 2.17 to hold. The positions of m_1, m_2, and m_3 then form an equilateral triangle. There are two equilibrium points that satisfy this constraint; these are L_4 and L_5 with positions

$$L_4 = \{\mu - \frac{1}{2}, \frac{\sqrt{3}}{2}, 0\}\,, \tag{2.25}$$

$$L_5 = \{\mu - \frac{1}{2}, -\frac{\sqrt{3}}{2}, 0\}. \tag{2.26}$$

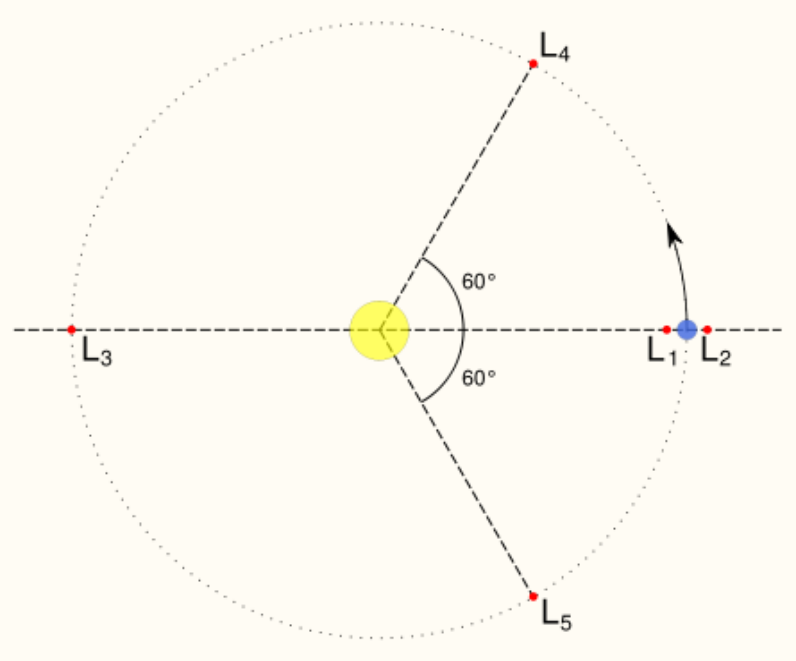

Figure 2.2: Sketch of the locations of the Lagrange points [26]

2.3 Series Expansion around L2

While the ultimate aim is to characterize motion in the neighborhood of L2, analytical solutions are not available. I therefore proceed with asymptotic analysis, which requires series expansion of the expressions on the right hand side of equation 2.13. It is necessary to first change the variables such that the coordinates themselves are small parameters. Subsequently, an appropriate expansion method is employed to obtain the full series expressions.

2.3.1 Translation of L_2 to the origin, and rescaling

In order to linearize CRTBP around the L_2 point, which has the coordinates $\{1 - \mu + \gamma_2, 0, 0\}$, the equations must be written in a different set of coordinates, where L_2 is at the origin. In the next section, I will perform asymptotic analysis in the neighborhood of L_2, which extends from L2 to m_2. Following Richardson [27], I therefore change the unit of distance from D, the distance between the primaries, to

γ_2, the distance from L2 to m_2, since this is more in line with the length scales of the problem. The distance unit rescaling ensures that the series expansions have good numerical properties. In order to translate L_2 to the origin and rescale the units, the following change of variables is applied:

$$x_{new} = \frac{x - 1 + \mu - \gamma_2}{\gamma_2} \tag{2.27}$$

$$y_{new} = \frac{y}{\gamma_2} \tag{2.28}$$

$$z_{new} = \frac{z}{\gamma_2} \tag{2.29}$$

$$\tag{2.30}$$

The mass unit is kept as M. Time unit is chosen such that the gravitational constant, G, is unity in the new unit system as it was before. In the new time unit, the period of the circular motion of the primaries, T, is $2\pi \left(\frac{D}{\gamma_2}\right)^{3/2}$, as a result of the Keplerian period equation for the primaries, $T = 2\pi \frac{D^{3/2}}{M^{1/2} G^{1/2}}$. To simplify the equations, we define a new variable, γ_L,

$$\gamma_L \triangleq \frac{\gamma_2}{D} \, .$$

Then, the period of the primaries is $T = 2\pi {\gamma_L}^{-\frac{3}{2}}$, and the angular velocity, $\omega = \frac{2\pi}{T}$, is ${\gamma_L}^{\frac{3}{2}}$. Change in the unit of time scales the time derivative operator, $\dot{}$, in the new unit system by ${\gamma_L}^{\frac{3}{2}}$. To keep the differential equations consistent, we define a new time variable, s,

$$s \triangleq {\gamma_L}^{\frac{3}{2}} t \, ,$$

and a derivative with respect to this new time variable,

$$' \triangleq \frac{d}{ds} \, .$$

This notation enables the use of the old differential equations by only replacing, $\dot{}$, with, $'$. From here on, subscripts for x_{new}, y_{new} and z_{new} are dropped for convenience.

2.3.2 Series Expansion of the Equations

The right hand terms in the equations of motion, equation 2.13, are expanded using the fact that

$$\frac{1}{\|\vec{\mathbf{r}}+\vec{\rho}\|} = \frac{1}{\|\vec{\mathbf{r}}\|}\sum_{n=0}^{\infty} P_n\left(cos(\alpha)\right)\left(\frac{\|\vec{\rho}\|}{\|\vec{\mathbf{r}}\|}\right)^n \tag{2.31}$$

where $P_n\left(\cdot\right)$ are the Legendre polynomials, and

$$cos(\alpha) = \frac{\vec{\rho}\cdot\vec{\mathbf{r}}}{\|\vec{\rho}\|\|\vec{\mathbf{r}}\|}\,. \tag{2.32}$$

Defining $\vec{\rho} = x, y, z$, distances to primaries can be written as

$$\vec{\mathbf{r_1}} = (\frac{1}{\gamma_L}+1)\hat{x}+\vec{\rho} \tag{2.33}$$

$$\vec{\mathbf{r_2}} = \hat{x}+\vec{\rho}. \tag{2.34}$$

Using equations 2.31-2.34, the gravitation potential can be expanded in Legendre polynomials around L_2,

$$\frac{1-\mu}{\|\vec{\mathbf{r_1}}\|}+\frac{\mu}{\|\vec{\mathbf{r_2}}\|} = \sum_{n\geqslant 2}^{\infty} c_n\rho^n P_n\left(\frac{x}{\rho}\right)\,. \tag{2.35}$$

where $\rho = \|\vec{\rho}\|$ and the c_n coefficients are

$$c_n = \frac{(-1)^n}{{\gamma_L}^3}\left(\mu+\frac{(1-\mu){\gamma_L}^{n+1}}{(1+\gamma_L)^{n+1}}\right). \tag{2.36}$$

Thus, the series expansion for the effective potential, $\bar{U}$, in equation 2.12 becomes

$$\begin{aligned}\bar{U} &= \frac{x^2+y^2}{2} + \frac{1-\mu}{\|\vec{\mathbf{r_1}}\|} + \frac{\mu}{\|\vec{\mathbf{r_2}}\|} \\ &= \frac{1}{2}\left((1+2c_2)x^2 + (1-c_2)y^2 - c_2 z^2\right) + \sum_{n\geqslant 3}^{\infty} c_n \rho^n P_n\left(\frac{x}{\rho}\right) . \end{aligned} \tag{2.37}$$

Substituting the new coordinates in equation 2.13 and employing the $\bar{U}$ expansion, the equations of motion become:

$$\begin{aligned} x'' - 2y' - (1+2c_2)x = &\quad \frac{\partial}{\partial x}\sum_{n\geqslant 3}^{\infty} c_n \rho^n P_n\left(\frac{x}{\rho}\right) = \quad \sum_{n\geqslant 2}^{\infty}(n+1)c_{n+1}\rho^n P_n\left(\frac{x}{\rho}\right) \\ y'' + 2x' + (c_2-1)y = &\quad \frac{\partial}{\partial y}\sum_{n\geqslant 3}^{\infty} c_n \rho^n P_n\left(\frac{x}{\rho}\right) = \quad \sum_{n\geqslant 3}^{\infty} c_n y \rho^{n-2}\tilde{P}_n\left(\frac{x}{\rho}\right) \\ z'' + c_2 z = &\quad \frac{\partial}{\partial z}\sum_{n\geqslant 3}^{\infty} c_n \rho^n P_n\left(\frac{x}{\rho}\right) = \quad \sum_{n\geqslant 3}^{\infty} c_n z \rho^{n-2}\tilde{P}_n\left(\frac{x}{\rho}\right) , \end{aligned} \tag{2.38}$$

where

$$\tilde{P}_n = \sum_{k=0}^{[(n-2)/2]} (3+4k-2n) P_{n-2k-2}\left(\frac{x}{\rho}\right) , \tag{2.39}$$

and the bracket operator, [ ], gives the integer part of a real number.

2.4 Analysis of the Linear Part around L2

Before looking at the more complicated non-linear dynamical system, I investigate the linearized system to gain insight into the stability and the structure of the phase space. Ignoring the second and high-order terms in equation 2.38, the linear equations

of motion are

$$\begin{aligned} x'' - 2y' - (1+2c_2)x &= 0 \\ y'' + 2x' + (c_2 - 1)y &= 0 \\ z'' + c_2 z &= 0\,. \end{aligned} \tag{2.40}$$

The linearized motion in the $x-y$ plane and in the z direction are independent of one another. For the purpose of our studies, which focus on the motion around the Earth-Sun L2 with $\mu = 3.040423398444176 \times 10^{-6}$, the c_2 constant can be obtained from equation 2.36 as 4.006810788883402. Noting that $c_2 > 0$, motion in the z direction is a simple harmonic oscillator. To study the in-plane motion, the differential equations are written in the first-order form:

$$\frac{d}{dt}\begin{pmatrix} x \\ y \\ x' \\ y' \end{pmatrix} = \begin{pmatrix} 0 & 0 & 1 & 0 \\ 0 & 0 & 0 & 1 \\ (1+2c_2) & 0 & 0 & 2 \\ 0 & -(c_2-1) & -2 & 0 \end{pmatrix} \begin{pmatrix} x \\ y \\ x' \\ y' \end{pmatrix}. \tag{2.41}$$

This system has four eigenvalues, which are

$$\begin{aligned} e_{1,2} &= \pm\lambda = \pm\frac{\sqrt{c_2 - 2 + \sqrt{9{c_2}^2 - 8c_2}}}{\sqrt{2}} \\ e_{3,4} &= \pm i\nu = \pm i\frac{\sqrt{-c_2 + 2 + \sqrt{9{c_2}^2 - 8c_2}}}{\sqrt{2}}\,, \end{aligned} \tag{2.42}$$

where λ and ν are positive constants. This can be shown through algebraic manipulation for $\mu < \frac{1}{2}$ [24]. Thus, the planar system has two real eigenvalues, λ and $-\lambda$, corresponding to the divergent and convergent modes, respectively, and, two imaginary eigenvalues, $\pm\nu$, corresponding to the oscillatory modes. The corresponding

eigenvectors for these modes are

$$\vec{\mathbf{v}}_{\lambda} = \begin{pmatrix} 1 \\ -\sigma \\ \lambda \\ -\lambda\sigma \end{pmatrix}, \vec{\mathbf{v}}_{-\lambda} = \begin{pmatrix} 1 \\ \sigma \\ -\lambda \\ -\lambda\sigma \end{pmatrix}, \vec{\mathbf{v}}_{-\nu} = \begin{pmatrix} 1 \\ ik \\ i\nu \\ -\nu k \end{pmatrix}, \vec{\mathbf{v}}_{\nu} = \begin{pmatrix} 1 \\ -ik \\ -i\nu \\ -\nu k \end{pmatrix}, \tag{2.43}$$

where

$$\begin{aligned} \sigma &= \frac{2\lambda}{\lambda^2 + c_2 - 1} \quad \text{and} \\ k &= \frac{\nu^2 + 2c_2 + 1}{2\nu}. \end{aligned} \tag{2.44}$$

The general solution to the linear ODE can then be written as:

$$\begin{pmatrix} x(s) \\ y(s) \\ x'(s) \\ y'(s) \end{pmatrix} = C_1 e^{\lambda s} \begin{pmatrix} 1 \\ -\sigma \\ \lambda \\ -\lambda\sigma \end{pmatrix} + C_2 e^{-\lambda s} \begin{pmatrix} 1 \\ \sigma \\ -\lambda \\ -\lambda\sigma \end{pmatrix} + C_3 \begin{pmatrix} cos(\nu s) \\ -k\ sin(\nu s) \\ -\nu\ sin(\nu s) \\ -\nu k\ cos(\nu s) \end{pmatrix} + C_4 \begin{pmatrix} sin(\nu s) \\ k\ cos(\nu s) \\ \nu\ cos(\nu s) \\ -\nu k\ sin(\nu s) \end{pmatrix}. \tag{2.45}$$

The $x - y$ plane has a center $\times$ saddle structure. This can be visualized by drawing the projection of the motion in these subspaces onto the x-y coordinates, by ignoring the velocity components (See figure 2.3). Including the z-direction mode, the linear phase space around the L_2 point has the center $\times$ center $\times$ saddle structure.

Saddle behavior around the Lagrange point can be utilized to design efficient trajectories that veer in and out of the libration region for spacecraft missions. Furthermore, analyzing the stable and unstable manifolds, it can be shown that there exists a heteroclinic connection between the L_1 and L_2 points [28, 25]. This characteristic is useful in mission design, such as the GENESIS mission trajectory to move

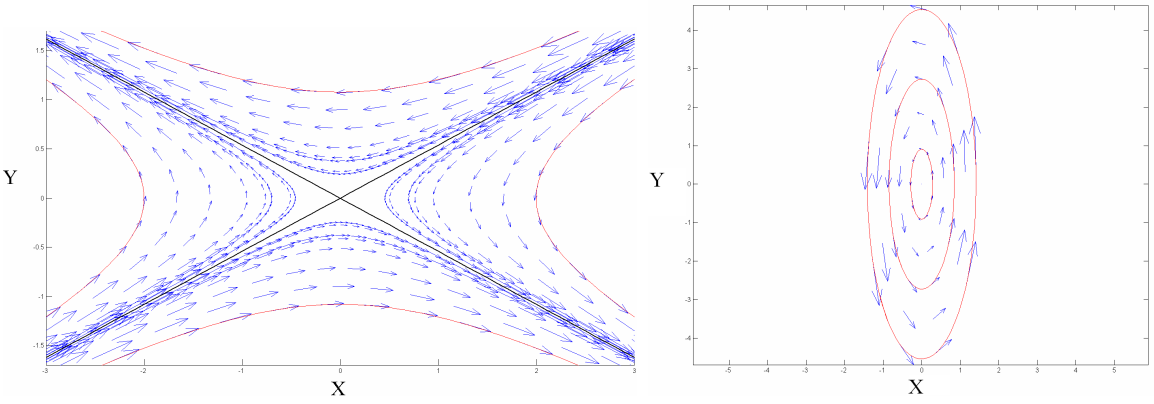

Figure 2.3: Projection onto the x-y coordinates of the saddle subspace (on the left) and center subspace (on the right) of the linearized planer motion around L2

between Sun-Earth L1 and L2 [29, 30].

Because this dissertation focuses on the types of motion that stay around the L_2 region for all time, i.e. the libration orbits, this stable and unstable behavior will not be analyzed further. Instead, I focus on the librational motion.

2.5 High-Order Analysis (The Lindstedt-Poincaré Procedure and Halo Orbits)

As seen above, there are periodic (and quasiperiodic) orbits near the collinear libration points. I now turn to higher-order approximations for further insight.

Without loss of generality, if we restrict the initial conditions such that divergent motion is not allowed, i.e. that the stable and unstable modes in the x-y plane are excluded, we obtain the linear quasi-periodic orbits around L2, which can be written in compact form as

$$\begin{aligned} x &= -A_x cos(\nu s + \phi) \\ y &= kA_x sin(\nu s + \phi) \\ z &= A_z cos(\omega_z s + \psi) \ , \end{aligned} \tag{2.46}$$

where $\omega_z = \sqrt{c_2}$. In the general case, when the in-plane and out-of-plane frequencies are not commensurable, i.e., when $\frac{\nu}{\omega_z} \neq \frac{i_1}{i_2}$ where i_1 and i_2 are integers, Lissajous orbits are obtained. In the linear analysis of the Earth-Sun CRTBP L2 point, these frequencies,

$$\begin{aligned} \nu &= 2.073256862131411 \quad \text{and} \\ \omega_z &= 2.001701973042791 \ , \end{aligned} \tag{2.47}$$

are not commensurable. As a result, there are no three-dimensional periodic orbits in the linear L2 system. However, as we move further away from the origin, and A_x and A_z increase, these amplitudes may affect the frequencies ν and ω_z in a nonlinear fashion. Since the frequencies in the x-y plane and in the z direction are very close to one another, it makes intuitive sense to seek the possibility of 1-1 commensurate nonlinear three-dimensional orbits. When the in-plane and out-of-plane frequencies are equal, i.e. $\nu = \omega_z$, 1-1 commensurable periodic orbits are obtained. These orbits were first discovered by Farquhar, who coined the term "Halo" orbits due to the resemblance of the Earth-Lunar L2 Halo orbits to a halo when seen from Earth [31, 32, 33].

The linearized equations give the first approximation for this type of periodic motion. In order to find the solutions for the Halo orbits up to the third order, I use Richardson's application of the Lindstedt-Poincaré successive approximation technique [27]. In the Lindstedt-Poincaré procedure, the frequency correction for the periodic motion is expanded in powers of the amplitude $\mathcal{O}(A_x^n)$,

$$\omega = 1 + \sum_{n \geqslant 1} \omega_n, \quad \omega_n < 1 \ , \tag{2.48}$$

where the coefficients ω_n are chosen to remove the secular terms at each step.

A new time variable, $\tau = \omega s$, is introduced, and the equations of motion 2.38 are

expanded up to the third order, which yields

$$\begin{aligned}
\omega^2 x'' - 2\omega y' - (1+2c_2)x &= \frac{3}{2}c_3(2x^2 - y^2 - z^2) + 2c_4 x(2x^2 - 3y^2 - 3z^2) + \mathcal{O}(4) \\
\omega^2 y'' + 2\omega x' + (c_2 - 1)y &= -3c_3 xy - \frac{3}{2}y(4x^2 - y^2 - z^2) + \mathcal{O}(4) \\
\omega^2 z'' + c_2 z &= -c_3 xz - \frac{3}{2}z(4x^2 - y^2 - z^2) + \mathcal{O}(4)\ . \qquad (2.49)
\end{aligned}$$

It can be shown that the choice of

$$\omega_1 = 0 \quad \text{and} \quad \omega_2 = s_1 A_x^2 + s_2 A_z^2, \qquad (2.50)$$

removes the secular terms up to third order, with the requirement that in-plane and out-of-plane amplitudes and phases satisfy the following conditions:

$$\begin{aligned}
0 &= l_1 A_x^2 + l_2 A_z^2 + \Delta \\
\psi &= \phi + n\frac{\pi}{2}, \quad n = 1,\ 3\ . \qquad (2.51)
\end{aligned}$$

For lengthy variables, l_1, l_2, s_1, s_2 and Δ, see [27]. From these equations, we see that the smallest Halo orbit occurs when $A_z = 0$, which, in the Sun-Earth L2 case, corresponds to approximately $A_x = 200,000$ km.

Using the frequency correction and the phase amplitude constraints, the third-order solution of the Halo orbit is

$$\begin{aligned}
x &= a_{21}A_x^2 + a_{22}A_z^2 - A_x cos(\tau_1) + (a_{23}A_x^2 - a_{24}A_z^2)cos(2\tau_1) \\
&\quad + (a_{31}A_x^3 - a_{32}A_x A_z^2))cos(3\tau_1) \\
y &= kA_x sin(\tau_1) + (b_{21}A_x^2 - b_{22}A_Z^2)sin(2\tau_1) + (b_{31}A_x^3 - b_{32}A_x A_z^2)sin(3\tau_1) \\
z &= \delta_n(A_z cos(\tau_1) + d_{21}A_x A_z(cos(2\tau_1) - 3) \\
&\quad + (d_{32}A_z A_x^2 - d_{31}A_z^3)cos(3\tau_1))\ , \qquad (2.52)
\end{aligned}$$

where

$$\begin{aligned} \tau_1 &= \nu\tau + \phi\,, \\ \delta_n &= 2 - n, \quad n = 1,\ 3\,. \end{aligned} \tag{2.53}$$

Depending on the value of n, there are two types of Halo orbits, called the northern ($n = 1$) and southern Halos ($n = 3$), which are the mirror images of each other with respect to the $x - y$ plane. This is due to the CRTBP's mirror symmetry across the $z = 0$ plane, that is, the equations of motion are invariant under the transformation: $\{x,\ y,\ z,\ \dot{x},\ \dot{y},\ \dot{z}\} \Rightarrow \{x,\ y,\ -z,\ \dot{x},\ \dot{y},\ -\dot{z}\}$. Figure 2.4 shows an approximate northern Halo orbit obtained via the Richardson formulation. While it is possible to extend

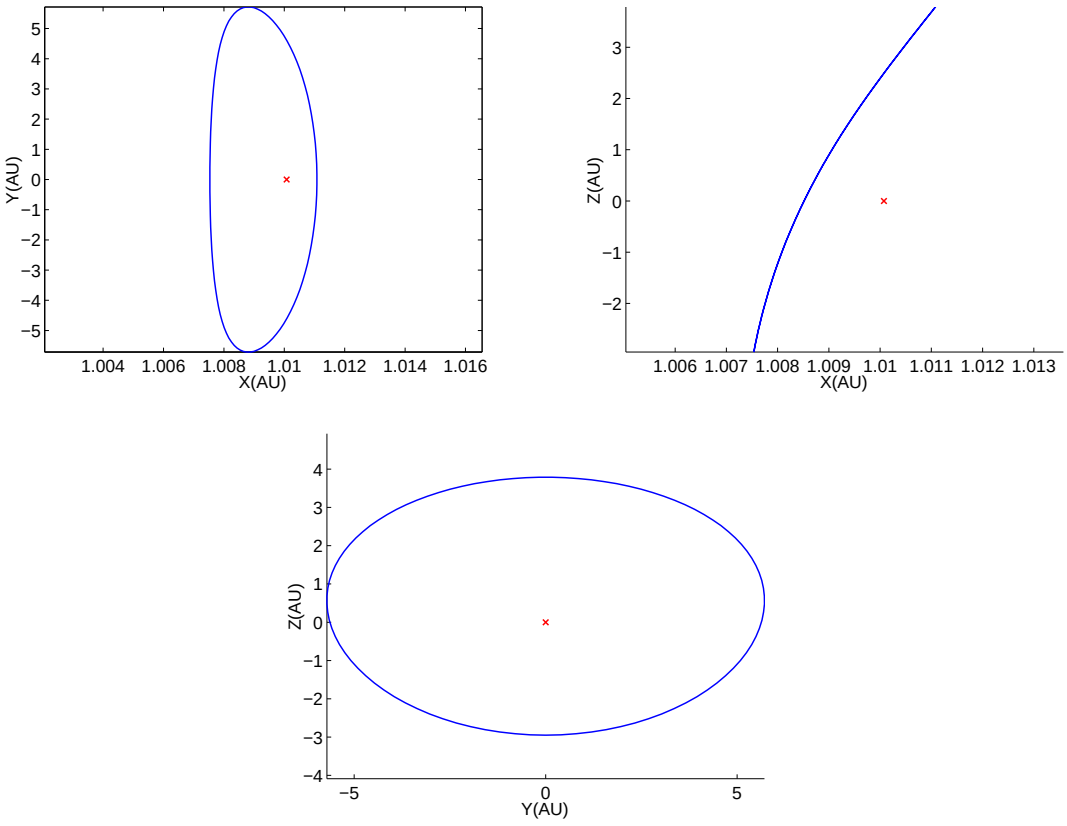

Figure 2.4: Sample northern Halo orbit approximation via the Richardson formulation.

this analysis further to higher orders (see [34]), the Richardson results are adequate

for a quantitative understanding of the Halo orbits and as an initial estimate for the numerical procedure that will be used in the chapters to follow.

2.6 Reduction to Center Manifold

In the previous sections, I first looked at the linear phase space around L2, and then at the higher-order series solutions to find an approximation for the Halo orbits. To gain more insight into the periodic and quasi-periodic librational motions, I now turn to an analysis of the full periodic subspace, i.e. the center manifold around L2. This can be done by separating the periodic and divergent manifolds through the center manifold reduction technique. This method is based on symplectic Lie-transformations on the series expansion of the Hamiltonian. Here, I explain how the center manifold reduction technique is applied to CRTBP, and I summarize the results obtained by Jorba and Masdemont in [35, 36].

2.6.1 Transformation into complex normal form

Introducing new momenta,

$$\begin{aligned} p_x &= x' - y \\ p_y &= y' + x \\ p_z &= z' \,, \end{aligned} \tag{2.54}$$

the corresponding Hamiltonian for equation 2.38 becomes

$$H_{=}\frac{1}{2}(p_x^2 + p_y^2 + p_z^2) + yp_x - xp_y - \sum_{n=2}^{\infty} c_n \rho^n P_n \left(\frac{x}{\rho}\right) \,. \tag{2.55}$$

To be able to apply the Lie series procedure, the quadratic part of the Hamiltonian, which corresponds to the linear ODE, must be in the normal form,

$$\tilde{H}_2 = \lambda\tilde{x}\tilde{p_x} + \nu(\tilde{y}^2 + \tilde{p_y}^2) + \omega_z(\tilde{z}^2 + \tilde{p_z}^2)\,, \tag{2.56}$$

where λ, ν and ω_z are the eigenvalues of the linear ODE system as defined previously. Analyzing the eigenvectors from the last section, it can be shown that the following symplectic transformation takes H_2 into the normal Hamiltonian form $\tilde{H}_2$,

$$\begin{pmatrix} \tilde{x} \\ \tilde{y} \\ \tilde{z} \\ \tilde{p_x} \\ \tilde{p_y} \\ \tilde{p_z} \end{pmatrix} = \begin{pmatrix} \frac{2\lambda}{s_1} & 0 & 0 & 0 & \frac{-2\lambda}{s_1} & \frac{2\nu}{s_2} & 0 \\ \frac{\lambda^2-2c_2-1}{s_1} & \frac{\nu^2-2c_2-1}{s_2} & 0 & \frac{\lambda-2c_2-1}{s_1} & 0 & 0 & \\ 0 & 0 & \frac{1}{\sqrt{\omega_z}} & 0 & 0 & 0 & \\ \frac{\lambda^2+2c_2+1}{s_1} & \frac{\nu^2+2c_2+1}{s_2} & 0 & \frac{\lambda+2c_2+1}{s_1} & 0 & 0 & \\ \frac{\lambda^3+(1-2c_2)\lambda}{s_1} & 0 & 0 & -\frac{\lambda^3-(1-2c_2)\lambda}{s_1} & \frac{\nu^3+(1-2c_2)\nu}{s_2} & 0 & \\ 0 & 0 & 0 & 0 & 0 & \sqrt{\omega_z} & \end{pmatrix} \begin{pmatrix} x \\ y \\ z \\ p_x \\ p_y \\ p_z \end{pmatrix}, \tag{2.57}$$

where,

$$\begin{aligned} s_1 &= \sqrt{2\lambda((4+3c_2)\lambda^2 + 4 + 5c_2 - 6c_2^2)} \\ s_2 &= \sqrt{\omega_z((4+3c_2)\nu^2 - 4 - 5c_2 + 6c_2^2)}\,. \end{aligned} \tag{2.58}$$

Finally, H_2 is transformed into the complex normal form in order to simplify the symbolic numerical manipulations and to keep the notation concise.

$$\begin{pmatrix} q_1 \\ q_2 \\ q_3 \\ p_1 \\ p_2 \\ p_3 \end{pmatrix} = \begin{pmatrix} 1 & 0 & 0 & 0 & 0 & 0 \\ 0 & \frac{1}{\sqrt{2}} & 0 & 0 & -\frac{i}{\sqrt{2}} & 0 \\ 0 & 0 & \frac{1}{\sqrt{2}} & 0 & 0 & -\frac{i}{\sqrt{2}} \\ 0 & 0 & 0 & 1 & 0 & 0 \\ 0 & -\frac{i}{\sqrt{2}} & 0 & 0 & \frac{1}{\sqrt{2}} & 0 \\ 0 & 0 & -\frac{i}{\sqrt{2}} & 0 & 0 & \frac{1}{\sqrt{2}} \end{pmatrix} \begin{pmatrix} \tilde{x} \\ \tilde{y} \\ \tilde{z} \\ \tilde{p_x} \\ \tilde{p_y} \\ \tilde{p_z} \end{pmatrix} \tag{2.59}$$

This transformation brings the quadratic Hamiltonian to its complex normal form,

$$H_2(q,p) = \lambda q_1 p_1 + i\nu q_2 p_2 + i\omega_z q_3 p_3 \,. \tag{2.60}$$

Then the expanded Hamiltonian becomes:

$$\begin{aligned} H(q,p) &= H_2(q,p) + \sum_{n \geqslant 3} H_n(q,p) \\ &= \lambda q_1 p_1 + i\nu q_2 p_2 + i\omega_z q_3 p_3 + \sum_{n \geqslant 3} H_n(q,p)\,, \end{aligned} \tag{2.61}$$

where H_n is the n_{th} order homogenous polynomial of the canonical coordinates and momenta

$$H_n(q,p) = \sum_{\|\mathbf{k}\|^1 = n} h_n^k q_1^{k_1} q_2^{k_2} q_3^{k_3} p_1^{k_4} p_2^{k_5} p_3^{k_6} \;, \tag{2.62}$$

and where the short notation $\mathbf{k} = \{k_1, k_2, k_3, k_4, k_5, k_6\}$ is used with $\| \; \|^1$ as the usual 1-norm given by $\|\mathbf{k}\|^1 = |k_1| + |k_2| + |k_3| + |k_4| + |k_5| + |k_6|$.

2.6.2 The Procedure Explained

The aim of the center manifold reduction is to separate the motion of the center part from the saddle part. This is achieved by applying successive canonical transformations to H, which results in the transformed Hamiltonian, $\bar{H}$, whose exponents of q_1 and p_1 are always the same, i.e. $k_1 = k_4$. Eliminating all the polynomials, where $k_1 \neq k_4$ up to the N_{th} order, we obtain a new Hamiltonian of the following form,

$$\bar{H}(q,p) = \lambda q_1 p_1 + i\nu q_2 p_2 + i\omega_z q_3 p_3 + \sum_{n\geqslant 3}^{N} \bar{H}_n(q_1 p_1, q2, q3, p2, p3) + \mathcal{R}(q,p)\,. \quad (2.63)$$

It is easy to see that $I = q_1 p_1$ is a first integral of motion when the effect of the residue, $\mathcal{R}(q,p)$, is ignored. Using the fact that the time flow of this system is given by Hamilton's equations,

$$\dot{p} = -\frac{\partial H}{\partial q}, \quad \dot{q} = \frac{\partial H}{\partial p}\,, \quad (2.64)$$

the constancy of I can be observed by differentiating it:

$$\begin{aligned} \frac{dI}{dt} &= q_1 \frac{\partial \bar{H}}{\partial p_1} - p_1 \frac{\partial \bar{H}}{\partial q_1} \\ &= 0\,. \end{aligned} \quad (2.65)$$

Hence, if $I = 0$ at time zero, it is zero for all time and the truncated Hamiltonian, $\bar{H}$, is constrained to be a function of only q_2, q_3, p_2, and p_3. The origin of the reduced $\bar{H}(0, q_2, q_3, p_2, p_3)$ system is an elliptic equilibrium point. It is restricted to a manifold tangent to linear center space, hence it is reduced to the center manifold.

2.6.3 Implementation of the Lie Series Method

Center manifold reduction is achieved by using successive canonical transformations, which are almost identity, through the Lie Series method. This method uses the time flow of a generating function, G, to canonically transform the original Hamiltonian into $\bar{H}$ through the following Lie series:

$$\bar{H} = H + [H, G] + \frac{1}{2}[[H, G], G] + \frac{1}{3!}[[[H, G], G], G] + \dots \ , \tag{2.66}$$

where $[\cdot, \cdot]$ is the Lie bracket operator. H is given in equation 2.61 and we want $\bar{H}$ to be of the form given in equation 2.63. As a result, the problem is reduced to finding G in the polynomial equation 2.66. Similar to the expansion of H via the equations 2.61 and 2.62, $\bar{H}$ and G are expanded in power series with the notation,

$$\begin{aligned} G &= G_2 + G_3 + G_4 + \ ... \\ \bar{H} &= \bar{H}_2 + \bar{H}_3 + \bar{H}_4 + \ ... \ , \end{aligned} \tag{2.67}$$

where $\bar{H}_n$ and G_n are n_{th}-order homogenous polynomials given as

$$\begin{aligned} G_n &= \sum_{\|\mathbf{k}\|^1 = n} g_n^k q_1^{k_1} q_2^{k_2} q_3^{k_3} p_1^{k_4} p_2^{k_5} p_3^{k_6} \\ \bar{H}_n &= \sum_{\|\mathbf{k}\|^1 = n,\ k_1 = k_4} \bar{h}_n^k (q_1 p_1)^{k_1} q_2^{k_2} q_3^{k_3} p_2^{k_5} p_3^{k_6} \ . \end{aligned} \tag{2.68}$$

The problem of finding the transformation is now converted into finding the coefficients g_n^k. Using the Lie bracket property that $[H_n, G_m]$ is a homogeneous polynomial of degree $n + m - 2$, the expanded equation is split up into polynomial equations of

increasing degrees:

$$\begin{aligned}
\bar{H}_2 &= H_2 \\
\bar{H}_3 &= H_3 + [H_2, G_3] \\
\bar{H}_4 &= H_4 + [H_2, G_4] + [H_3, G_3] + \frac{1}{2}[[H_2, G_3], G_3] \\
&\ldots
\end{aligned} \tag{2.69}$$

For $\mathbf{k}$ vector values with $k_1 \neq k_4$, $\bar{H}$ is zero. Thus, the equations simplify to

$$\begin{aligned}
0 &= H_3 + [H_2, G_3] \\
0 &= H_4 + [H_2, G_4] + [H_3, G_3] + \frac{1}{2}[[H_2, G_3], G_3] \\
&\ldots
\end{aligned} \tag{2.70}$$

For the first equation, the solution is

$$g_3^k = \begin{cases} \frac{-h_3^k}{(k_4-k_1)\lambda + i(k_5-k_2)\nu + i(k_6-k_3)\omega_z} & \text{for} \quad k_1 \neq k_4 \;\; \& \;\; \|\mathbf{k}\|^1 = 3 \\ 0 & \text{otherwise.} \end{cases} \tag{2.71}$$

Then, the equations given in 2.70 are solved sequentially to first find G_3, then G_4, and so on, in order to obtain the generating function up to a finite truncated order. Since $k_1 \neq k_4$, the denominator term is non-zero, and the series solution diverges very slowly.

Once the manifold reduction is complete and G and $\bar{H}$ have been obtained, the qualitative structure of the center space can be analyzed. In the case of expansion around L2, this manifold is four-dimensional and difficult to visualize. To visualize the qualitative behavior on a two-dimensional figure, the system must be reduced by two more dimensions. This is achieved by first restricting the system to a fixed Hamiltonian and then taking a Poincaré section through the surface $q_3 = 0$. Now we

can see the projection of the system to two dimensions. Figure 2.5 shows a collection of two-dimensional plots representing the dynamics in the periodic phase space with different Hamiltonians.

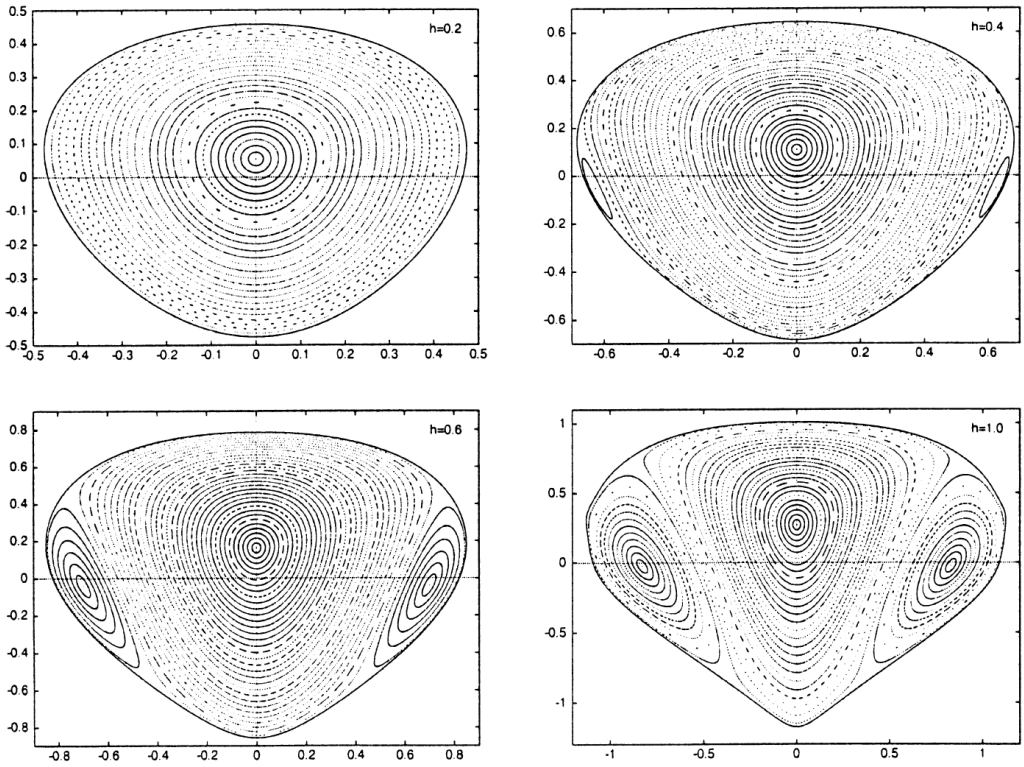

Figure 2.5: Poincaré sections of the center manifold for different Hamiltonian values [36].

While analyzing these plots, it is important to keep in mind that these are Poincaré sections. In other words, the fixed points correspond to periodic orbits in the center manifold, and the closed curves correspond to quasi-periodic orbits. The fixed point at the central part of the plot corresponds to the out-of-plane periodic orbit, whose linear solution is given in Eqn 2.45. Surrounding it are the Lissajous orbits. In the figure, it can be seen that, after a certain increase in the energy level, two lobes appear. These are the north and south Halo orbits, which are surrounded by quasi-periodic orbits called the Quasi-Halos. They bifurcate from the in-plane periodic orbits. These orbits and their properties are discussed in the next chapter.

Chapter 3

Periodic Orbits of Interest around L2: Numerical Methods

The second chapter looked at the dynamical properties and the low-order analytical solutions for the periodic and quasi-periodic orbits around L2 for the simplified CRTBP. In this chapter, I find the real orbits in our solar system that correspond to these analyzed orbits. The chapter proceeds in two sections. The first section explains the numerical tools that are used to find the exact solutions and the stability properties for the periodic orbits in the CRTBP. These methods are then applied to find the horizontal Lyapunov, the vertical Lyapunov, and the Halo orbits, and their stability properties.

3.1 Numerical Tools for Periodic Libration Orbits around L2

Finding periodic orbits of a first order ODE system can be formulated as a boundary value problem (BVP). Shooting algorithms were the first methods to be employed to solve these types of BVPs. Their easy implementation and lack of computational intensity ensures their continued popularity as BVP solving methods. Howell obtained the Halo orbits numerically for the first time using a shooting method, [37].

The accurate analytical approximations for the periodic orbits of interest obtained in the last chapter form the starting points of the numerical algorithms. While the shooting method only uses one point from the analytical approximation, the collocation method uses the whole approximation. This extra information ensures the superior performance of the collocation algorithm. The collocation algorithms have higher accuracy and a bigger region of attraction (minimal need of continuation procedure). In order to verify and confirm the correctness of the results, I implemented both shooting and collocation algorithms to find the periodic orbits of interest.

In addition, as we will see in the last section of this chapter, the collocation algorithm can be modified to transfer these orbits from the CRTBP to a full Solar

System model. For these reasons, I explain the implementation of the collocation algorithms to the CRTBP periodic orbits and refer the reader to [37] for further details on the shooting method.

3.1.1 Collocation as a Numerical Tool to Find Periodic Orbits

If a trajectory $\phi(t, \mathbf{x}_0)$ begins at a point $\mathbf{x}_0$ at time $t = 0$, and at some later time $t = T$ the trajectory $\phi(T, \mathbf{x}_0)$ returns to the point of departure, then this trajectory is called a periodic orbit with period T. Finding periodic orbits of a first-order ODE system can be formulated as a BVP. For a generic system, the problem mathematically reduces to finding the solution $\mathbf{x}(t)$ of the autonomous ODE

$$\dot{\mathbf{x}}(t) = \mathbf{f}(t, \mathbf{x}) \ , \tag{3.1}$$

within the time boundaries

$$0 \leqslant t \leqslant T \ , \tag{3.2}$$

where the system is subjected to boundary conditions which correspond to the periodicity condition, i.e. the trajectory closing on itself:

$$\mathbf{g}(\mathbf{x}(0), \mathbf{x}(T)) = \mathbf{x}(0) - \mathbf{x}(T) = 0. \tag{3.3}$$

After formulating the computation of the periodic orbit as a BVP, the state vector, $\mathbf{x}(t)$, which is subjected to the differential equation and boundary constraints, is solved. To implement the problem on a digital computer, the time and state variables

are discretized at $N+1$ points along the trajectory

$$\begin{aligned} 0 = t_0 < t_1 \ \ldots \ < t_i < \ldots < t_{N-1} < t_N = T\,, \\ \mathbf{x}_0 = \mathbf{x}(0),\ \ldots,\ \mathbf{x}_i = \mathbf{x}(t_i),\ \ldots,\ \mathbf{x}_N = \mathbf{x}(T)\,. \end{aligned} \tag{3.4}$$

Now, we need to find the discrete relationship that corresponds to the ODE

$$\dot{\mathbf{x}}(t) - \mathbf{f}(t, \mathbf{x}) = 0 \Rightarrow F(t_i, \mathbf{x}_i, t_{i+1}, \mathbf{x}_{i+1}) = 0\,. \tag{3.5}$$

There are schemes that can be used for this discretization. Among the most popular are the Runge-Kutta formulas and the Simpson's quadrature. Cash and his colleagues have developed a number of effective solvers - for example, Cash and Wright TWBVP [38, 39], where the basic formula is Simpson's rule for quadrature. In the BVP solver COLNEW, Ascher et al. [40, 41], implemented a family of implicit Runge-Kutta methods. I used the Kierzenka et al.'s [42] *bvp4c* implementation, where a Simpson's formula for the quadrature is implemented. One advantage of this implementation is that the discretized equations can be analytically solved without intermediate variables. If the initial guess is sufficiently close to the real solution, the discretized Simpson quadrature equation, which corresponds to the differential equation, gives the following constraint at every point:

$$\begin{aligned} F(\mathbf{x}_i) = \quad & -\mathbf{x}_{i+1} + \mathbf{x}_i + \frac{h_i}{6}\left(\mathbf{f}(t_i, \mathbf{x}_i) + \mathbf{f}(t_{i+1}, \mathbf{x}_{i+1})\right) \ldots \\ & + \frac{2h_i}{3}\mathbf{f}\left(\frac{t_i + t_{i+1}}{2}, \frac{\mathbf{x}_i + \mathbf{x}_{i+1}}{2} - \frac{h_i}{8}\left[\mathbf{f}(t_i, \mathbf{x}_i) - \mathbf{f}(t_{i+1}, \mathbf{x}_{i+1})\right]\right)\Big]\,, \end{aligned} \tag{3.6}$$

where

$$h_i = t_{i+1} - t_i. \tag{3.7}$$

In order to obtain the full discrete version of the BVP, the constraint vector is augmented with the constraints at the boundaries:

$$F_0(\mathbf{x}_0, \mathbf{x}_N) = \mathbf{g}(\mathbf{x}_0, \mathbf{x}_N) \ . \tag{3.8}$$

Solving for this set of equations is equivalent to a general finite difference implementation. The correct solution is obtained when constraint equations are equal to zero. The $N + dim(g)$ dimensional nonlinear equation given by $[F_0, F(\mathbf{x}_i)] = 0$ is solved using Newton's method, where an initial guess $\mathbf{q}^0 = \{\mathbf{x}_0, \mathbf{x}_1, ..., \mathbf{x}_{N-1}, \mathbf{x}_N\}$ is iterated according to

$$DF(\mathbf{q^{j-1}}) \cdot (\mathbf{q^j} - \mathbf{q^{j-1}}) \ = \ -F(\mathbf{q^{j-1}}) \ . \tag{3.9}$$

Before taking the next Newton step, the accuracy of the current guess is assessed and the values are redistributed.

The full state along the trajectory is approximated by a piecewise polynomial, $\mathbf{S}(t, \mathbf{q^j})$. Employing Hermite cubic polynomials, a $\mathcal{C}^1$ representation that interpolates $\mathbf{x}$ and $\dot{\mathbf{x}}$ for each subinterval $[x_i, x_{i+1}]$ is constructed as

$$S(t, \mathbf{q^j}) = A_1(t)\mathbf{x}_i + A_2(t)\mathbf{x}_{i+1} + B_1(t)\dot{\mathbf{x}}_i + B_2(t)\dot{\mathbf{x}}_{i+1} + \mathcal{O}(h^4) \ , \tag{3.10}$$

where $A_1(t)$, $A_2(t)$, $B_1(t)$, $B_2(t)$ are the third-order Hermite polynomial function, which satisfies the continuity boundary conditions for each subinterval $[x_i, \ x_{i+1}]$ of the mesh.

Once the approximation for the continuous solution by this spline is obtained, the estimate of the error norm in the current stage of iteration is needed to make decisions for the following iteration steps. Defining the residue between the spline and the real

solution as

$$r(t)^j = \mathbf{S}'(\mathbf{x}^j) - f(\mathbf{x}^j, \mathbf{S}(\mathbf{x}^j)) \ , \tag{3.11}$$

the error norm is calculated by integration of the residue between the spline and the real solution by a 5-point Lobatto quadrature approximation [43] on each subinterval i:

$$||r(\mathbf{x}^j)||_i = \left(\int_{x_i}^{x_i+1} ||r(\mathbf{x}^j)||^2 \right)^{1/2} . \tag{3.12}$$

Based on the norm of the residual of the continuous solution, the mesh points, $\mathbf{x}^j$, are redistributed. Extra points are added to the intervals with residues larger than minimum error tolerance, and the points on the intervals which have errors much smaller than the minimum tolerance are removed. Then, the Newton's iteration is continued until $||r(\mathbf{x}^j)|| < \epsilon$, where ϵ is a preset tolerance for the BVP solution. Then, it is assumed that the iteration converged and that the correct answer is obtained.

3.1.2 Stability Analysis of Periodic Orbits

The stability of an orbit of a dynamical system determines whether nearby orbits will stay in close proximity to that orbit or be repelled from it as time progresses. The Poincaré map enables us to determine the stability of a periodic orbit for a time-independent dynamical system (for a detailed mathematical explanation, see Guckenheimer & Holmes [44]). It does so by converting the n-dimensional continuous dynamical system into an $(n-1)$-dimensional map.

Let us consider surface section Σ, a subspace with a dimension lower than the dynamical system of interest, that is transversal to the flow direction. A first return map or Poincaré map is the intersection of a periodic orbit, $x(t)$, in the state space of the continuous dynamical system with Σ. If we consider a periodic orbit with initial

conditions, x_0, on the Poincaré section and observe the successive points at which this orbits returns to the section, x_i, we can reduce the dynamical system to the following map

$$x_{i+1} = P(x_i) \tag{3.13}$$

on the section Σ section. The periodic orbit of the dynamical system becomes the fixed point of the map P when

$$x_0 = P(x_0)\,. \tag{3.14}$$

Thus, the transformation converts the condition for the stability of the periodic orbit to determining the stability of the map P. In order to study the stability of the Poincaré map, it is linearized around the fixed point

$$\delta x_{i+1} = \mathrm{D}P(x_0)\delta x_i. \tag{3.15}$$

The fixed point of this map, x_0, is asymptotically stable if the moduli of all the eigenvalues of $\mathrm{D}P$ are less than one and unstable if any of the eigenvalues are outside the unit circle. The stability of the periodic orbit is determined by the fixed point of the map.

Floquet theory offers an attractive numerical alternative to determining the stability of a periodic orbit without employing Poincaré maps. Instead of using a section in the phase space, we linearize the T-periodic vector field around the periodic orbit. Solving the linearized equations, we obtain the Floquet multipliers that define the rate of convergence or divergence of small perturbations from the periodic orbit. Guckenheimer and Holmes prove that one of the Floquet multipliers is unity with the eigenvector corresponding to motion along the periodic orbit, and that the $(n-1)$

eigenvalues of DP are equal to $(n-1)$ of the Floquet multipliers of the periodic orbit [44].

In what follows, I investigate the stability of one particular periodic solution $x(t)$ with period T of the autonomous system given as: $\dot{x} = f(x)$. I proceed by linearizing the T-periodic vector field around the periodic orbit $\phi(t, x_0)$. First, let us note that the trajectory satisfies its own ODE,

$$\frac{d}{dt}\frac{\partial \phi(t,x_0)}{\partial x_0} = f(\phi(t,x_0)), \quad \text{with} \quad \phi(0,x_0) = x_0 \ . \tag{3.16}$$

Differentiating this equation with respect to x_0, we obtain

$$\frac{d}{dt}\frac{\partial \phi(t,x_0)}{\partial x_0} = Df(\phi)\frac{\partial \phi(t,x_0)}{\partial x_0}, \quad \text{with initial condition} \quad \frac{\partial \phi(0;x_0)}{\partial x_0} = I. \tag{3.17}$$

Rewriting equation 3.17 in terms of the state transition matrix, $\Phi(t)$, where $\Phi(t) := \frac{\partial \phi(t,x_0)}{\partial x_0}$, we obtain

$$\dot{\Phi} = Df(x)\Phi, \quad \Phi(0) = I \ . \tag{3.18}$$

The monodromy matrix, M, of a periodic solution, $x(t)$, with period T and initial condition x_0, is defined as

$$M := \Phi(T) = \frac{\partial \phi(T,x_0)}{\partial x_0} \ . \tag{3.19}$$

The eigenvalues of the monodromy matrix are the Floquet multipliers [44]. They define the full stability properties of the periodic orbit of interest. We can see this by looking at how much a perturbed trajectory $\phi(t, x_0+\delta x_0)$ separates from the periodic trajectory $\phi(t, x_0)$ after one period.

$$\delta x(T) \quad = \quad \phi(T, x_0 + \delta x_0) - \phi(T, x_0) \ . \tag{3.20}$$

Expanding the right hand side of the equation in Taylor series gives the approximation

$$\begin{aligned} \delta x(T) &= \frac{\partial \phi(T, x_0)}{\partial x_0} \delta x_0 \quad + \text{high order terms} \\ &\approx M \delta x_0. \end{aligned} \tag{3.21}$$

Thus, M quantifies how perturbations on initial conditions progress after one period. All we need to do to understand the stability of the periodic orbit of interest is to integrate the equation 3.18 from $t = 0$ to $t = T$, and then check the eigenvalues of M, i.e. the Floquet multipliers. If the Floquet multipliers are less than one then the orbit is stable, if one of them is larger than one then the orbit is unstable. While the eigenvectors define the stable and unstable direction, the magnitude of the eigenvalue define the rate of convergence or divergence.

3.2 Application to the Periodic Orbits of the CRTBP Around L2

The linear six-dimensional phase space around L2 is a *center* $\times$ *center* $\times$ *saddle* as discussed in the second chapter. For energy values close to that at L2, where it is sufficient to consider only the linear approximation to the equations of motion, there exist two families of periodic orbits; the horizonal Lyapunov orbits, which are in the ecliptic plane, and the horizontally symmetric figure-eight-shaped vertical Lyapunov orbits. As the energy is increased, and nonlinear terms become important, the linear phase space is broken and a new periodic family, Halo orbits, bifurcates from the horizontal Lyapunov orbit family. These orbits are three-dimensional and asymmetric about the ecliptic plane.

In this section, I explain how the numerical tools of the previous section can be used to obtain and analyze all the periodic orbits in the vicinity of L2. These three

periodic orbits, namely, horizontal Lyapunov, vertical Lyapunov, and Halo orbits, are studied in the following subsections.

First, the orbit finding problem is converted to the canonical form for the implementation of the collocation algorithm. Rewriting the CRTBP ODE given as equation 2.9 in the first-order form, with the state vector $\mathbf{x} = \{x,\ y,\ z,\ \dot{x},\ \dot{y},\ \dot{z}\}$, we obtain

$$\dot{\mathbf{x}} = \mathbf{f}(\mathbf{x}) = \begin{pmatrix} \dot{x} \\ \dot{y} \\ \dot{z} \\ 2\dot{y} + \frac{\partial \bar{U}}{\partial x} \\ -2\dot{x} + \frac{\partial \bar{U}}{\partial y} \\ \frac{\partial \bar{U}}{\partial z} \end{pmatrix} . \tag{3.22}$$

Although we have approximations for the periods of the periodic orbits, we do not know the exact period. For the collocation algorithm to work, we need to explicitly define the time boundaries for the BVP. However, in our case, the time interval is $[0,\ T]$, where the end time, T, for the BVP is an unknown parameter. To overcome this problem, I redefine the system on the fixed time interval $[0,\ 1]$ by rewriting the equation in terms of a new time variable

$$\tau = \frac{t}{T} . \tag{3.23}$$

Introducing T as a new state variable, the extended differential equation becomes

$$\begin{aligned} \frac{d\mathbf{x}}{d\tau} &= T \cdot \mathbf{f}(\mathbf{x}) \\ \frac{dT}{d\tau} &= 0 . \end{aligned} \tag{3.24}$$

The collocation algorithm is used on this modified system.

After finding the periodic orbit, the stability analysis is conducted. The Jacobian of the differential equation that is used in equation 3.18 to integrate the state transformation, Φ, and find Monodromy matrix, M, is

$$\mathrm{D}\mathbf{f} = \begin{pmatrix} 0 & I \\ \bar{U}^*_{xx} & 2\Omega \end{pmatrix} , \tag{3.25}$$

where 0 is the 3×3 zero matrix, I is the 3×3 identity matrix, $\bar{U}^*_{xx}$ is the matrix of symmetric second partial derivatives of U with respect to x, y and z,

$$\bar{U}^*_{xx} = \begin{pmatrix} \bar{U}_{xx} & \bar{U}_{xy} & \bar{U}_{xz} \\ \bar{U}_{yx} & \bar{U}_{yy} & \bar{U}_{yz} \\ \bar{U}_{zx} & \bar{U}_{zy} & \bar{U}_{zz} \end{pmatrix} , \tag{3.26}$$

and Ω is

$$\Omega = \begin{pmatrix} 0 & 1 & 0 \\ -1 & 0 & 0 \\ 0 & 0 & 0 \end{pmatrix} . \tag{3.27}$$

Now we define a new 42-dimensional augmented state vector consisting of the 6-dimensional state vector and the 36-dimensional state transition matrix: $\mathbf{x_{aug}} = [\mathbf{x}; \Phi(:)]$. Integrating the augmented state vector, $M = \Phi(T)$ is obtained.

Before going into the details of each orbit calculation, I would like to point out some of the properties of the eigenvalues of the monodromy matrix of the periodic orbits of the CRTBP. Since this is a map, an eigenvalue of +1 indicates a stationary mode, and an eigenvalue of modulus one indicates a rotational mode. An eigenvalue of modulus greater than +1 indicates the exponentially growing mode and a modulus less than one indicates an exponentially decaying mode. As the direction along the

periodic orbit will always come back to the same point on the map, M always has $+1$ as an eigenvalue, with the corresponding eigenvector tangent to the periodic orbit direction at x_0. Since the CRTBP is an autonomous Hamiltonian system, it has an energy integral, the Jacobi Constant, which means that the periodic orbits come in families. Thus, there will be another stationary mode and another $+1$ eigenvalue of M, which is in the direction of the periodic orbit family, and the eigenvalue $+1$ has an algebraic multiplicity of at least two. Moreover, M is symplectic for autonomous Hamiltonian systems. Hence, if λ is an eigenvalue of M, then λ^{-1}, $\bar{\lambda}$ (conjugate of λ), and $\bar{\lambda}^{-1}$ are also eigenvalues of M, with the same multiplicity. To sum up, at least two of the eigenvalues of M will be $+1$ and the other four will have to be such that the conjugate and the inverse of these eigenvalues have to be eigenvalues as well. These properties are useful for the stability analysis of the CRTBP orbits.

3.2.1 Horizontal Lyapunov Orbits

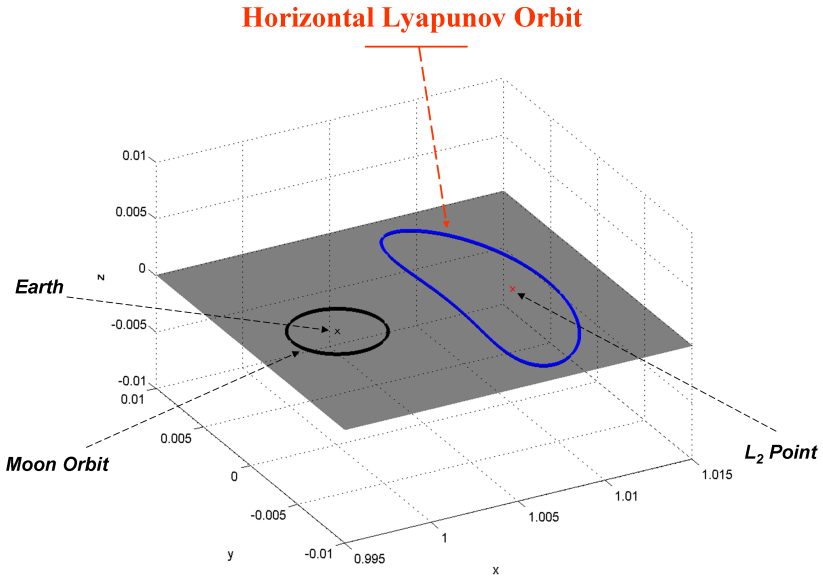

Figure 3.1: Horizontal Lyapunov periodic orbit around L2 libration point

The first type of periodic orbits are the horizontal Lyapunov orbits, which are constrained to the x-y plane. As a result, $z = \dot{z} = 0$ throughout the trajectory. In addition, the CRTBP dynamical system, which was defined in equation 3.22, is invariant under the transformation

$$\{x(t), y(t), z(t)\} \Rightarrow \{x(-t), -y(-t), z(-t)\}\,. \tag{3.28}$$

Due to this invariance, the solution of the horizontal Lyapunov orbits will be symmetric with respect to the y plane and will cross the y plane perpendicularly [37]. Thus, at $y(0) = 0$, the periodic horizontal Lyapunov orbit has to satisfy

$$y(0) = 0,\ z(0) = 0,\ \dot{x}(0) = 0,\ \dot{z}(0) = 0\,. \tag{3.29}$$

These constraints simplify the problem such that for a given $x(0) = x_0$, we only need to find $\dot{y}(0)$ to specify a horizontal Lyapunov orbit. When choosing the boundary condition, we need to be careful to avoid the degenerate solution, where $\mathbf{x}(0) = \mathbf{x}(1)$ with $T = 0$. However, the degenerate solution becomes infeasible if we set $\dot{y}(0)$ to a constant value, $\dot{y}_0$, as the initial condition, instead of setting $x(0) = x_0$. The constant $\dot{y}_0$ is the orbit size parameter. Changing this parameter enables us to find periodic orbits with different sizes and energies. Keeping these considerations in mind, I set

the boundary value problem as follows:

$$
\begin{aligned}
x(0) &= x(1), \\
y(0) &= y(1) = 0, \\
z(0) &= z(1) = 0, \\
\dot{x}(0) &= \dot{x}(1) = 0, \\
\dot{y}(0) &= \dot{y}(1) = \dot{y}_0, \\
\dot{z}(0) &= \dot{z}(1) = 0 \ .
\end{aligned} \tag{3.30}
$$

I then solve the BVP with the differential equation 3.24 and the boundary condition equation 3.30, using the initial estimate from equation 2.45. Figure 3.1 shows a typical horizontal Lyapunov periodic orbit around the Sun-Earth L2 point, which is found with this method. By varying the $\dot{y}_0$ parameter, periodic orbits on different energy levels are solved using collocation. The full horizontal Lyapunov family is obtained as shown in figure 3.2.

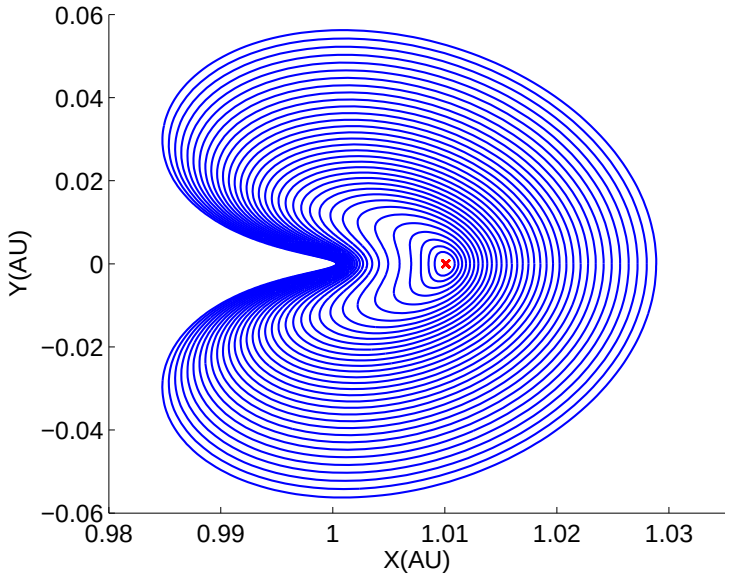

Figure 3.2: Horizontal Lyapunov Family around L2

The stability of these orbits is studied via their monodromy matrices. This four-dimensional in-plane system has four eigenvalues. Two eigenvalues are equal to +1. These correspond to the neutral directions, namely, the tangent direction to the periodic orbit, and the variation in the energy level sets. The two positive eigenvalues, λ and $1/\lambda$, where λ is a very large parameter on the order of 10^3, correspond to the unstable and stable modes, respectively. λ decreases as the size of the orbit increases.

3.2.2 Vertical Lyapunov Orbits

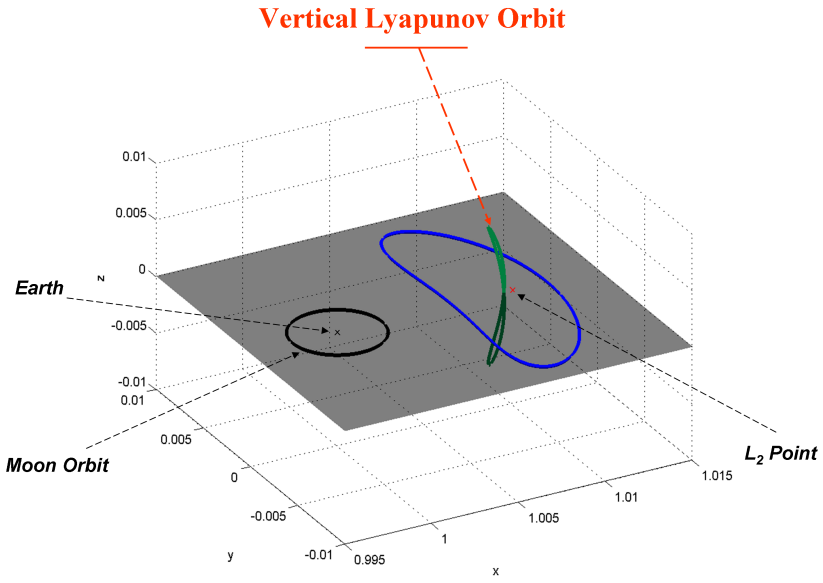

Figure 3.3: Vertical Lyapunov periodic orbit around L2 libration point

The second type of periodic orbit around L2 is the vertical Lyapunov orbit, where the vertical motion dominates, even though the trajectory has components in all three dimensions. These orbits are symmetric with respect to the z plane, and their shape resembles the figure eight, crossing the z plane at a single point. As discussed in the previous section, the solution of the vertical Lyapunov orbits will be symmetric with respect to the y plane and thus will cross the y plane perpendicularly. This partitions

the vertical Lyapunov orbit into four symmetric parts. Instead of obtaining the whole orbit, it is thus sufficient to find one of the symmetric parts, and this reduces the computation time. As the orbit crosses the y plane at time zero, the periodic vertical Lyapunov orbit has to satisfy

$$y(0) = 0,\ \dot{x}(0) = 0,\ \dot{z}(0) = 0\ . \tag{3.31}$$

At $t = 1/4$, the orbit crosses the y and z planes

$$y(1/4) = 0,\ z(1/4) = 0,\ \dot{x}(1/4) = 0\ . \tag{3.32}$$

As before, to avoid the degenerate solution, where $\mathbf{x}(0) = \mathbf{x}(1/4)$ with $T = 0$, I specify an initial condition that makes the degeneracy infeasible. I choose $\dot{z}(1/4) = \dot{z}_{1/4}$ as the orbit size parameter.

$$\begin{aligned} y(0) = y(1/4) &= 0, \\ \dot{x}(0) = \dot{x}(1/4) &= 0, \\ \dot{z}(0) &= 0, \\ z(1/4) &= 0, \\ \dot{z}(1/4) &= \dot{z}_{1/4}\ . \end{aligned} \tag{3.33}$$

I solve the BVP with differential equation 3.24 and the boundary condition equation 3.33, using the initial guess from equation 2.45. Figure 3.3 shows a typical vertical Lyapunov periodic orbit around L2 found by using this method. By varying the $\dot{z}_{1/4}$ parameter, periodic orbits on different energy levels are solved using collocation and the full vertical Lyapunov family is obtained as shown in figure 3.4.

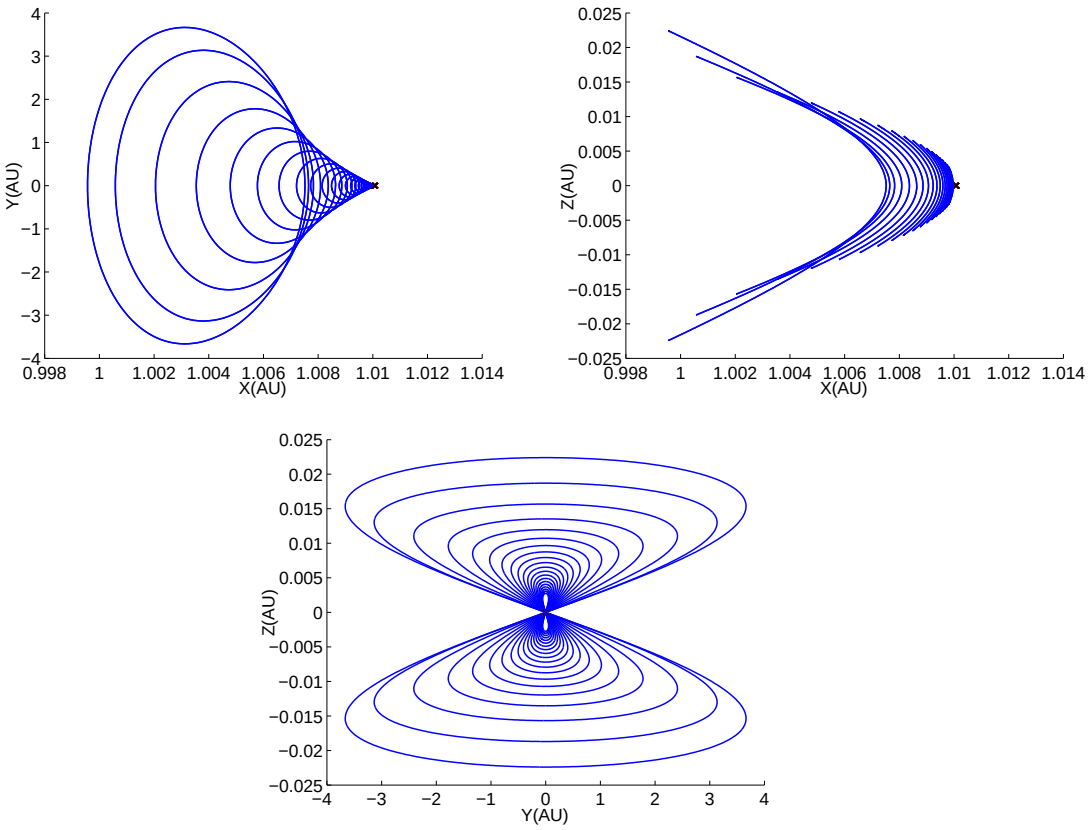

Figure 3.4: Vertical Lyapunov Family around L2

The stability of these orbits is studied via their six-dimensional monodromy matrices. This six-dimensional system has six eigenvalues, two of which are equal to +1. These correspond to the neutral directions, namely, the tangent direction to the periodic orbit and the variation in the energy level sets. The two positive eigenvalues, λ and $1/\lambda$, where λ is a very large parameter on the order of 10^3, correspond to the unstable and stable modes, respectively. λ decreases as the size of the orbit increases. In addition, there is an eigenvalue couple, $cos(\sigma) \pm isin(\sigma)$ with modulus 1, which corresponds to the periodic mode. As the size of the orbit increases, the σ value increases from zero moving the eigenvalues on the unit circle.

3.2.3 Halo Orbits

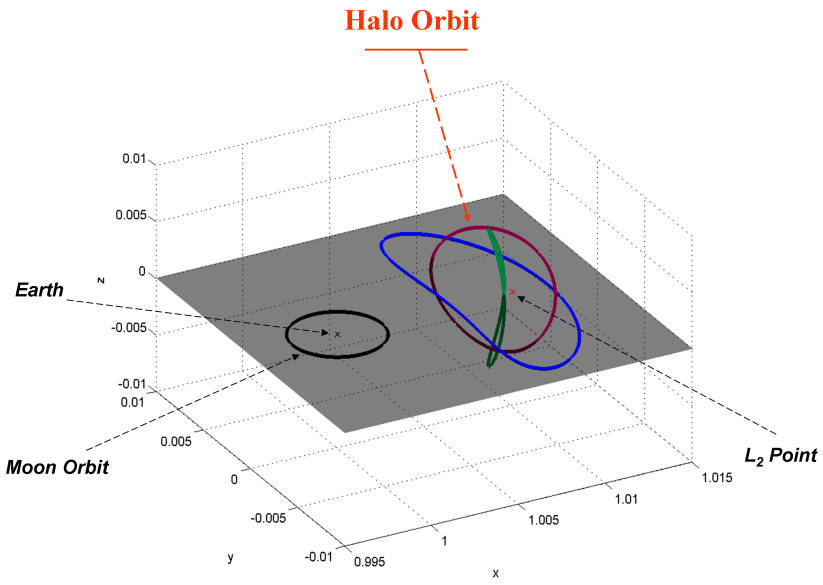

Figure 3.5: Halo periodic orbit around L2 libration point.

The third type of periodic orbit is the Halo orbit. These three-dimensional orbits are described analytically in detail in section 2.5. As before, the solution of the Halo orbits will be symmetric with respect to the y plane and cross the y plane perpendicularly, partitioning the Halo orbit into two symmetric parts. It is thus sufficient to obtain one of the symmetric parts, rather than having to find the whole orbit. This reduces the computation time. As the orbit crosses the y plane at time zero, the halo orbit has to satisfy

$$y(0) = 0,\ \dot{x}(0) = 0,\ \dot{z}(0) = 0\ . \tag{3.34}$$

As before, to avoid the degenerate solution where $\mathbf{x}(0) = \mathbf{x}(1/2)$ with $T = 0$, I specify an initial condition that makes the degeneracy infeasible. I choose $\dot{y}(0) = \dot{y}_0$ as the orbit size parameter. Changing this parameter enables us to find periodic orbits with

different energy levels. So, I set the boundary value problem as follows:

$$\begin{aligned} y(0) &= y(1/2) = 0, \\ \dot{x}(0) &= \dot{x}(1/2) = 0, \\ \dot{y}(0) &= \dot{y}_0, \\ \dot{z}(0) &= \dot{z}(1/2) = 0\ . \end{aligned} \tag{3.35}$$

I solve the BVP with differential equation 3.24 and the boundary condition equation 3.35, using the initial estimate from equation 2.52. Figure 3.5 shows a typical northern Halo periodic orbit around L2 that was found with this method. By varying the $\dot{y}_0$ parameter, periodic orbits on different energy levels are solved using collocation, and the full northern Halo family is obtained, as shown in figure 3.6. The CRTBP dynamical system, which is defined in equation 3.22, is invariant under the transformation

$$\{x(t), y(t), z(t)\} \Rightarrow \{x(t), y(t), -z(t)\}\ . \tag{3.36}$$

Due to this invariance,there is a mirror symmetry across the $z = 0$ plane. Therefore, there is also a southern Halo orbit family which is the mirror copy of the northern family with respect to the z plane (not shown on figure 3.6).

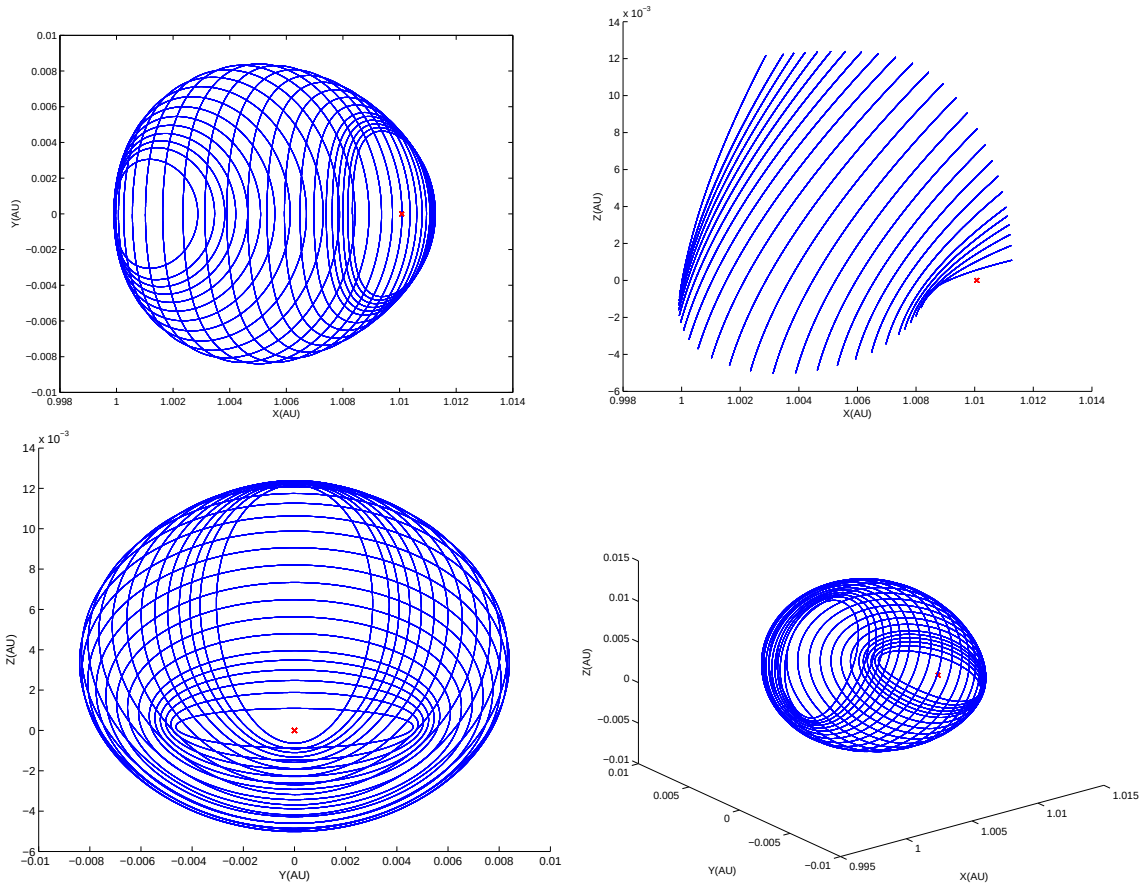

Figure 3.6: Northern Halo orbit family around L2 libration point

The stability of these orbits is studied via their six-dimensional monodromy matrices. This six-dimensional system has six eigenvalues. Two eigenvalues are equal to $+1$, and correspond to the neutral directions, namely, the tangent direction to the periodic orbit and the variation in the energy level sets. The two positive eigenvalues, λ and $1/\lambda$, where λ is a very large parameter on the order of 10^3, correspond to the unstable and stable modes, respectively. λ decreases as the size of the orbit increases. In addition, there is an eigenvalue couple, $cos(\sigma) \pm isin(\sigma)$ with modulus 1, which corresponds to the periodic mode. As the size of the orbit increases, the σ value increases from zero moving the eigenvalues on the unit circle. For a more detailed bifurcation analysis of the halo orbits, please see [45].

Chapter 4

Multiple Poincaré Sections Method for Finding the Quasi-Halo and Lissajous Orbits

There are three main challenges associated with finding quasi-periodic orbits. The first is to minimize the time it takes to program the software that numerically solves for the orbits. This reduces the threshold for researchers who work on trajectory design. The second is to achieve reasonable execution times, allowing results to be obtained quickly and "on the go". The third is to improve the robustness of the method in order to map the very large regions of attraction that are needed to obtain the full families of quasi-periodic orbits.

Symbolic methods such as the Lindstedt-Poincaré method by Gómez et al. [46] and the reduction to the center manifold by Jorba et al. [36, 47], which depend on series expansions, are very slow because an exponential increase in the number of coefficients is needed for every additional increase in the order of expansion. The speed problem can be overcome to a great extent by programming a symbolic manipulator for the problem of interest, but this leads to a significant increase in programming time. More importantly, some of these techniques have instability problems near resonances.

This led to the consideration of fully numeric methods. However, instead of taking a mesh on the whole surface, which requires many points and is thus memory and CPU intensive, I considered only a section on the torus containing the quasi-periodic trajectories, thus representing the full torus by only points on this section. This is an invariant circle. These points on the invariant circle must be integrated for one period at each iteration step. The initial errors in the estimation of the section increase exponentially with the highest Lyapunov exponent as the integration time increases. This is of great concern, especially for the CRTBP L2 case where the Lyapunov exponent is more than 10^3. The effect is more dramatic near resonant and chaotic regions. To overcome this problem, I reduce the integration times by taking multiple sections on the torus, integrating only between the consecutive Poincaré sections. The methodology is parallel to the multiple shooting method used in two-point boundary

value problems [48].

This chapter consist of four sections. In the first section, I explain the main idea of the procedure without going into details of the numerical implementation. Here, I first introduce the methodology by explaining the procedure for a single Poincaré section. The results are then extended to multiple Poincaré sections. I discuss different implementations using various Poincaré surfaces. A continuation method to find the full family of quasi-periodic orbits is introduced.

In the second section, numerical details for obtaining the real quasi-periodic orbits around L2 are explained.

The third section presents the results section, where I give the solutions for the quasi-periodic orbits around L2 of the CRTBP, the Lissajous and the Quasi-Halo orbits, and show the full periodic family and compare the results with the literature.

In the last section, I explain and apply the numerical method to "transfer" these orbits from the CRTBP model to the real ephemeris model of the Solar System.

This chapter is based on previous work by Kolemen and Kasdin [49].

4.1 Procedure

4.1.1 Finding Invariant Tori via a Single Poincaré Section

For the occulter-based telescopy mission under study, the main quasi-periodic orbits of interest are the Quasi-Halos which lie on two-dimensional invariant manifold. As discussed in the introductory section, the multiple Poincaré section procedure aims to reduce the problem of finding the two-dimensional invariant manifold of the full ordinary differential equation to finding the invariant circles, i.e., the one-dimensional invariant manifold of the Poincaré map. These invariant circles compactly define the full two-dimensional manifold.

The first step in the single Poincaré section procedure is to find a convenient

Poincaré section. This can be a section in any of the 6-dimensional phase-space coordinates including the position and/or the velocity elements of the state. Figure 4.1 shows the projection to the position space of a torus and its intersection with a Poincaré section.

When choosing the plane of the section, the main concern is to ensure that the velocity vector of the quasi-periodic orbit is as transverse to the surface of section, Σ, as possible. This reduces the possibility that the integrated points will not return to the Poincaré section. Thus, a good candidate for the Poincaré section is the plane perpendicular to the velocity of the Halo orbit section. For the specific case of the CRTBP, another suitable plane-of-section is the ecliptic plane, since the type of quasi-periodic orbits of interest by their nature transversely cross this plane. I used both types of Poincaré sections for the results in this dissertation.

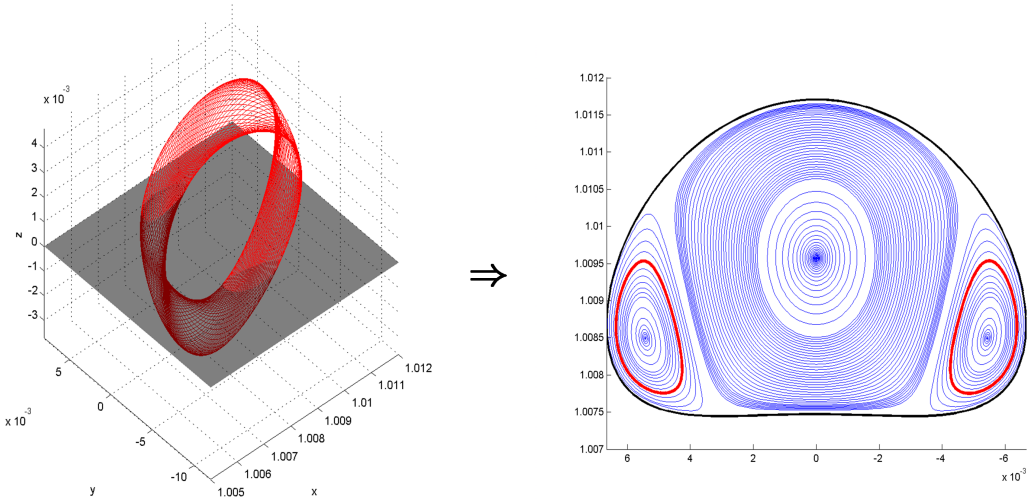

Figure 4.1: Converting the search for a torus problem of a differential equation to the search of the circle of a map

I expand the invariant circle, γ, in a truncated Fourier series with the expansion parameter $\theta \in [0,\, 2\pi)$, the angle parameter on the invariant circle,

$$\gamma(\theta) = \frac{a_0}{\sqrt{2}} + \sum_{n=1}^{n_{max}} \left[a_n \cos(n\theta) + b_n \sin(n\theta)\right] , \tag{4.1}$$

where n_{max} is the truncation order of the Fourier series expansion.

Here, the choice of the angle parameter, θ, is problem-dependent. In the case where the Poincaré section is taken on the ecliptic plane, i.e., $z = 0$, an intuitive angle parameter is $\theta = atan(\frac{y-y_{halo}}{x-x_{halo}})$. It is important to note that the system must be parameterized such that every point on the invariant circle is uniquely defined by one value of the parameter, $\gamma(\theta_i)$. For invariant circles with complex shapes, other parameters, such as the ratio of the arc length between a specific point on the circle and the full arc length of the closed orbit [50], should be used to ensure uniqueness. For the CRTBP, however, this simple parameter gives satisfactory results.

I then take N points on the invariant circle by choosing a set of angle variables in the interval $[0,\, 2\pi)$,

$$\theta_0(i) = \frac{2\pi i}{N} \quad i = 0, 1, \ldots, N-2, N-1 \; . \tag{4.2}$$

Every element of the angle vector, $\theta_0(i)$, corresponds to a six-dimensional coordinate vector, $\mathbf{x_i}$, on the phase space. Concatenating these coordinate vectors, a $6 \times N$-dimensional coordinate vector, $\mathbf{X_0}$, is obtained, which can be expressed as:

$$\mathbf{X_0} = \frac{a_0}{\sqrt{2}} + \sum_{n=1}^{n_{max}} [a_n \cos(n\theta_0) + b_n \sin(n\theta_0)] \; . \tag{4.3}$$

Since this is a linear transformation, it can be expressed as a matrix multiplication:

$$\mathbf{X_0} = A_{\theta_0}\mathbf{Q} \; , \tag{4.4}$$

where $\mathbf{Q}$ is the truncated Fourier coefficients vector and A_θ is the discrete Fourier matrix that takes Fourier coefficients to coordinate variables. I map these points, $\mathbf{P}(\mathbf{X_0})$, by integrating the equations of motion until they intersect the Poincaré section:

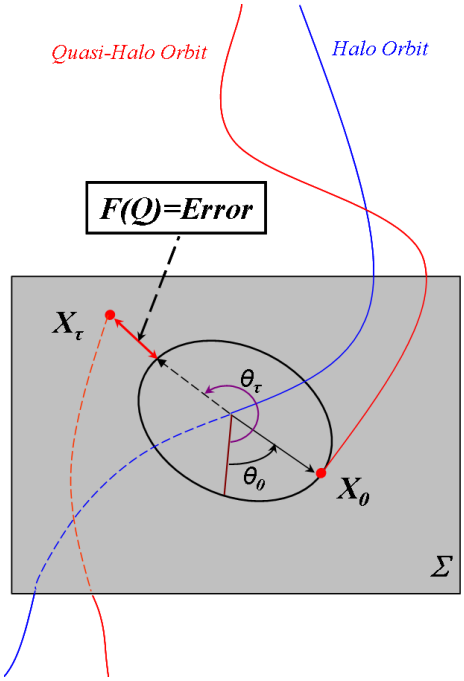

Figure 4.2: Schematic illustration of the numerical procedure for finding the invariant torus

$$\mathbf{X}_\tau \;=\; \mathbf{P}(\mathbf{X_0}) \;=\; \phi(\tau(\mathbf{X_0}), \mathbf{X_0})\,. \tag{4.5}$$

Here, $\tau(\mathbf{X_0})$ is the time it takes for a given set of points, $\mathbf{X_0}$, to reach to the Poincaré section, Σ. Recall also that the notation $\phi(t, x_0)$ is used for the flow of the ODE from a given initial condition, x_0, for the specified time, t. The first variations of these equations are integrated along with $\mathbf{X_0}$ for later use in the iteration process.

If all the mapped points, $\mathbf{X}_\tau$, fall exactly on the guessed invariant circle, this means that the initial guess for the invariant circle is indeed correct. Using this intuition, it is possible to set up a numerical scheme in order to find the correct parameterization of the quasi-periodic orbit. The schematic illustration of this numerical scheme is shown in figure 4.2, where the error vector to be minimized, i.e., $F(\mathbf{Q})$, is expressed. Thus, finding the quasi-periodic orbit is equivalent to finding the Fourier coefficient vector, $\mathbf{Q}$, which minimizes the distance between the mapped points $\mathbf{X}_\tau$ and the

invariant circle. This condition can be written in mathematical terms as:

$$F(\mathbf{Q}) \;=\; \mathbf{X}_\tau - A_{\theta_{X_\tau}}\mathbf{Q} \;=\mathbf{0}\;. \tag{4.6}$$

Here, θ_{X_τ} is the projection of the mapped points onto the invariant circle, which is described in detail in section 4.2.3, and $A_{\theta_{X_\tau}}$ is the Fourier coefficient matrix, which has the same structure as A_{θ_0}, but uses the projected angle elements instead of the original ones.

One advantage of this formulation is that a Newton iteration can be used, which has the potential to lead to quadratically convergent solutions. In Newton's iteration, an initial guess $\mathbf{Q^0}$ is iterated according to

$$\mathrm{DF}(\mathbf{Q^j})\;(\mathbf{Q^{j+1}} - \mathbf{Q^j}) \;=\; -F(\mathbf{Q^j}) \tag{4.7}$$

until a satisfactory answer is reached. Here, the superscript defines the value of $\mathbf{Q}$ at a given iteration step. To find an explicit form for this equation, all its variables are expanded in terms of $\mathbf{Q}$. F then becomes:

$$\begin{aligned} F\,(\mathbf{Q}) \;&=\; \mathbf{X}_\tau - \mathbf{X}_{\theta_{\phi(\tau,\mathbf{X_0})}} \\ &=\; \phi(\tau, A_{\theta_0}\;\mathbf{Q}) - A_{\theta_{\phi(\tau,A_{\theta_0}\,\mathbf{Q})}}\;\mathbf{Q}\;. \end{aligned} \tag{4.8}$$

I then take the derivative with respect to $\mathbf{Q}$:

$$\begin{aligned} \mathrm{DF}(\mathbf{Q}) \;&=\; \tfrac{dX_\tau}{dX_0}\,\tfrac{dX_0}{dQ} - \tfrac{dX}{d\theta_\phi}\,\tfrac{d\theta_\phi}{dX_\tau}\,\tfrac{dX_\tau}{dX_0}\,\tfrac{dX_0}{dQ} \\ &=\; \mathrm{DP\;A}_{\theta_0} - (\mathrm{DA}_{\theta_{\phi(\tau,\mathrm{A}_{\theta_0}\,\mathbf{Q})}}\;\mathbf{Q})\;\tfrac{\mathrm{d}\theta_\phi}{\mathrm{dX}_\tau}\;\mathrm{DP\;A}_{\theta_0}\,, \end{aligned} \tag{4.9}$$

where DP is the differential of the Poincaré map that is obtained from the first

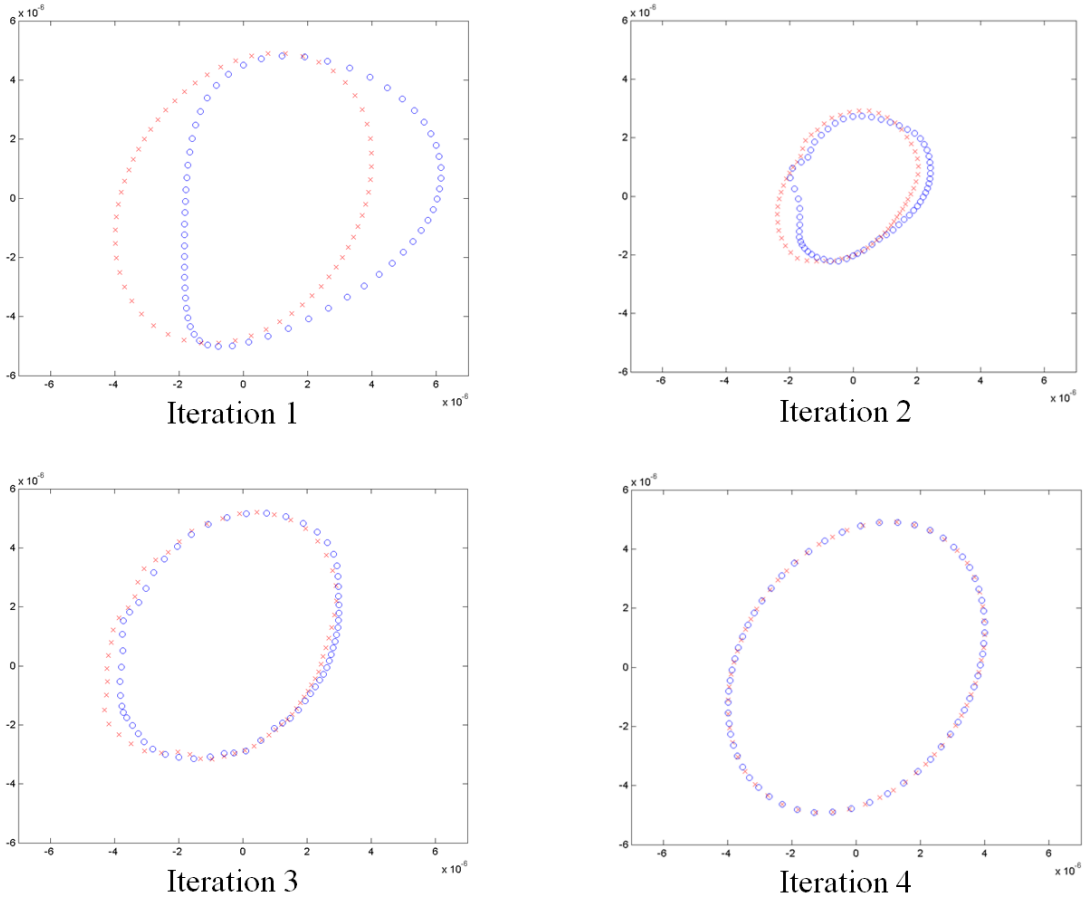

Figure 4.3: Iteration procedure in steps

variation of the map that was integrated with **X**. Employing Newton's iteration, solutions converge usually within 3-4 iterations. An example of an iteration procedure is shown in figure 4.3. Here, the sample points are shown as crosses and the return maps are represented by circles. After four iterations, all the sample points and the return maps are aligned on the same invariant circle.

4.1.2 Extension to Multiple Poincaré Sections

In order to overcome the potential instability that results from the long integration times, the invariant torus is cut by several Poincaré sections, as mentioned before. Figure 4.4 shows the invariant circles which are obtained when the tori of interest are cut with multiple sections. As a result, all the invariant circles in figure 4.4 are

determined, instead of only a single one, as was the case in the previous section.

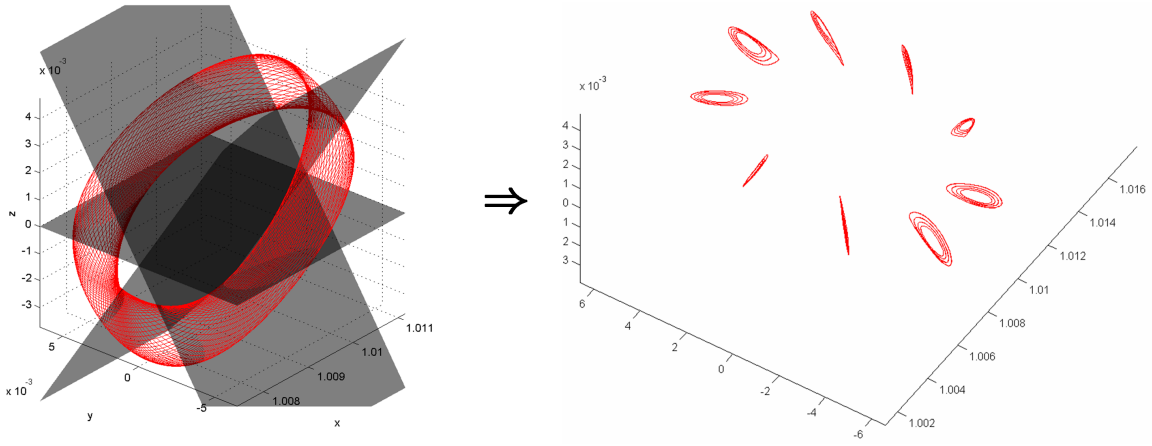

Figure 4.4: Multiple Poincaré Section Procedure: Invariant circles obtained by sectioning the invariant tori

The numerical procedure is similar to the single Poincaré section method. This time, the sample points are integrated until they hit the next Poincaré section, rather than being integrated for the whole period. For all these invariant circles to lie on the same invariant torus, all the mapped points must be aligned with the invariant circles of the next Poincaré section. The closure of the mathematical problem is obtained by requiring that the sample points from the last Poincaré section map to the first invariant circle. Mathematically, the invariance condition for the invariant circles can be expressed in the same form as in the single Poincaré section case by letting $\mathbf{Q}$, the vector containing the Fourier coefficients, be the concatenation of $\mathbf{q_i}$, the Fourier coefficients of each of the invariant circles,

$$\mathbf{Q} = [\,\mathbf{q_1};\ \mathbf{q_2};\ \ldots;\ \mathbf{q_{N_p-1}};\ \mathbf{q_{N_p}}\,], \tag{4.10}$$

where N_p is the number of Poincaré sections.

Thus, the invariance condition for all the invariant circles parameterized by $\mathbf{q_i}$ to

be on the same torus is

$$F(\mathbf{Q}) = F\begin{pmatrix} \mathbf{q}_1 \\ \mathbf{q}_2 \\ \vdots \\ \mathbf{q}_{N_p-1} \\ \mathbf{q}_{N_p} \end{pmatrix} = \begin{pmatrix} \phi(\tau, A_{\theta_0}\ \mathbf{q}_1) \\ \phi(\tau, A_{\theta_0}\ \mathbf{q}_2) \\ \vdots \\ \phi(\tau, A_{\theta_0}\ \mathbf{q}_{N_p-1}) \\ \phi(\tau, A_{\theta_0}\ \mathbf{q}_{N_p}) \end{pmatrix} - \begin{pmatrix} A_{\theta_{\phi(\tau, A_{\theta_0}\ \mathbf{q}_1)}}\ \mathbf{q}_2 \\ A_{\theta_{\phi(\tau, A_{\theta_0}\ \mathbf{q}_2)}}\ \mathbf{q}_3 \\ \vdots \\ A_{\theta_{\phi(\tau, A_{\theta_0}\ \mathbf{q}_{N_p-1})}}\ \mathbf{q}_{N_p} \\ A_{\theta_{\phi(\tau, A_{\theta_0}\ \mathbf{q}_{N_p})}}\ \mathbf{q}_1 \end{pmatrix} = 0 \quad (4.11)$$

Finally, as before, we apply Newton's iteration to the root finding problem:

$$\mathrm{DF}(\mathbf{Q}^{\mathrm{j}})\ (\mathbf{Q}^{\mathrm{j}+1} - \mathbf{Q}^{\mathrm{j}}) = -F(\mathbf{Q}^{j}). \quad (4.12)$$

4.1.3 Different Implementations

The quasi-periodic orbits reside in six-dimensional phase space, which has a four-dimensional center manifold (periodic subspace). Each quasi-periodic orbit is of dimension two. Thus, two properties of a given quasi-periodic orbit must be specified in order to uniquely define it. Many different parameters can be used to specify a quasi-periodic orbit; among these, the most intuitive and relevant for mission design are the Hamiltonian (or the Jacobi constant) of the orbit, the period of the orbit, and the size of the orbit. Since prescribing the period also prescribes the Hamiltonian and vice versa, two implementations where the period or the Hamiltonian is preset are considered in this section.

When the Hamiltonian is used to specify a quasi-periodic orbit, another constraint is needed in order to define the properties of the orbit of interest. I chose to specify the size of the orbit as the second variable. This is a relevant parameter since the distance between the telescope and the occulter is set by the size of the Quasi-Halo orbit. Since the numerical method is based on Poincaré sections, size can be specified by the two-dimensional area, $\mathbb{A}$, which is enclosed by the invariant circle. Then, the

constraint vector is augmented to include the new constraints:

$$F \;=\; [F \;;\; H_{fixed} \;-\; H_{\mathbf{Q}} \;;\; \mathbb{A}_{fixed} \;-\; \mathbb{A}_{\mathbf{Q}}]. \tag{4.13}$$

Another implementation is to set the period of the quasi-periodic orbit to a constant. Quasi-Halo orbits have two periods; one around the Halo orbit and the other along the Halo orbit. The period along the Halo orbit is very important for space missions that require all spacecraft to stay close to one another at all times. An uncontrolled mismatch in this period would lead to a separation on the order of the size of the Halo orbit, which is unacceptable. However, this period for a numerically computed two-dimensional structure is vague, unlike the one-dimensional case. I define this period of the Quasi-Halo to be the average time it takes for all the sample points starting from the initial Poincaré section to return back to it. That is, the period is

$$T = \frac{1}{n} \sum_{i=1}^{n} \tau(\mathbf{x_i}) \; . \tag{4.14}$$

Here, n is the total number of sample points taken on the Poincaré section. This way, the period of the quasi-periodic orbit can be specified along with the integration direction for the return map. In this case, there is one more degree of freedom to specify a unique orbit. Choosing the Hamiltonian as a constraint is not an option, as discussed before. Thus, I specify the size of the orbit by choosing the area parameter: the two-dimensional area, $\mathbb{A}$, which is enclosed by the invariant circle. This can be done by augmenting the error vector with a new constraint, such as the projected size along one direction:

$$F \;=\; [F \;;\; T_{fixed} \;-\; T_{\mathbf{Q}} \;;\; \mathbb{A}_{fixed} \;-\; \mathbb{A}_{\mathbf{Q}} \,]. \tag{4.15}$$

4.1.4 Continuation Procedure

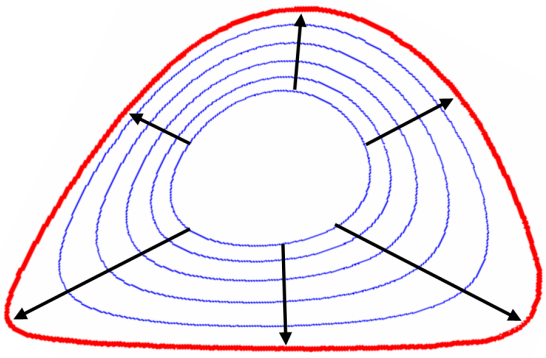

Figure 4.5: A schematic illustration of continuation in the area variable

Once the Fourier coefficients for a given orbit have been obtained, it is important to extend these results to find the complete quasi-periodic family. This procedure is called *continuation*, in which the previous solutions for quasi-periodic orbits in a given family are used to extrapolate another member of the family along a continuation parameter. Ultimately, the full quasi-periodic family is obtained.

In this study, I used the area variable, $\mathbb{A}$, as the continuation parameter. In figure 4.5, a schematic illustration of continuation in the area variable is shown. The inner orbits in the figure have a smaller area. The arrow indicates the direction of the continuation. Given a set of blue orbits that have already been found in a Quasi-Halo family, the aim of the continuation is to find the Quasi-Halo that is shown in red, in order to extend the results.

While there is no intuitive way to continue the coordinate variables, $\{x, y, z, \dot{x}, \dot{y}, \dot{z}\}$, the continuation of the Fourier coefficients is straight-forward, since they vary incrementally between sufficiently close quasi-periodic family members. A low-order polynomial fit is thus sufficient for continuing these parameters. Even a very simple linear continuation in the area variable, $\mathbb{A}$, gives satisfactory results:

$$\mathbf{Q^0_{k+1}} \quad = \quad \mathbf{Q}_k + \frac{\mathbb{A}_{k+1} - \mathbb{A}_k}{\mathbb{A}_k - \mathbb{A}_{k-1}}(\mathbf{Q}_k - \mathbf{Q}_{k-1}). \tag{4.16}$$

Here, as before, the superscript of $\mathbf{Q}$ defines the Newton's iteration step, while the subscript defines the continuation step.

Once the initial guess for ${\mathbf{Q^0}}_{k+1}$ is obtained, the multiple Poincaré section method is applied on this guess to get the correct $\mathbf{Q}_{k+1}$. Then, the continuation is repeated to find $\mathbf{Q}_{k+2}$.

4.2 Numerical Application for the Quasi-Periodic Orbits Around the L2 Region of the CRTBP

In this section, I show the numerical computation in implementation order. The details of the computations are discussed in the sections that follow.

1. Compute the initial guess $\mathbf{Q_0^0}$.

2. Compute X_0.

$$\mathbf{X_0} = A_{\theta_0}\ \mathbf{Q_k^j} \tag{4.17}$$

3. Compute Poincaré map for each Σ_i.

$$\mathbf{X}_\tau = P(\mathbf{X_0}) \tag{4.18}$$

4. Compute $\theta_{\mathbf{X}_\tau}$.

$$\begin{aligned} \theta_{\mathbf{X}_\tau} &= arctan(\tfrac{X_\tau(2)}{X_\tau(1)}) \quad \text{for Lissajous orbits} \\ \theta_{\mathbf{X}_\tau} &= arctan(\tfrac{X_\tau(6)}{X_\tau(5)}) \quad \text{for Quasi-Halo orbits} \end{aligned} \tag{4.19}$$

5. Compute the error.

$$F\left(\mathbf{Q_k^i}\right) \;=\; \mathbf{X}_\tau - A_{\theta_{\mathbf{X}_\tau}}\,\mathbf{Q_k^j} \tag{4.20}$$

6. Compute the Jacobian of the error.

$$\mathrm{DF}(\mathbf{Q_k^j}) \;=\; \mathrm{DP\ A}_{\theta_0} - (\mathrm{DA}_{\theta_{\mathbf{X}_\tau}}\,\mathbf{Q_k^j})\,\tfrac{\mathrm{d}\theta_\phi}{\mathrm{dX}_\tau}\,\mathrm{DP\ A}_{\theta_0} \tag{4.21}$$

7. Augment the error vector and the Jacobian.

$$\begin{aligned} F &= [F\,;\,\mathbb{A}_{fixed} - \mathbb{A}_{\mathbf{Q}}\,;\,\ldots]\,, \\ \mathrm{DF} &= [\mathrm{DF}\,;\,\mathrm{D}\mathbb{A}\,;\,\ldots] \end{aligned} \tag{4.22}$$

8. Perform Newton's iteration.

$$\mathrm{DF}(\mathbf{Q_k^j})\,(\mathbf{Q_k^{j+1}} - \mathbf{Q_k^j}) \;=\; -F(\mathbf{Q_k^j}) \tag{4.23}$$

9. Decision step:

$$\text{Decision:}\begin{cases} \mathbf{Q}_k = \mathbf{Q}_k^{j+1} \text{ and go to 10} & \text{if } |F(\mathbf{Q_k^j})| < \epsilon, \\ \text{Go to 2} & \text{if } j < j_{max} \text{ and } |F(\mathbf{Q_k^j})| > \epsilon \\ \text{Redo 10} & \text{otherwise.} \end{cases}$$

10. Continuation: Extrapolate an initial guess for $\mathbf{Q}_{k+1}^0$ from previous Fourier elements $\{\mathbf{Q}_0, \ldots, \mathbf{Q}_k\}$ and continuation variables $\{\mathbb{A}_0, \ldots, \mathbb{A}_k\}$

$$\mathbf{Q}_{k+1}^0 \;=\; polyfunc(\mathbb{A}_{k+1})\,. \tag{4.24}$$

Stop the numerical implementation if the full quasi-periodic family is obtained. Otherwise, go to 2.

4.2.1 Initial estimate for Q

Let us consider the monodromy matrix, M, which was discussed in the last chapter, as a linear map from the initial variations around the periodic orbit at time 0 to variation after one period T,

$$M := \delta x_0 \rightarrow \delta x_T \, . \tag{4.25}$$

Recall that the monodromy matrices for vertical Lyapunov and Halo orbits each have an eigenvalue couple, $cos\sigma \pm isin\sigma$ with modulus 1 and corresponding eigenvector $\mathbf{v_1} \pm i\mathbf{v_2}$. By the definition of eigenvalue and eigenvector,

$$\begin{aligned} M\,(\mathbf{v_1} + i\mathbf{v_2}) &= (cos\sigma + isin\sigma)\,(\mathbf{v_1} + i\mathbf{v_2}) \\ &= cos\sigma\ \mathbf{v_1} - isin\sigma\ \mathbf{v_2} + i(sin\sigma\ \mathbf{v_1} + cos\sigma\ \mathbf{v_2})\,, \qquad (4.26) \\ M\,(\mathbf{v_1} - i\mathbf{v_2}) &= (cos\sigma - isin\sigma)\,(\mathbf{v_1} - i\mathbf{v_2}) \\ &= cos\sigma\ \mathbf{v_1} - isin\sigma\ \mathbf{v_2} - i(sin\sigma\ \mathbf{v_1} + cos\sigma\ \mathbf{v_2})\,. \qquad (4.27) \end{aligned}$$

Using these properties, it is possible to find the invariant circle of the map M. Let us consider a closed curve, φ, of this map, parameterized with $\theta = [0,\ 2\pi]$,

$$\varphi(\theta) = \kappa(cos\theta\mathbf{v_1} - sin\theta\mathbf{v_2})\,. \tag{4.28}$$

Using trigonometric manipulation, it can now be shown that the monodromy matrix maps this closed curve onto itself:

$$\begin{aligned} \varphi(\theta) &\stackrel{M}{\rightarrow} M\ \kappa(cos\theta\ \mathbf{v_1} - sin\theta\ \mathbf{v_2}) \\ &= \kappa(cos(\theta+\rho)\ \mathbf{v_1} - sin(\theta+\rho)\ \mathbf{v_2}) \\ &= \varphi(\theta+\rho)\ . \end{aligned} \tag{4.29}$$

Thus, $\varphi(\theta)$ is a periodic orbit of this map (which should not be confused with the invariant circle of the Poincaré section) with κ magnitude. It is a linear approximation to the relative distance from the quasi-periodic orbit to the periodic orbit. In the numerical scheme, I used the linear approximation with small κ as the starting point for the multiple Poincaré scheme. κ values of order 10^{-6} have been sufficiently small to give reasonable startup approximations. (Please recall that, in the normalized units, 1 is the distance between Sun and Earth).

$\varphi(\theta)$ is a periodic orbit of the monodromy map. I first chose a high number, $N_M = 100$, of parametrization variables,

$$\theta_M(i) = \frac{2\pi i}{N_M} \quad i = 0, 1, \ldots, N_m - 2, N_m - 1\ , \tag{4.30}$$

and obtained the corresponding N_M points on the closed curve:

$$\mathbf{X_M} = \varphi(\theta_M)\,. \tag{4.31}$$

For the multiple Poincaré algorithm, an initial estimate is needed for the periodic orbit on the Poincaré map. To this aim, I integrated $\mathbf{X_M}$ and found their intersection with the Poincaré sections of interest. The methods I employed are the subject of the two chapter sections that follow.

The initial estimate for the Fourier elements, $\mathbf{Q_0^0}$, was obtained by using fast

Fourier transform (fft) on the intersecting points. It is important to note that this is the only time that a Fourier transform is employed in the algorithm. Once $\mathbf{Q_0^0}$ is obtained, all the transformations, including the continuation step, take $\mathbf{Q} \rightarrow \mathbf{X}$. For ease of programming, I chose to use real valued Fourier coefficients rather than imaginary ones. Below, a pseudo-code shows how to obtain the Fourier coefficients:

```
input: X
    N= length(X);
    y = fft(X);
    Q(1) = 1/sqrt(2)/N*real(y(1));
    for { i=2:i_max
        Q(2*(i-1))= 2/N*real(y(i));
        Q(2*(i-1)+1)= -2/N*imaginary(y(i));}
output: Q
```

where i_max was chosen to be 20. I would like to note that, due to sin(0)=0, the imaginary part of y(1) is always 0.

4.2.2 Choosing the Poincaré Section Surfaces

When choosing the planes of the section, the main concern is to ensure that the velocity vector of the quasi-periodic orbit is as transverse to the surface of section, Σ, as possible. This reduces the possibility of the integrated points not returning to the Poincaré section.

For the Lissajous orbits, I restrict the Poincaré sections to be on one side of the $z = 0$ plane because of the mirror symmetry of the CRTBP with respect to the z plane, which was discussed in the previous chapters. For the single Poincaré section method, I used a section on the $z = 0$ plane. When extending this to multiple Poincaré sections, an intuitive choice was to use sections parallel to this $z = 0$. Thus,

I chose four sections over the half period (equivalent to seven sections over the full period). Two of these are $z = 0$ and the other two are $z = z_{fixed}$, one section as the trajectories cross these sections in one direction and another while they cross in the other direction:

$$0 \;=\; g_i(\mathbf{x}) \;=\; z_{fixed_i} - z_{qh}(\tau_i)\,. \tag{4.32}$$

I chose z_{fixed} to be half of the maximum displacement in the z-direction to ensure that all the trajectories are transversal.

For Quasi-Halos, sections that are parallel to one another cannot be considered, since the torus twists in space. A good candidate for the Poincaré section surface, $g(\mathbf{x})$, is the plane perpendicular to the velocity of the halo orbit section:

$$0 \;=\; g_i(\mathbf{x}) \;=\; [x_h(t_i) - x_{qh}(\tau_i)]\dot{x}_h + [y_h(t_i) - y_{qh}(\tau_i)]\dot{y}_h + [z_h(t_i) - z_{qh}(\tau_i)]\dot{z}_h\,, \tag{4.33}$$

where subscript $_h$ stands for the Halo orbit and subscript $_{qh}$ stands for the Quasi-Halo orbit.

Along the Quasi-Halo, ten of these sections, $g_{i=0\ldots9}$, are taken with equal separation in time, i.e., $t_i = \frac{i}{9T}$, where $i = 0, \ldots, 9$. Figure 4.6 shows the multiple Poincaré sections on a sample Quasi-Halo orbit. Then, the Fourier coefficients that correspond to all the sections along the trajectory are continued, giving initial conditions to the next Quasi-Halo.

4.2.3 Choosing θ and computing its derivative $\frac{d\theta_{\mathbf{X}_\tau}}{dX_\tau}$

I choose the Poincaré sections to be along the coordinate variables of the state. Thus, an intuitive choice for θ would be to pick it as the angle between the coordinate variables of the invariant circles. Since all the sections, $g_i(\mathbf{x}) = z_{fixed_i} - z_{qh}(\tau_i)$, for the Lissajous case are parallel to one another, it is feasible to choose θ as the angle

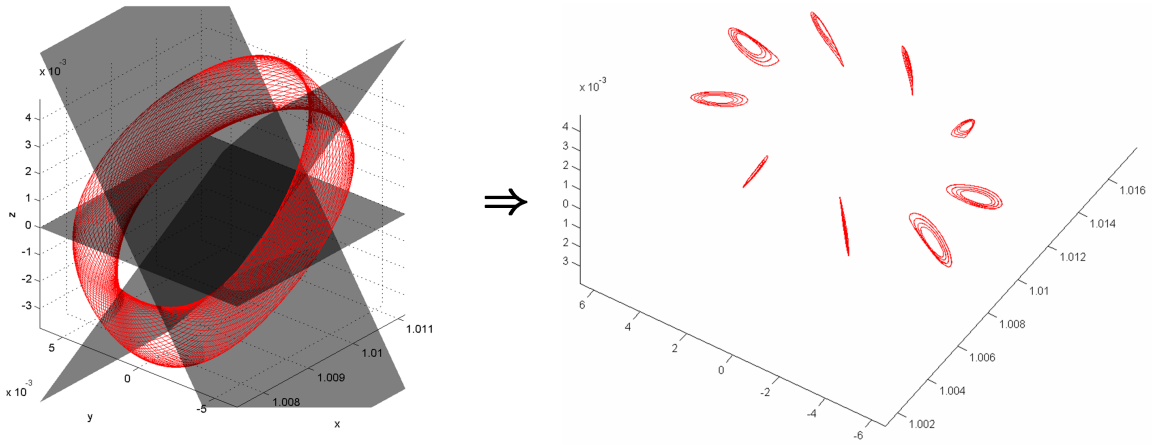

Figure 4.6: Multiple Poincaré section selection on the Quasi-Halo orbit

between the coordinate variables $\theta = arctan(y/x)$. A single form of parametrization, $\theta = arctan(y/x)$, defines the cross sections on all the Poincaré sections uniquely, and this is therefore the parametrization that I use.

A major advantage of such a parametrization is the reduction in size of $\mathbf{Q}$. Since z is constant on the Poincaré section, the Fourier coefficient is not needed for this vector. In addition, an explicit interdependence of x and y makes it feasible to use one Fourier element vector to define both these states. Thus, instead of using six sets of Fourier element vectors to define six states, it can be reduced to four sets. The reduced Fourier series vector is

$$\mathbf{Q} = \left[\mathbf{Q_R}\,;\quad \mathbf{Q_{\dot{x}}}\,;\quad \mathbf{Q_{\dot{y}}}\,;\quad \mathbf{Q_{\dot{z}}}\right]\,, \tag{4.34}$$

where $R = \sqrt{x^2 + y^2}$ and $\mathbf{Q_R}$, $\mathbf{Q_{\dot{x}}}$, $\mathbf{Q_{\dot{y}}}$, $\mathbf{Q_{\dot{z}}}$ are the Fourier series coefficients of the R, $\dot{x}$, $\dot{y}$, $\dot{z}$, variables of the invariant circle, respectively.

Unlike in the Lissajous case, the Poincaré sections given in equation 4.33 are not parallel in the case of the quasi-halo orbits. The choice of θ as the angle along the coordinate variables leads to different parameterizations for each of the sections. In

order to reduce the extra complication that this would entail, I opted for a simpler parametrization that works for all the sections at the same time, as in the Lissajous case. Figure 4.7 shows the projection of the invariant circle on different axes of all the closed orbits on the Poincaré sections. Looking at this figure, it is apparent that parametrization $\theta = arctan(\dot{z}/\dot{y})$ works for all the sections. As with the Lissajous case, a major advantage of such a parametrization is the reduction in size of $\mathbf{Q}$. The reduced Fourier series vector for a quasi-halo is thus

$$\mathbf{Q} = \left[\mathbf{Q_x}\,;\quad \mathbf{Q_y}\,;\quad \mathbf{Q_z}\,;\quad \mathbf{Q_{\dot{x}}}\,;\quad \mathbf{Q_R}\right], \tag{4.35}$$

where $R = \sqrt{\dot{y}^2 + \dot{z}^2}$ and $\mathbf{Q_x}$, $\mathbf{Q_y}$, $\mathbf{Q_z}$, $\mathbf{Q_{\dot{x}}}$, $\mathbf{Q_R}$ are the Fourier series coefficients of the x, y, z, $\dot{x}$, R variables of the invariant circle, respectively.

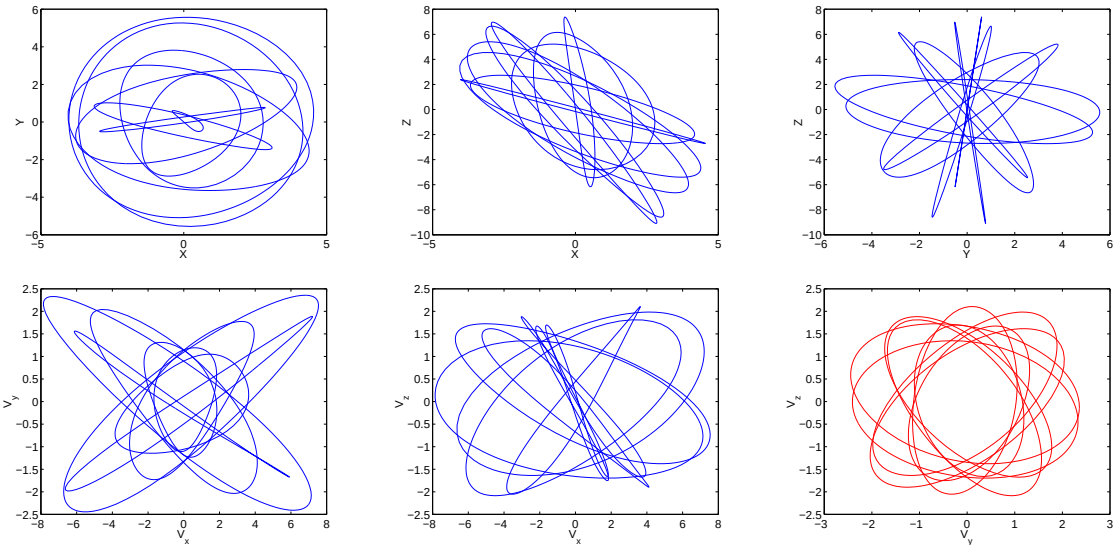

Figure 4.7: The relative distance from the invariant circle is projected on different axes for a sample orbit. The upper three sub-plots show the projection on the position space, while the lower ones show the projection on the velocity space. The sub-plot on the lower right corner, which is the V_y (i.e. $\dot{y}$) versus V_z (i.e. $\dot{z}$), is highlighted in red.

Finally, employing the chain rule, the derivative of θ with respect to $\mathbf{X}_\tau$ can be obtained as

$$\begin{aligned}
\frac{d\theta_{\mathbf{X}_\tau}}{dX_\tau} &= [-\frac{y}{x^2+y^2}, \frac{x}{x^2+y^2} 0,\ 0,\ 0,\ 0,\ ] \quad \text{for Lissajous} \\
\frac{d\theta_{\mathbf{X}_\tau}}{dX_\tau} &= [\,0,\ 0,\ 0,\ 0,\ -\frac{\dot{z}}{\dot{y}^2+\dot{z}^2}, \frac{\dot{y}}{\dot{y}^2+\dot{z}^2}\,] \quad \text{for Quasi-Halo}\,.
\end{aligned}$$

4.2.4 Computing A_θ and DA

Recall that the invariant circle, γ, on the Poincaré section was defined via a finite Fourier series:

$$\gamma(\theta) = \frac{a_0}{\sqrt{2}} + \sum_{n=1}^{n_{max}} [a_n \cos(n\theta) + b_n \sin(n\theta)]\ , \tag{4.36}$$

with θ on the interval $[0, 2\pi)$. and A_θ as the transformation from the Fourier elements to the state vector.

In this section, I explain how to obtain this matrix and its derivative. The Fourier coefficients vector, $\mathbf{Q}$, for Lissajous and Quasi-Halo orbits was defined in equations 4.34 and 4.35. The state vector, $\mathbf{X}$, can then be obtained by multiplying $\mathbf{Q}$ with the following A_θ:

$$A_\theta = \begin{bmatrix}
A_{section_1} & 0 & \cdots & 0 & 0 \\
0 & A_{section_2} & \cdots & 0 & 0 \\
\vdots & \vdots & \ddots & 0 & 0 \\
0 & 0 & 0 & A_{section_{N_{sec}-1}} & 0 \\
0 & 0 & 0 & 0 & A_{section_{N_{sec}}}
\end{bmatrix}. \tag{4.37}$$

In the above equation, the maximum number of sections, N_{sec}, is four for Lissajous

orbits and ten for Quasi-Halo orbits, and

$$A_{section_i} = \begin{bmatrix} A_1 \\ A_2 \\ \vdots \\ A_{N_{npoints}-1} \\ A_{N_{npoints}} \end{bmatrix}, \tag{4.38}$$

where $N_{npoints} = 40$ is the number of points on each Poincaré section. A_i for Lissajous orbits is given by

$$A_i = \begin{bmatrix} cos(\theta_i)cs(\theta_i) & 0 & 0 & 0 \\ sin(\theta_i)cs(\theta_i) & 0 & 0 & 0 \\ 0 & 0 & 0 & 0 \\ 0 & cs(\theta_i) & 0 & 0 \\ 0 & 0 & cs(\theta_i) & 0 \\ 0 & 0 & 0 & cs(\theta_i) \end{bmatrix}. \tag{4.39}$$

Note that the constant value of z_{fixed} has to be added to A_θ $\mathbf{Q}$ later on. For the Quasi-Halo orbits, A_i is given by

$$A_i = \begin{bmatrix} cs(\theta_i) & 0 & 0 & 0 & 0 \\ 0 & cs(\theta_i) & 0 & 0 & 0 \\ 0 & 0 & cs(\theta_i) & 0 & 0 \\ 0 & 0 & 0 & cs(\theta_i) & 0 \\ 0 & 0 & 0 & 0 & cos(\theta_i)cs(\theta_i) \\ 0 & 0 & 0 & 0 & sin(\theta_i)cs(\theta_i) \end{bmatrix}, \tag{4.40}$$

where $cs(\theta_i)$ is the vector

$$cs(\theta_i) = \left\{ \frac{1}{2} \quad cos(\theta_i) \quad sin(\theta_i) \quad cos(2\theta_i) \quad sin(2\theta_i) \quad \cdots \quad cos(N_0\theta_i) \quad sin(N_0\theta_i) \right\} \tag{4.41}$$

In the equation above, $N_0 = 20$ is the maximum number of Fourier elements to be used in the system. $\mathrm{DA} = \frac{\mathrm{dA}_\theta}{\mathrm{d}\theta}$ can be obtained in a similar fashion. To save space, I do not include the explicit form of DA. It can be obtained via term-by-term differentiation of A_θ.

4.2.5 Augmenting the error vector F and its derivative DF

One of the main advantages of this algorithm is the ease with which constraints can be added. For example, in order to fix the value of the Hamiltonian (i.e. the Jacobi constant), equation 4.13 is used to augment the error vector, where H_{fixed} is set to the Hamiltonian of the base Halo or the vertical Lyapunov orbit. The equation to obtain the Hamiltonian is listed in 2.14.

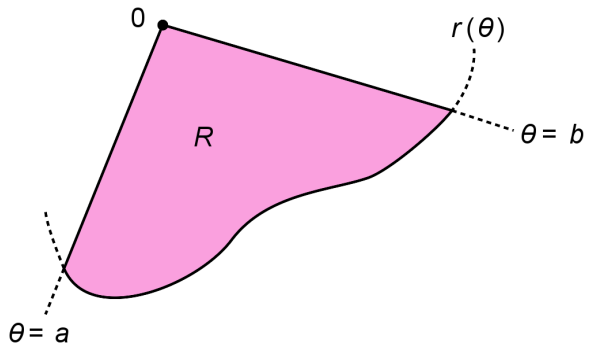

Figure 4.8: Polar coordinates integration region [51].

As for the determination of the area variable, $\mathbb{A}$, use of the Fourier coefficients is of great help. If R denotes the region enclosed by a curve $r(\theta)$, as shown in figure

4.8, and the rays $\theta = a$ and $\theta = b$, where $0 < b - a \leqslant 2\pi$, the area of R is

$$\mathbb{A} = \frac{1}{2}\int_a^b r(\theta)^2\, d\theta. \tag{4.42}$$

Substituting the Fourier expansion in equation 4.36 for $r(\theta)$, and noting that $a = 0$ and $b = 2\pi$ and $r(0) = r(2\pi)$, the well-known Parseval Theorem [52] states that the area integral becomes

$$\mathbb{A} = \frac{\pi}{2} < \mathbf{Q_R}, \mathbf{Q_R} > , \tag{4.43}$$

where $< \ ., \ . >$ is the usual dot product.

For the fixed period case, the augmentation given in equation 4.15 is used to obtain the error vector, where T_{fixed} is set to the period of the base Halo or the vertical Lyapunov orbit. The period of quasi-periodic orbit, T, is obtained from equation 4.14.

As for the derivative terms, the derivative of the Hamiltonian is

$$\mathrm{DH} \ = \ \mathrm{DHdx}\ \mathrm{DP}\ \mathrm{A}_{\theta_0}\,, \tag{4.44}$$

where

$$\mathrm{DHdx} \ = \ \begin{bmatrix} 2x + \frac{-2\mu(-1+\mu+x)}{(-1+\mu+x)^2+y^2+z^2)^{3/2}} - \frac{2(1-\mu)(\mu+x)}{(\mu+x)^2+y^2+z^2)^{3/2}} \\ 2y + \frac{-2\mu y}{(-1+\mu+x)^2+y^2+z^2)^{-3/2}} - \frac{2(1-\mu)y}{(\mu+x)^2+y^2+z^2)^{-3/2}} \\ \frac{-2\mu z}{(-1+\mu+x)^2+y^2+z^2)^{-3/2}} - \frac{(1-\mu)z}{((\mu+x)^2+y^2+z^2)^{-3/2}} \\ -2\dot{x} \\ -2\dot{y} \\ -2\dot{z} \end{bmatrix}. \tag{4.45}$$

The Jacobian of $\mathbb{A}$ is simply

$$\mathrm{D}\mathbb{A} = \pi \mathbf{Q_R} \,. \tag{4.46}$$

Finally, the Jacobian of T is

$$\mathrm{DT} \;\; = \;\; \frac{1}{npoints} \mathrm{D}\tau(\mathbf{X_0}) \; \mathrm{A}_{\theta_0} \,, \tag{4.47}$$

where $\mathrm{D}\tau(\mathbf{X_0})$ is given in equation 4.51.

4.2.6 Numerical Integration of the Orbits

The CRTBP has a nonstiff and smooth ordinary differential equation. For nonstiff problems, an explicit numerical integration technique achieves the desired accuracy with minimal computational costs. Additionally, for smooth ODEs, higher-order integration methods can be employed which further reduces the computation time. Thus, to numerically propagate the initial state variables, I used an explicit 8-7 Runge-Kutta method. The method integrates a system of ordinary differential equations using 8-7th order Dorman and Prince formulas [53].

This is an 8th-order accurate integrator; therefore, the local error normally expected is $\mathbb{O}(h^9)$. In this scheme, the approximation for the state at $x_1(h + t_0)$ is obtained from the state at $x_0(t_0)$ with the equation

$$x_1 = x_0 + h \sum_{i=1}^{s} b_i F_i \,, \tag{4.48}$$

where F_i is obtained from

$$F_i = f(t_0 + h\, c_i, x_0 + h \sum_{j=1}^{s} a_{ij} F_j) \,, \tag{4.49}$$

and where the constants, the lower triangular a_{ij} matrix and the b_i and c_i vectors, are listed in [53]. The number of stages, s, is 13. Thus, the procedure requires 13 function evaluations per integration step. The error check is done by finding both the 7th and 8th order solutions and looking at the difference between them. If the difference is above a preset error bound ϵ, which I chose to be 10^{-13} for high accuracy, the step size is reduced and the solution recomputed.

4.2.7 Numerical computation of the Poincaré map

Remember that the Poincaré map is defined by

$$\mathbf{X}_\tau \;=\; \mathbf{P}(\mathbf{X_0}) \;=\; \phi(\tau(\mathbf{X_0}), \mathbf{X_0})\,. \tag{4.50}$$

The Poincaré section, Σ, given by $\{g(\mathbf{x}) = 0\}$, separates the phase space in two. Assuming that Σ is to be crossed in the direction from the initial state's, $\mathbf{X}_0$, side of the phase space to the other side, the following pseudo-code is used to numerically obtain the Poincaré map:

```
input: X0, f, h, tol, g, Dg
    t=0; y=X0;
    while [g(y)*g(X0)] > 0 {
        rk87(f) := (t,y) -> (t+h,y+deltay)
        t = t+h; y = y+deltay }
    while |g(y)| > tol {
        delta = - g(y)/(Dg(y)f(y))
        rk87(f) := (t,y) -> (t+delta,y+deltay) }
output: t, y.
```

where rk87 is the 8-7th order Runge-Kutta integration step.

Each iteration of the last loop corresponds to performing a Newton iteration to find a zero of the function $F := g(\phi(\text{delta}, y)) = 0$ with initial condition delta $= 0$. In this case, DF $= \frac{\text{dg}}{\text{d}\phi(\text{delta,y})} \frac{\text{d}\phi(\text{delta,y})}{\text{ddelta}}$. Remembering the Euler approximation to integration, $\phi(\text{delta}, y) \approx y + f(y)\,\text{delta}$, I obtain DF $=$ Dg(y) f(y). It is possible to see that the pseudo-code employs root finding via the Newton iteration, delta $= -F\,\text{DF}^{-1}$. At the end of the algorithm, $P(\mathbf{X_0}) = y$ and $\tau(\mathbf{X_0}) = t$.

4.2.8 Numerical Computation of the Derivative of the Poincaré map

The differential of the Poincaré map is computed as

$$\begin{aligned} \text{DP(x)} = \frac{\text{d}}{\text{dx}}\phi(\tau(\mathbf{x}), \mathbf{x})) &= \frac{d}{d\tau}\phi(\tau(\mathbf{x}), \mathbf{x}) + \text{D}\phi(\tau(\mathbf{x}), \mathbf{x}) \\ &= \mathbf{f}(P(\mathbf{x}))\text{D}\tau(\mathbf{x}) + \text{D}\phi(\tau(\mathbf{x}), \mathbf{x}) \,, \end{aligned} \tag{4.51}$$

where the differential of the time to reach Σ is obtained by differentiating the Poincaré section condition,

$$\begin{aligned} 0 &= g(P(\mathbf{x})) \\ \Rightarrow &= \text{Dg(P(}\mathbf{x}\text{))DP(}\mathbf{x}\text{)} \\ &= \text{Dg(P(}\mathbf{x}\text{))}\left[\mathbf{f}(\text{P}(\mathbf{x}))\text{D}\tau(\mathbf{x}) + \text{D}\phi(\tau(\mathbf{x}), \mathbf{x})\right] \\ &= \left[\text{Dg(P(}\mathbf{x}\text{))}\mathbf{f}(\text{P}(\mathbf{x}))\right]\text{D}\tau(\mathbf{x}) + \text{Dg(P(}\mathbf{x}\text{))D}\phi(\tau(\mathbf{x}), \mathbf{x}) \\ \Rightarrow \quad \text{D}\tau(\mathbf{x}) &= -\frac{\text{Dg(P(}\mathbf{x}\text{))}\phi(\tau(\mathbf{x}), \mathbf{x}))}{\text{Dg(P(}\mathbf{x}\text{))}\mathbf{f}(\text{P}(\mathbf{x}))} \end{aligned} \tag{4.52}$$

Substituting equation 4.52 in equation 4.51, I obtain the final form of DP:

$$\text{DP(x)} = -\mathbf{f}(\text{P}(\mathbf{x}))\frac{\text{Dg(P(}\mathbf{x}\text{))}\phi(\tau(\mathbf{x}), \mathbf{x}))}{\text{Dg(P(}\mathbf{x}\text{))}\mathbf{f}(\text{P}(\mathbf{x}))} + \text{D}\phi(\tau(\mathbf{x}), \mathbf{x})) \,. \tag{4.53}$$

Recall that in this study two types of Poincaré sections are used. For the Quasi-Halo Poincaré section defined in 4.33, Dg is

$$\mathrm{Dg} = \{\ \dot{x}\ \ \dot{y}\ \ \dot{z}\ \ 0\ \ 0\ \ 0\ \} , \tag{4.54}$$

and for the Lissajous Poincaré section defined in 4.32, Dg is

$$\mathrm{Dg} = \{\ 0\ \ 0\ \ 1\ \ 0\ \ 0\ \ 0\ \} . \tag{4.55}$$

4.2.9 Continuation

For the Quasi-Halo continuation with both the constant Hamiltonian and the constant period cases, I used the area, $\mathbb{A}$, of the projection of the invariant circle on the Poincaré section to the $\dot{y} - \dot{z}$ plane as the continuation parameter in accordance with the choice of θ as $arctan(\dot{z}/\dot{y})$. For the Lissajous orbit continuation with the constant Hamiltonian case, I used the area, $\mathbb{A}$, of the projection of the invariant circle on the Poincaré section to the $x - y$ plane as the continuation parameter in accordance with the choice of θ as $arctan(y/x)$.

For the first continuation, I used a linear extrapolation from the $\mathbf{Q}_0$ value to find $\mathbf{Q}_1$. For the second and third continuations, I used a second- and third-order polynomial fit to extrapolate the value of $\mathbf{Q}$. From the fourth onwards, I used a fourth-order polynomial fit to extrapolate the value of $\mathbf{Q}$ from the known values. Higher-order polynomial fits were avoided due to the well-known Runge's phenomenon, which leads to wildly oscillating interpolant function [54]. First, I obtain the polynomial fit:

$$polyfunc(\mathbb{A}) \quad = \quad polyfit([\mathbf{Q}_k, \mathbf{Q}_{k-1}, ..., \mathbf{Q}_0, \mathbf{0}], [\mathbb{A}_k, \mathbb{A}_{k-1}, ..., \mathbb{A}_0, 0], order) \tag{4.56}$$

where $polyfit$ is the usual least square polynomial fit of degree $order$. Then, the

continuation of the Fourier coefficient is performed by extrapolation:

$$\mathbf{Q}_{k+1} \quad = \quad polyfunc(\mathbb{A}_{k+1})\,, \tag{4.57}$$

where

$$\mathbb{A}_{k+1} = \mathbb{A}_k + \Delta\mathbb{A}\,. \tag{4.58}$$

While choosing $\Delta\mathbb{A}$, there is a compromise between speed and convergence. The larger the $\Delta\mathbb{A}$, the shorter the continuation procedure takes, while the possibility of non-convergence increases with increasing step size. To find the optimal iteration step size automatically, I set

$$\Delta\mathbb{A} = \begin{cases} 1.2\,\Delta\mathbb{A} & \text{if Newton iteration converged for all previous cases} \\ 0.8\,\Delta\mathbb{A} & \text{if Newton iteration did not converge: repeat the previous step} \\ \Delta\mathbb{A} & \text{otherwise}\,. \end{cases}$$

Thus, when the iteration is convergent, increasingly large steps are taken to speed up the process, until the maximum step size is exceeded and the algorithm becomes divergent. Then, the step size is reduced and the iteration is continued with the optimal step size.

Finally, I would like to note that as $\mathbb{A} \to 0$, so does $\mathbf{Q} \to \mathbf{0}$. Therefore, when $\mathbb{A} = 0$, $\mathbf{Q} = \mathbf{0}$. I use this property in the initial step of the continuation by setting the initial $\Delta\mathbb{A} = \mathbb{A}_0$.

For illustration purposes, figure 4.9 is a continuation curve for the constant Hamiltonian Quasi-Halo family which shows how the first four elements of the $\mathbf{Q}$ vector vary with the continuation parameter.

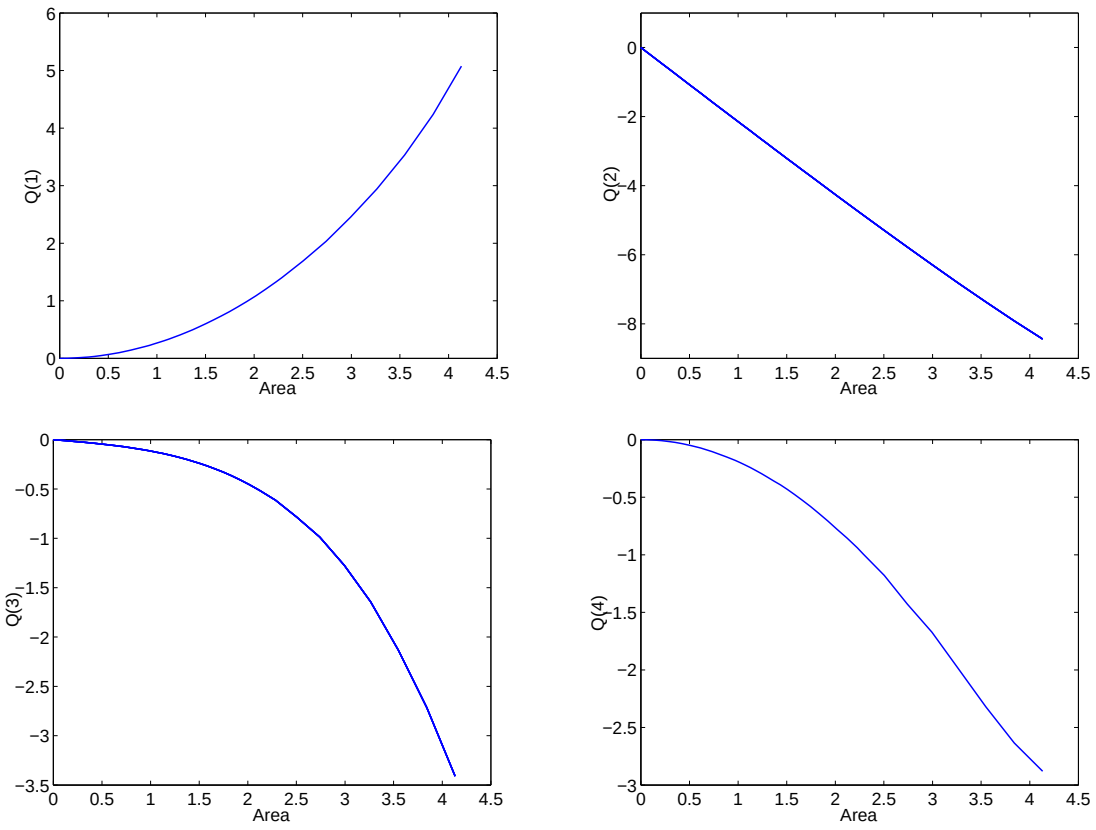

Figure 4.9: The first four elements of **Q** for the constant Hamiltonian Quasi-Halo family versus the continuation variable Area, $\mathbb{A}$.

4.3 Results

The four-dimensional center manifold around L2 is occupied by quasi-periodic orbits of two different families: the Lissajous family around the vertical Lyapunov orbits, and the Quasi-Halo orbits around the Halo orbits. These quasi-periodic orbits reside on invariant tori about the corresponding periodic orbit.

In this section, I apply the Multiple Poincaré numerical method to find these orbits. Once the Fourier coefficients on the Poincaré sections are obtained as described in the previous section, the two-dimensional quasi-periodic orbit is obtained by integrating a sample point on one of the Poincaré sections until it crosses the

same section again. Due to error bounds on the multiple Poincaré algorithm, this intersection point is very close to, but not exactly on, the one-dimensional invariant circle. This point is projected onto the invariant circle by finding $\theta_{proj} = arctan(y/x)$ or $\theta_{proj} = arctan(\dot{z}/\dot{y})$, depending on whether the point is on a Quasi-Halo or on a Lissajous orbit. Then the projected point $X_{proj} = A_{\theta_{proj}}\mathbf{Q}$ is integrated, as with the initial sample point, until it crosses the Poincaré section, and the procedure is repeated for the desired period length. Finally, these solutions are patched together to obtain the full orbit.

4.3.1 Lissajous Orbits

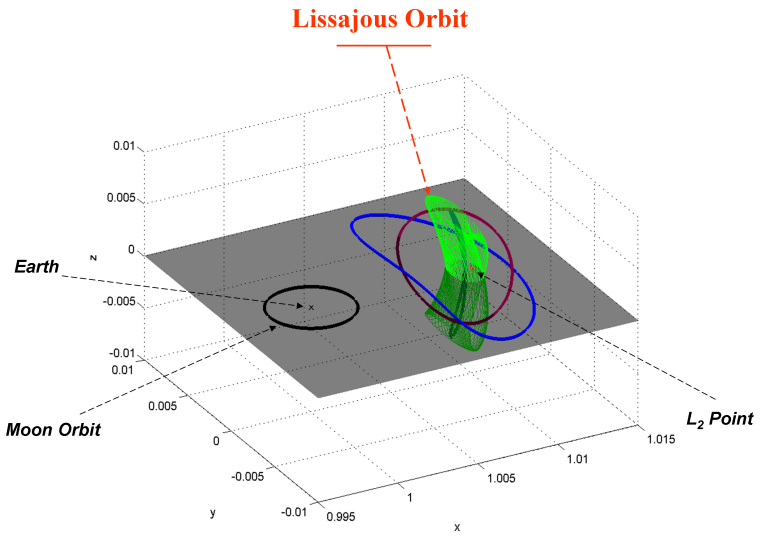

Figure 4.10: Lissajous orbits around the L2 libration point

The Lissajous family resides on invariant tori about the vertical Lyapunov orbits. These orbits, which were studied analytically in Chapter 2, can be obtained numerically by employing the multiple Poincaré section method. The full Lissajous family was obtained via this method, as shown in figure 4.14. Figure 4.10 and 4.11 shows typical Lissajous orbits around the L2 point.

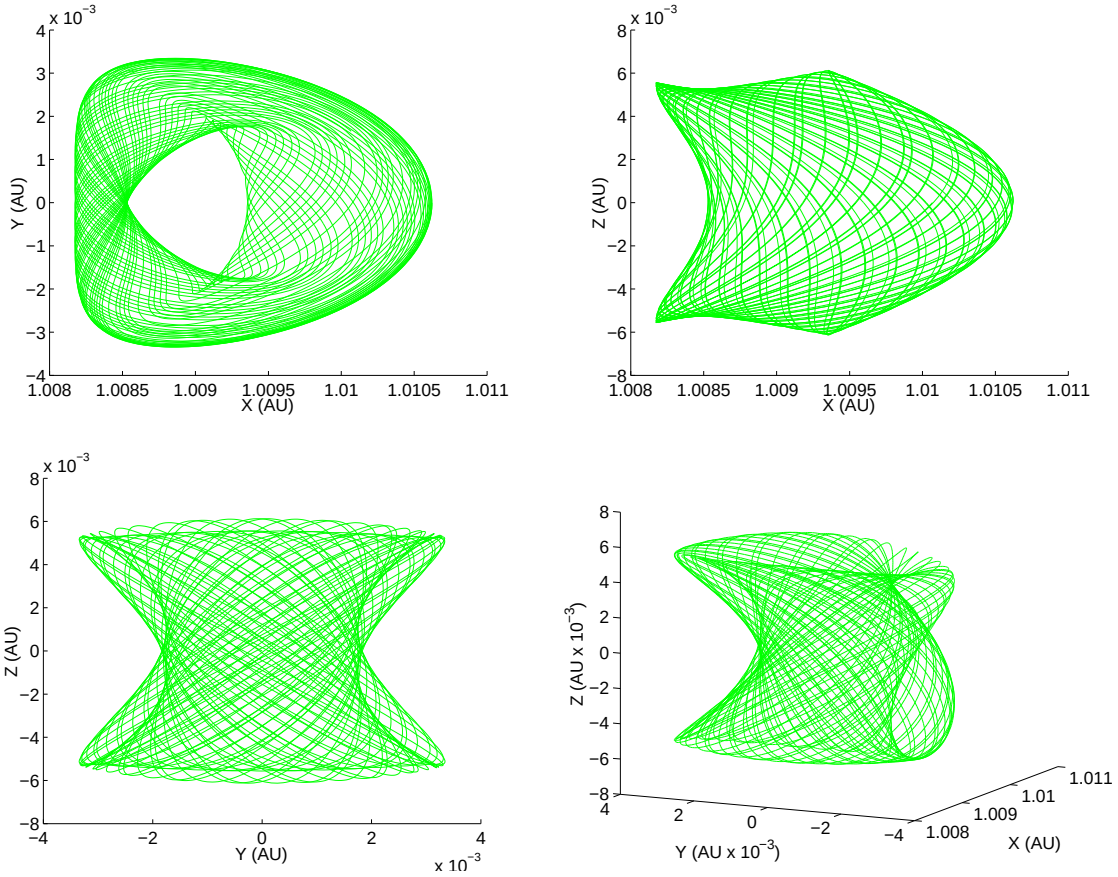

Figure 4.11: Example of a Lissajous Orbit around L2

4.3.2 Quasi-Halo Orbits

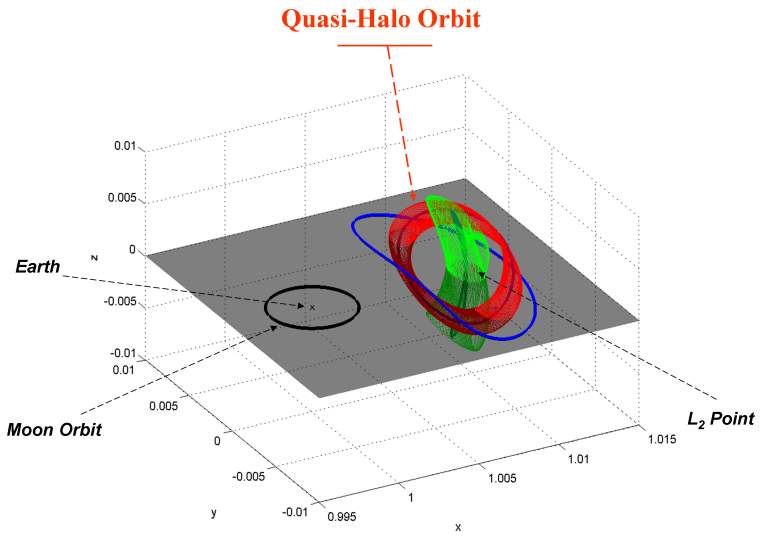

Figure 4.12: Quasi-Halo orbits around the L2 libration point

The quasi-halo family reside on invariant tori about the halo orbits. These orbits which were studied analytically in chapter 2 can be obtained numerically by employing the multiple Poincaré section method. The full Quasi-Halo family was obtained via this method, as shown in figure 4.14. Figure 4.12 and 4.13 shows typical Quasi-Halo orbits around the L2 point.

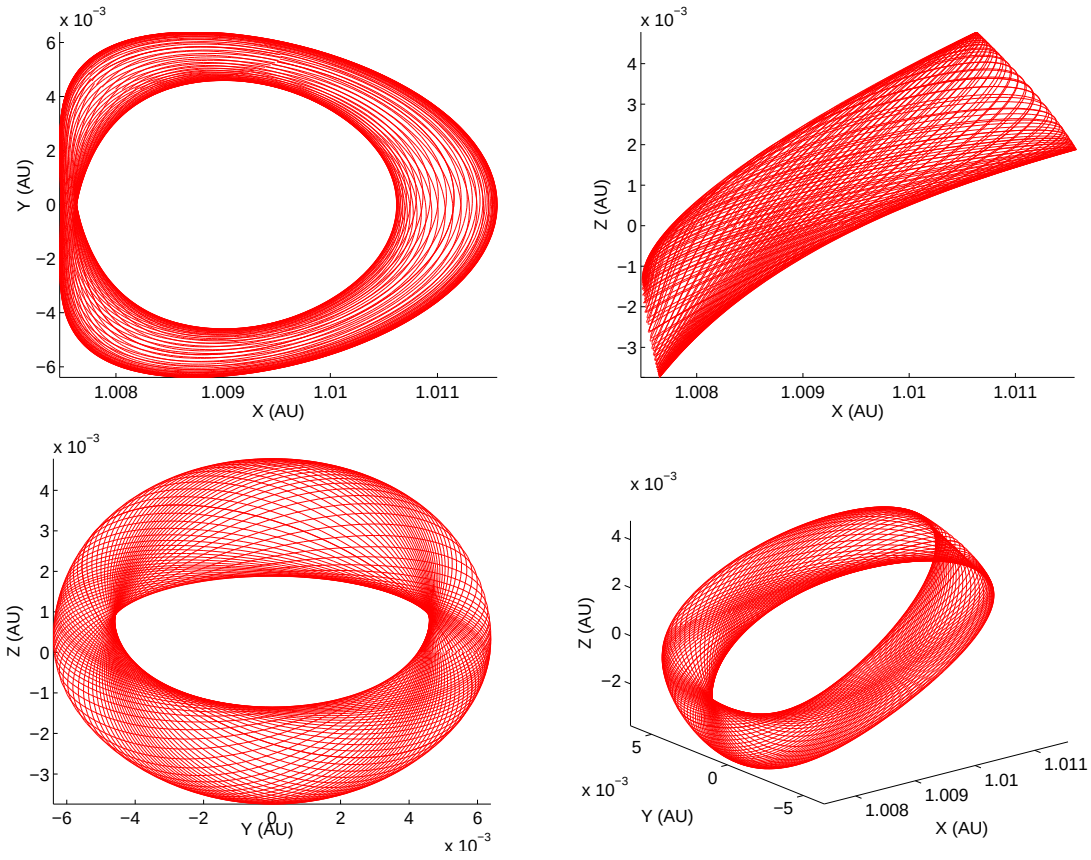

Figure 4.13: Example Quasi-Halo Orbit around L2

4.3.3 Complete Periodic Family around L2

To visualize the four-dimensional center manifold, which consists of all the periodic and quasi-periodic orbits, on a two-dimensional figure, the center manifold must be constrained by two dimensions. A convenient way of achieving this is to choose periodic and quasi-periodic orbits which have the same energy, and to take a Poincaré section when these orbits cross the ecliptic plane. Thus, figure 4.14 is obtained. In this figure, since this is a Poincaré section, the equilibrium points correspond to the periodic orbits of the original system, while the closed curves correspond to the quasi-periodic orbits. This correspondence of the real orbits and the sections on the Poincaré map is shown in figure 4.14.

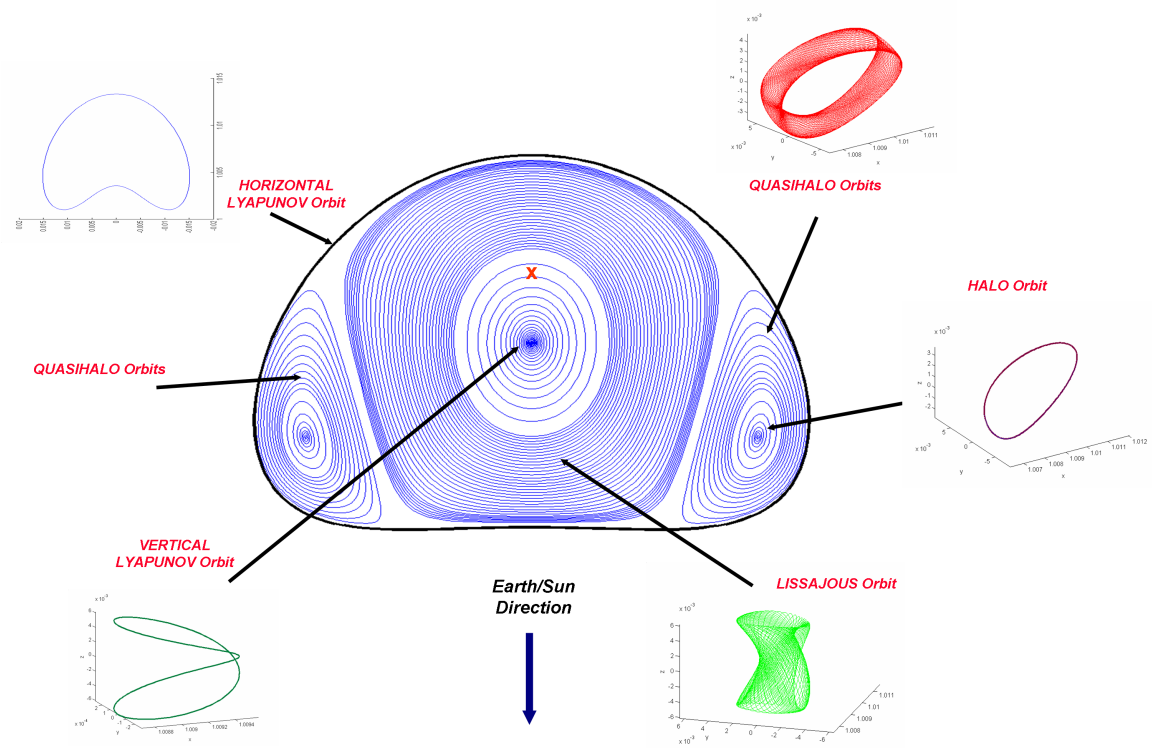

Figure 4.14: All the periodic and quasi-periodic orbits around L2 shown on a Poincaré section of the ecliptic plane

4.3.4 Comparison of the Results with the Literature

The Poincaré section in time, where I specified the orbit period along the Halo, is shown in figure 4.15. Here, the results are compared to Gómez et al.'s [46]. By specifying the period of all the orbits to be the same as that of the base Halo orbit, it is possible to ensure that the spacecraft stay close at all times. This is of great importance particularly for natural, control-free, formation-flying missions. The main advantage of the Poincaré section approach is that, due to the numerical nature of the algorithm, the calculations take only a few minutes of computation time, with minimal programming requirement. Note that, since the Hamiltonians for these orbits

are not equal to one another, the orbits may intersect.

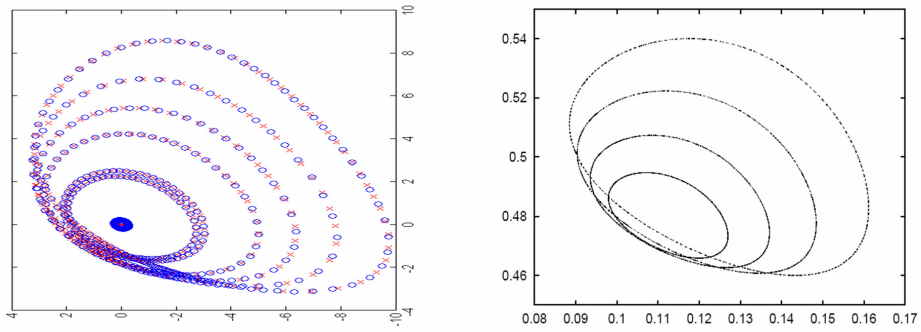

Figure 4.15: The Poincaré section of the invariant tori, where the period of all the orbits is equal to that of the base Halo orbit. The multiple Poincaré section method is employed on the left, while the Lindstedt-Poincaré method is used on the right [46].

Utilizing the multiple sections approach, the complete quasi-periodic orbit families around the libration points are found. Figure 4.16 shows the Poincaré section of the quasi-periodic family with constant energy on the ecliptic plane, and it compares the results obtained by our multiple Poincaré method with Gómez and Mondelo's refined Fourier analysis [55, 56] and Gómez et al.'s Lindstedt-Poincaré analysis [46]. While the Lindstedt-Poincaré analysis [46] cannot obtain the complete families and a cluster of parallel computers was required to get the complete families with the refined Fourier analysis [55, 56], the current method obtains the complete set of quasi-periodic orbits with a computation time for the full families of only a few minutes on a 2.15 GHz Intel Pentium processor.

4.4 Extension of the CRTBP Results to the Full Ephemeris Model

The quasi-periodic orbits obtained above reside on two-dimensional surfaces around the libration points of the CRTBP. These orbits do not exist in the real Solar system due to the eccentricity of the Earth's orbit and the perturbing effects of many celestial

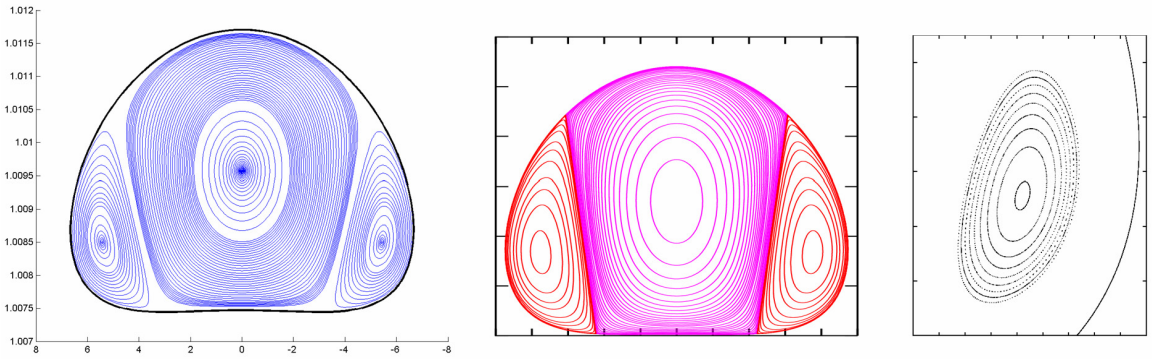

Figure 4.16: The Poincaré section of the complete quasi-periodic family around L2 with energy that is equivalent to the 500,000 km-sized halo orbit on the ecliptic plane (on the left). Similar results from Gómez & Mondelo [55, 56] (in the middle) and Gómez et al. [46] (on the right).

bodies. Nevertheless, since the CRTBP is a good first-order approximation to the real Solar System dynamics, there are orbits in the Solar System that have very similar shapes and properties to the orbits found in the simplified problem. The aim of this chapter is to find these orbits.

I take the real Solar System dynamics to be the point-mass gravitational interactions of the major Solar system bodies given at each time-instant with the JPL DE-406, which is the latest version of the JPL Solar System Ephemeris [57]. It specifies the past and future positions of the Sun, Moon, and nine planets (Pluto is still defined as a planet in this ephemeris) in three-dimensional space. The ephemeris gives the Chebyshev polynomial coefficients corresponding to the J2000 standard epoch positions of these Solar bodies [57, 58]. In the calculations to follow, deviation from the spherical symmetry of the bodies such as oblateness is not taken into account. Since the specifications of the spacecraft that will be placed in these orbits are not known, neither are drag and solar pressure included in the study. However, note that for a spherical spacecraft, the effect of solar pressure can easily be included without any additional force terms, by only reducing the effective mass of the Sun. This is the case because both the gravitation and the solar pressure forces are inversely proportional

to distance square (i.e. $F \propto \frac{1}{r^2}$), only differing by a constant.

The aim is to find real solar trajectories that have the same characteristics as the quasi-periodic orbits obtained in this chapter. Thus, the algorithm first takes the orbits in the CRTBP and converts them from the synodical frame to the solar frame. For astronomically simplified models, better results are obtained when the Earth/Moon system is treated as a single planet with the center-of-mass at the Earth/Moon Barycenter, than when the effect of the Moon is ignored in the model.

I employ the usual synodical frame, which has its center at the center-of-mass of the Sun-Earth/Moon Barycenter system, to map the CRTBP results to the full solar model, and I find that the large distance between the Sun and the spacecraft trajectory leads to undesirable behavior. Multiplying small errors with this large distance leads to non-convergent transfers. Thus, I move the position of the axis center from the usual definition, which is the center-of-mass of the Sun-Earth/Moon Barycenter system, to the Earth/Moon Barycenter. In order to map the synodical coordinates to solar coordinates, the following steps are taken.

In what follows, subscripts $_{cm}$, $_{syn}$, $_{sun}$, $_{em}$, and $_{e/s}$ refer, respectively, to the center-of-mass synodical frame, the Sun, the Earth/Moon Barycenter, and the Earth/Moon Barycenter with respect to the Sun. Superscripts ^{R} and ^{I} refer to the rotating and the inertial coordinates. r and v are the position and velocity components of the spacecraft. Finally, R and V are the position and velocity components of the solar system bodies with respect to the solar system center-of-mass, unless specified otherwise.

1. First, the position and velocities of the Sun, the Earth/Moon Barycenter, and their relative distances are obtained from DE-406:

$$\vec{\mathbf{R}}_{e/s} = \vec{\mathbf{R}}_{em} - \vec{\mathbf{R}}_{sun} \,. \tag{4.59}$$

2. The position, velocity and rotation rate of the rotating frame are calculated:

$$\begin{aligned} \vec{\mathbf{R}}_{cm} &= \vec{\mathbf{R}}_{em}\,, \\ \vec{\mathbf{V}}_{cm} &= \vec{\mathbf{V}}_{em}\,, \\ \vec{\omega}_{syn} &= \frac{\vec{\mathbf{R}}_{s/e} \times \vec{\mathbf{R}}_{s/e}}{|\vec{\mathbf{R}}_{s/e}|^2}\,. \end{aligned} \tag{4.60}$$

3. $(1-\mu)$ is subtracted from the x-coordinates of the synodical frame elements, and the synodical elements are multiplied with the length and time scale to redimensionize the coordinates:

$$\begin{aligned} \vec{\mathbf{r}}^{R}_{syn} &= ||\vec{\mathbf{R}}_{s/e}|| \;\; \left(\vec{\mathbf{r}}^{R}_{syn} - \{\, 1-\mu,\, 0,\, 0\,\}^T\right)\,, \\ \vec{\mathbf{v}}^{R}_{syn} &= ||\vec{\mathbf{R}}_{s/e}|| \;\; ||\vec{\omega}_{syn}|| \;\; \vec{\mathbf{v}}^{R}_{syn}\,. \end{aligned} \tag{4.61}$$

4. The rotation matrix is obtained from the synodical frame to inertial frame:

$$\mathcal{R} = [\,\hat{e}_1\,\hat{e}_2\,\hat{e}_3\,]\,, \tag{4.62}$$

where

$$\hat{e}_1 = \frac{\vec{\mathbf{R}}_{s/e}}{||\vec{\mathbf{R}}_{s/e}||}\,, \quad \hat{e}_3 = \frac{\vec{\omega}_{syn}}{||\vec{\omega}_{syn}||}\,, \quad \text{and} \quad \hat{e}_2 = \frac{\hat{e}_3 \times \hat{e}_1}{||\hat{e}_3 \times \hat{e}_1||}\,. \tag{4.63}$$

5. The synodical coordinates are expressed in inertial frame coordinates:

$$\begin{aligned} \vec{\mathbf{r}}^{I}_{syn} &= \mathcal{R}\,\vec{\mathbf{r}}^{R}_{syn}\,, \\ \vec{\mathbf{v}}^{I}_{syn} &= \mathcal{R}\,\vec{\mathbf{v}}^{R}_{syn}\,. \end{aligned} \tag{4.64}$$

6. Finally, the inertial position, $\vec{\mathbf{r}}^{I}_{solar}$, and velocity, $\vec{\mathbf{r}}^{I}_{solar}$, of the spacecraft are

found with respect to the solar center-of-mass:

$$\begin{aligned} \vec{\mathbf{r}}^{I}_{solar} &= \vec{\mathbf{r}}^{I}_{syn} + \vec{\mathbf{R}}_{cm}\,, \\ \vec{\mathbf{v}}^{I}_{solar} &= \vec{\mathbf{v}}^{I}_{syn} + \vec{\omega}_{syn} \times \vec{\mathbf{r}}^{I}_{syn} + \vec{\mathbf{V}}_{cm}\,. \end{aligned} \tag{4.65}$$

Once the position and velocities are mapped to solar system coordinates, I take these orbits as initial guesses, and find the natural orbits in the full ephemeris model that stay close to them. My approach to this problem was to take an orbit for a specified time interval, which would be the time frame of the mission, and to feed this guess to the collocation algorithm. However, this time, I ran the algorithm without boundary conditions (see section 3.1.1 for details of the implementation). Thus, without any constraints, I look for an orbit that satisfies the full Solar System ODE, starting with the initial guess obtained from the CRTBP. The result is a natural orbit of the Solar System which is very close in shape and characteristics to the CRTBP orbit.

The main advantage of this approach is that all the available information, i.e., the full guess for the orbit, is used. This is helpful because the Halo and Quasi-Halo orbits around L2 are unstable, and long-term integration with bad initial guesses might lead to trajectories that diverge from the original orbit. Thus, I employ a collocation algorithm, which is a robust boundary value problem-solving technique.

Finally, for visualization purposes, the results in the solar coordinates are converted back to the synodical frame by applying the algorithm backwards. Figures 4.17, 4.18, and 4.19 show the results for three different types of orbits - Halo, Quasi-Halo and Lissajous orbits - around the Sun-Earth L2 point, transferred to the JPL DE-406 model.

The collocation algorithm performs robustly around the Sun-Earth L2 point where the missions of our interest will be located. I also implemented the multiple shoot-

ing algorithm, developed by Gómez et al. [46] for the Quasi-Halo refinement. The obtained results and the computation time from both methods are similar. Further comparisons, including the more computationally challenging orbits of the Earth-Moon system, will be performed as part of future research.

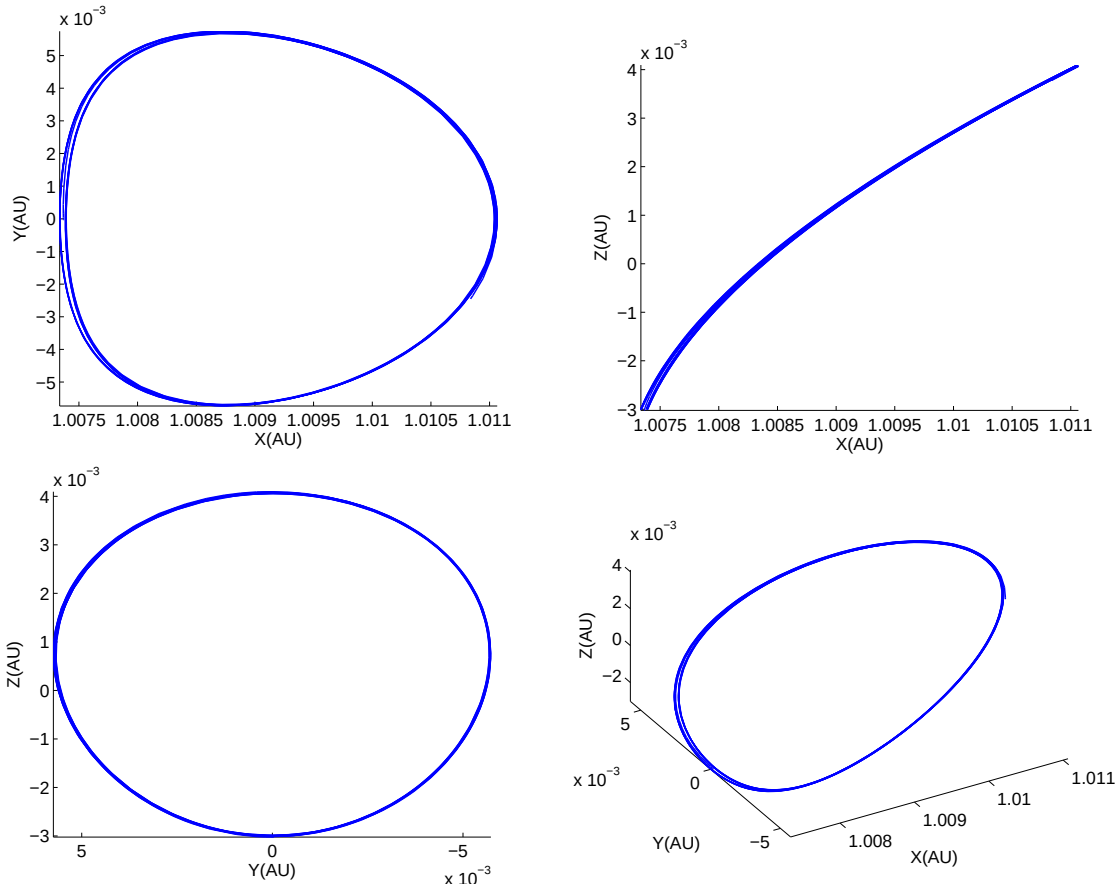

Figure 4.17: An example of a Halo orbit around L2 transferred to the JPL DE-406 model

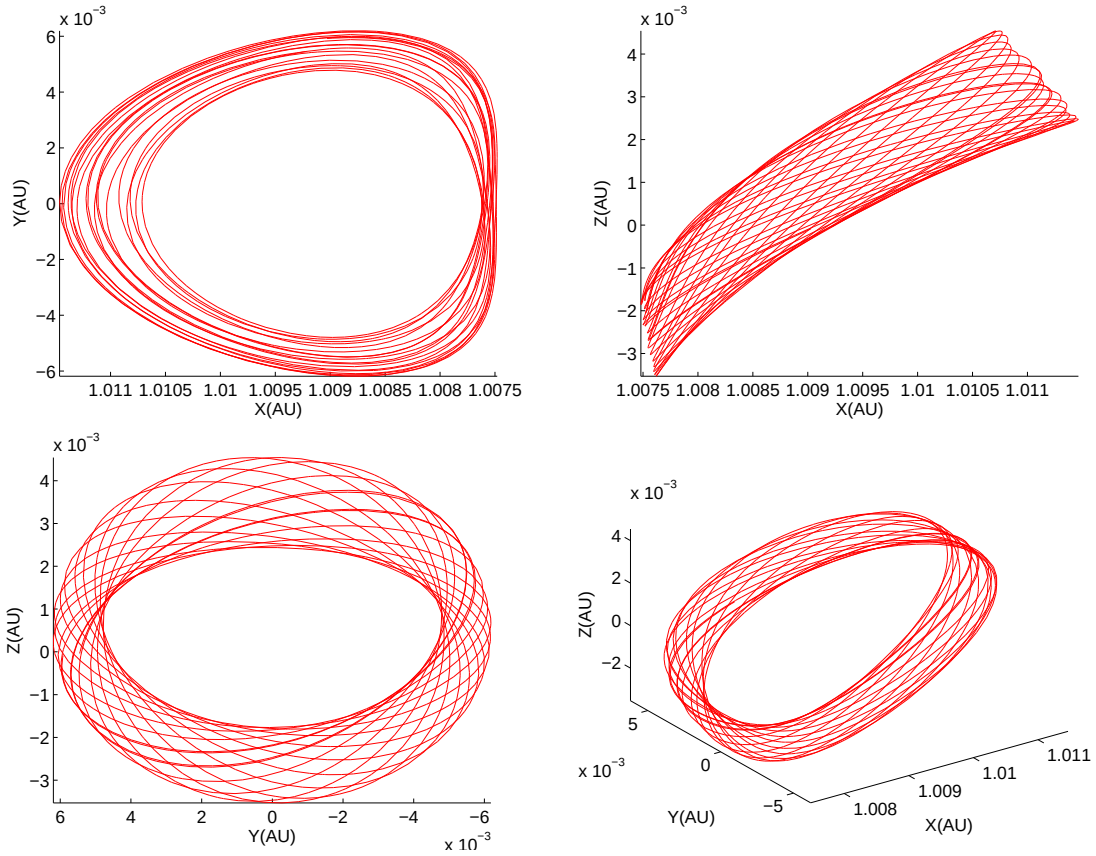

Figure 4.18: An example of a Quasi-Halo orbit around L2 transferred to the JPL DE-406 model

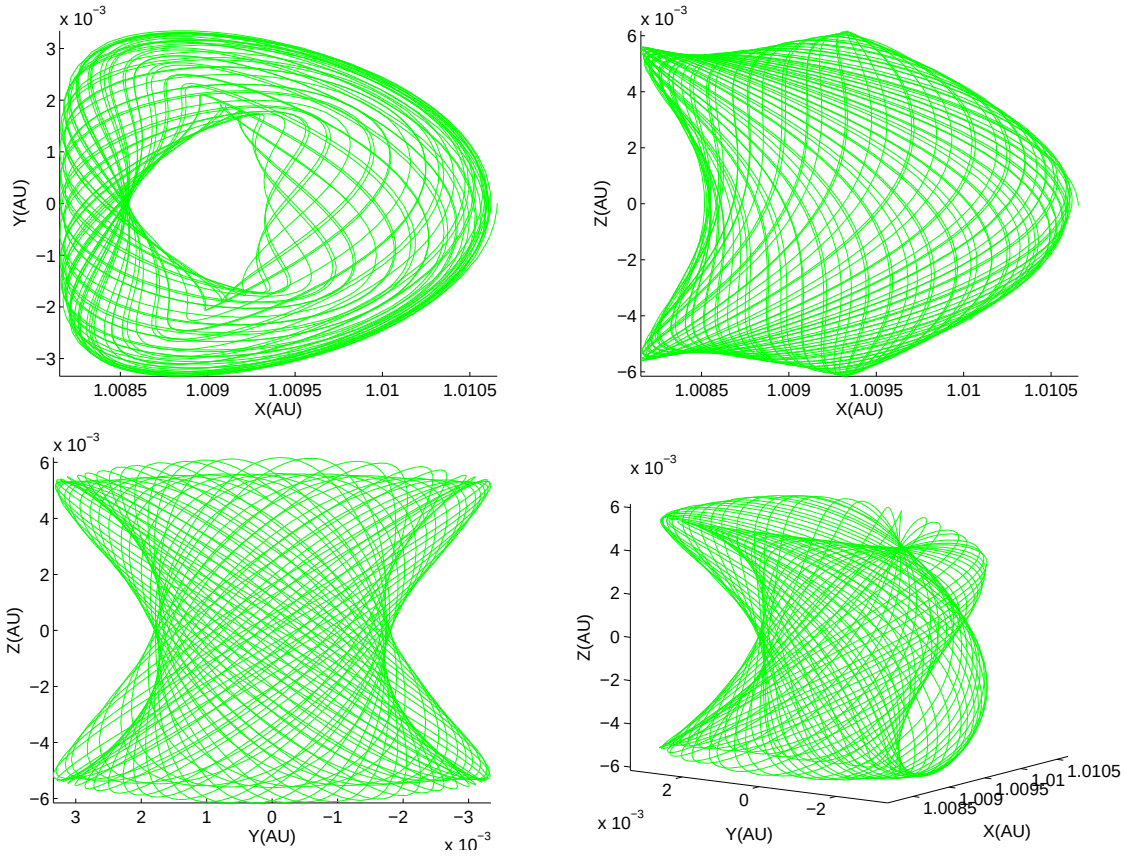

Figure 4.19: An example of a Lissajous orbit around L2 transferred to the JPL DE-406 model

Chapter 5

Finding the Optimal Trajectories

The control problem can be separated into two parts; first, the line-of-sight (LOS) control of the formation during imaging, and second, the trajectory control for maneuvering the occulter from one star LOS to another between imaging sessions, i.e., the realignment maneuver. Here, I focus on the latter, since the realignment dominates the Delta-V budget. In this chapter, I find the optimal trajectories for the realignment processes. Although this is not the main aim of this chapter, I also solved for the optimal trajectories from Earth to Halo orbits as a sample problem for the control algorithms that were developed, and to give an idea about the transfer trajectories.

5.1 Different Optimal Control Approaches

During the imaging of a given planetary system, the telescope and the occulter must be aligned to the LOS of the star position. Thus, the inertial velocities of the telescope and the occulter should be the same. In addition, the optics of the diffraction pattern are such that the telescope will most probably be designed for a prespecified constant occulter-telescope separation. Thus, based on this optical constraint, the distance between the occulter and the telescope should be roughly the same for all observations. This fixes the position of the occulter to be on a sphere around the telescope. The realignment problem then becomes one of finding an optimal trajectory between two two-dimensional surfaces, as shown in figure 5.1. I examine six optimization strategies for the realignment. Depending on the type of thruster the mission uses, either continuous or discrete control might be needed. Since the most probable devices are Hall-type thrusters, where we have access to continuous, low magnitude thrust throughout the trajectory, I studied five continuous thrust methods (and one discrete one). For all the control algorithms developed in this chapter, I assume that the there is a single thruster that can be instantaneously thrusted towards any direction

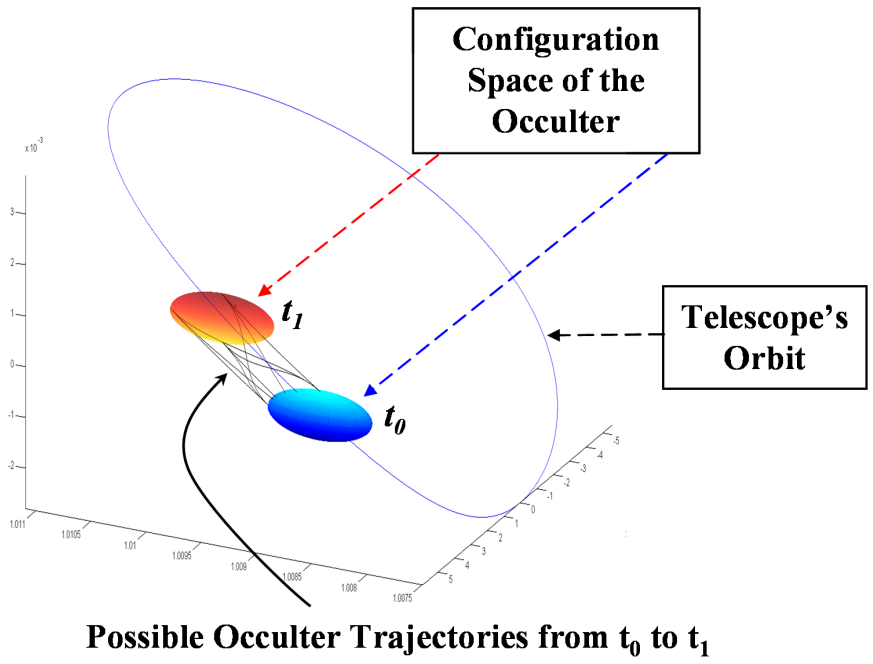

Figure 5.1: The sphere of possible occulter locations about the telescope at two times, and example optimal trajectories connecting them

of choice.

First, we look at the optimal control problem of finding the trajectory that takes the occulter from a given star LOS to another star LOS, the realignment maneuver. Here it is presupposed continuous thrust between two given star LOS's with a given time of flight. In this case, I examined the point-to-point transfer in the phase space with an energy-cost function. While this is not the most physically meaningful of the cost functions, its quadratic nature makes it easier to solve and it was used as the initial feed for other types of optimizations. The second optimization leaves out the time of flight but adds a constraint on the maximum thrust. The third option presumes continuous thrust and knowledge of the initial condition but the end point is free to be in any position on the spherical configuration space.

The fourth optimization focuses on the trajectories that minimize fuel consumption, where the magnitude of the control effort was minimized. The fifth option finds the minimum-time optimal trajectories between the phase space points. Finally, there

is the discrete control consisting of two impulsive Delta-V maneuvers, one at the beginning and one at the end of the trajectory.

In the following sections, I go over these six different optimization strategies, and I discuss the approaches taken to solve the optimal control problem that arises from these different assumptions. Before going any further, I first review the general optimal control problem.

The stars to be observed were taken from the list with the most suitable 100 stars for the TPF-C mission [59]. I then used the astrometrical data from the Hipparcos astronomical catalog [60]. I employed the NOVAS routines developed by Kaplan [61] to convert and update the exact star locations of the target stars relative to the Solar system, starting from 1 January 2010, the mission start day of my choice. For high-fidelity applications, I developed the capability to use the full nonlinear solar system model based on the JPL DE-406 ephemeris [57] for differential equations. However, in the analysis to follow, the CRTBP simplified model is used for the dynamical model, and a uniformly rotating star model is employed for the star locations for faster calculations.

For ease of comparison, all the missions scenarios discussed from here on assume a base Halo orbit around L2 with an out-of-plane amplitude of 500,000 km.

5.1.1 The Euler-Lagrange Formulation of the Optimal Control Problem (Indirect Method)

The Euler-Lagrange method, otherwise known as the adjoint method, employs the variational calculus to find the optimal control of a differential system. Here I only outline the methodology; for details see Stengel [62] and Bryson & Ho [63]. I wish to find a trajectory, $\mathbf{x}(t)$, and control, $\mathbf{u}(t)$, that minimizes the cost function, J, in the

time interval $[t_0,\, t_f]$,

$$J = \phi(\mathbf{x}(t_f)) + \int_{t_0}^{t_f} L(t, \mathbf{x}, \mathbf{u}) dt \tag{5.1}$$

subjected to the ordinary differential equations,

$$\dot{\mathbf{x}} = \mathbf{f}(t, \mathbf{x}, \mathbf{u}) \tag{5.2}$$

with boundary conditions at each end of the interval

$$\mathbf{x}(t_0) = \mathbf{x_0} \quad \text{and} \quad \psi(t_f) = 0\,, \tag{5.3}$$

for some terminal function $\psi(t_f)$. The Euler-Lagrange equations give the optimal solution path as a BVP with a differential algebraic equation in terms of the augmented state consisting of the normal state vector, $\mathbf{x}$, and an additional state vector, λ, called the adjoint states,

$$\dot{\mathbf{x}} = \mathbf{f}(t, \mathbf{x}, \mathbf{u})\ , \tag{5.4}$$

$$\dot{\lambda} = -\left(\frac{\partial H(t, \mathbf{x}, \mathbf{u}, \lambda)}{\partial \mathbf{x}}\right)^T \tag{5.5}$$

$$\mathbf{0} = \frac{\partial H(t, \mathbf{x}, \mathbf{u}, \lambda)}{\partial \mathbf{u}}\,. \tag{5.6}$$

In addition to the boundary conditions given in equation 5.3, the algebraic differential equations are subjected to the following additional boundary conditions given for the adjoint states at the final time:

$$\lambda(t_f) = \left(\frac{\partial G(t_f, \mathbf{x}(t_f), \nu)}{\partial \mathbf{x}(t_f)}\right)^T\ . \tag{5.7}$$

In these equations, H, the Hamiltonian, and G are given as

$$H(t, \mathbf{x}, \mathbf{u}) = L(t, \mathbf{x}, \mathbf{u}) + \lambda^T f(t, \mathbf{x}, \mathbf{u}) \,, \tag{5.8}$$

$$G(t_f, \mathbf{x}(t_f), \nu) = \phi(\mathbf{x}(t_f)) + \nu^T \psi(\mathbf{x}(t_f)). \tag{5.9}$$

The main advantage of using the Euler-Lagrange formulation is that the optimality of the solution can be checked, and the computational effort for solving the BVP using shooting or collocation methods will be minimal if a feasible solution can be found. The main disadvantage of this formulation is that it may be difficult to generate sufficiently good initial guesses for the adjoint states.

5.1.2 The Sequential Quadratic Programming Formulation of the Optimal Control Problem (Direct Method)

The second approach to solving optimization problem defined in equations 5.2, 5.1, and 5.3 is to discretize integral and states and solve a high-dimensional nonlinear optimization problem via an appropriate nonlinear optimization algorithm. I discuss such algorithms at the end of the section. Since there are no intermediate steps, such as the introduction of the adjoint state, involved in solving the problem, numerical methods that employ nonlinear programming algorithms to solve the discretized optimal control problem are called the direct method. Here I give an brief overview of the direct method see Betts [64] for details. In this method, first the time interval is discretized,

$$t_{initial} = t_0 < t_1 \ldots < t_{N-1} < t_N = t_{final}. \tag{5.10}$$

Then, the continuous state vector, $\mathbf{x}(t)$, is approximated at these time points, $\mathbf{x}_i = \mathbf{x}(t_i)$, at each time point t_i. The continuous control variables, $\mathbf{u}(t)$, are approximated

between the time intervals $[t_i, , t_{i+1}]$ as $u_i = u(t_i)$ (for example, a zero-order hold). If our guess is sufficiently close to the real solution, the discretized quadrature equation corresponds to the differential equation. For instance, a first-order discretization of the differential given in equation 5.2 in the middle of every time interval leads to

$$\dot{\mathbf{x}}_i \approx \frac{\mathbf{x}_{i+1} - \mathbf{x}_i}{h_i} \tag{5.11}$$

$$\approx \mathbf{f}\left(\bar{t}_i, \bar{\mathbf{x}}_i, \mathbf{u}_i\right) , \tag{5.12}$$

where

$$\bar{t}_i := \frac{t_{i+1} - t_i}{2} \text{ and } \bar{\mathbf{x}}_i := \frac{\mathbf{x}_{i+1} - \mathbf{x}_i}{2} , \tag{5.13}$$

and $h_i = t_{i+1} - t_i$. Thus, the differential constraint is converted to an algebraic one,

$$0 = F(\bar{t}, \bar{\mathbf{x}}, \mathbf{u}) . \tag{5.14}$$

There are many other possible discretization schemes; the Euler type discretization is used here for illustration. Along with the differential equation, the cost function and the constraints, if the latter exist, are discretized as well.

$$J(t_i, \mathbf{x}_i, \mathbf{u}_i = \phi(\mathbf{x}(t_f)) + \sum_{i=0}^{N} L(t_i, \mathbf{x}_i, \mathbf{u}_i) h_i \tag{5.15}$$

Then, the constraint vector is augmented with inequality conditions such that

$$\begin{aligned} F_i &= 0, \quad i \in \mathcal{E} \\ F_i &< 0, \quad i \in \mathcal{I} , \end{aligned} \tag{5.16}$$

where $\mathcal{E}$ and $\mathcal{I}$ are the sets of indices for equality and inequality constraints, respectively. The high-dimensional discrete nonlinear optimization problem (NLP) is formulated as

$$\text{[NLP]:} \quad \min\{J(\xi) \ : \ F_i(\xi) = 0, \ i \in \mathcal{E}, \quad F_i(\xi) < 0, \ i \in \mathcal{I}\}, \tag{5.17}$$

where $\xi = \{\mathbf{x}_i, \mathbf{u}_i\}$ is the augmented variables vector. This NLP is solved via a nonlinear optimization algorithm.

One of the most efficient and promising methods currently in use is the sequential programming algorithm (SQP). The SQP algorithm is a generalization of Newton's method for unconstrained optimization in that it finds a step away from the current point by minimizing a quadratic model of the problem. The SQP algorithm replaces the objective function, $J(\xi)$, with a quadratic approximation and replaces the constraint functions by linear approximations. A more detailed overview of the SQP method can be found in Gill et al. [65].

I utilized the IPOPT [66], a open-source interior point method SQP-solver software, and the MATLAB optimization toolbox software $fmincon$. To minimize the time it takes to convert the optimal control problem to a form that can be used with the direct method, I created an automated symbolic software. This algorithm discretizes the optimal control problem, which is defined effortlessly in MATLAB. It then symbolically converts the problem to the form needed by the SQP solver. This code is then converted and compiled in FORTRAN which is much faster than MATLAB. These compiled functions are in a form that can be called from within a MATLAB script (see MATLAB's "mex" [67] utility for more information). This enables me to solve the problem without leaving the convenience of the MATLAB environment while benefiting from the speed of the FORTRAN's fast compiler. The software allows for a choice between many different discretization methods, such as Runge-Kutta, Euler,

and trapezoidal, in order to suit the needs of the specific problem. I hope to make this software available for the public soon.

5.2 Unconstrained Minimum Energy Optimization

In this approach, I assume that the control variable is the acceleration of the spacecraft due to the force applied by the thrusters throughout its trajectory, $\mathbf{u} = (\frac{d^2\mathbf{x}}{dt^2})_{thruster}$. Then, the effect of the control can be added to the normal control-free Newtonian equations such that

$$\dot{\mathbf{x}} = \mathbf{f}_{ctr}(t, \mathbf{x}, \mathbf{u}) \,, \tag{5.18}$$

where

$$\mathbf{f}_{ctr}(t, \mathbf{x}, \mathbf{u}) = \mathbf{f}(t, \mathbf{x}) + \{\, 0,\, 0,\, 0,\, u_x,\, u_y,\, u_z \,\}^T \,, \tag{5.19}$$

and where the control vector, $\mathbf{u}$, is defined as $\mathbf{u} = \{\, u_x,\, u_y,\, u_z \,\}^T$. My aim is to minimize the control effort given these differential equations of motion. In this section, I use a cost function of the quadratic form,

$$J = \int_{t_0}^{t_f} \frac{1}{2}\mathbf{u} \cdot \mathbf{u} \; dt \,. \tag{5.20}$$

Here, I use the notation, $\cdot$, for the dot product of vectors. The Hamiltonian for this optimal control problem is

$$H(t, \mathbf{x}, \lambda, \mathbf{u}) = \frac{1}{2}\mathbf{u} \cdot \mathbf{u} + \lambda^T \mathbf{f}(t, \mathbf{x}) + \mathbf{p}^T \mathbf{u} \,, \tag{5.21}$$

where I use the intermediate variable, $\mathbf{p}$, which is the last three elements of the adjoint vector:

$$\mathbf{p} = \{\, \lambda_4,\, \lambda_5,\, \lambda_6 \,\}^T. \tag{5.22}$$

In this section, I consider the point-to-point optimal control, where both the initial and final states are fixed a priori.

$$\psi(t_f) = \mathbf{x}(t_f) - \mathbf{x_f} = 0 \tag{5.23}$$

Solving the optimality condition,

$$\mathbf{0} = \frac{\partial H(t, \mathbf{x}, \lambda, \mathbf{u})}{\partial \mathbf{u}} \tag{5.24}$$

I obtain,

$$\mathbf{u} = -\mathbf{p}\,. \tag{5.25}$$

Substituting for $\mathbf{u}$ in the Euler-Lagrange equations, I obtain a 12-degree ODE in terms of the state and adjoint state only:

$$\begin{aligned} \dot{\mathbf{x}} &= \mathbf{f}(t, \mathbf{x}, \lambda)\ , \\ \dot{\lambda} &= -\left(\frac{\partial \mathbf{f}(t, \mathbf{x})}{\partial \mathbf{x}}\right)^T \lambda\,, \end{aligned} \tag{5.26}$$

with twelve boundary conditions

$$\begin{pmatrix} \mathbf{x}(t_0) - \mathbf{x_0} \\ \mathbf{x}(t_f) - \mathbf{x_f} \end{pmatrix} = \mathbf{0}\ . \tag{5.27}$$

To make sure that this solution is indeed an optimal solution of the problem, I check that the Legendre-Clebsch and Weierstrass conditions are satisfied:

$$\frac{\partial^2 H(t, \mathbf{x}, \mathbf{u}, \lambda)}{\partial \mathbf{u}^2} = I > 0 \, . \tag{5.28}$$

The BVP arising from the optimal control problem is solved using a collocation algorithm. As an example consider the transfer from Earth to an L2 Halo orbit. Let the final condition be on the Halo orbit with high z value to show the out-of-plane characteristic of the optimal trajectories. The initial orbit of the satellite around Earth and the final position on the Halo orbit are shown in figure 5.3. Below are the exact initial and final states in the normalized synodical units that I used for the orbit.

$$\mathbf{x_0} = \begin{pmatrix} 9.999969595766015\ 10^{-1} \\ -1.007824043999068\ 10^{-3} \\ 0 \\ 7.237761726886938\ 10^{-2} \\ 0 \\ 0 \end{pmatrix}, \quad \mathbf{x_f} = \begin{pmatrix} 1.011080356710551\ 10^{0} \\ 7.419127797265952\ 10^{-4} \\ 3.655679288769010\ 10^{-3} \\ 6.534277927644666\ 10^{-4} \\ -1.054583863270762\ 10^{-2} \\ 7.362873998458644\ 10^{-4} \end{pmatrix} . \tag{5.29}$$

I solved the optimal control problem with various time intervals and obtained the cost function as shown in figure 5.2. There is a local minimum of the cost at around 90 days, after which the cost increases until a time-of-flight of approximately 170 days. After that, the results from the BVP solver become very sensitive, most likely due to branching of the optimal trajectories. Figure 5.3 shows the optimal trajectory for a 90 day time-of-flight and figure 5.4 shows the optimal control throughout the trajectory.

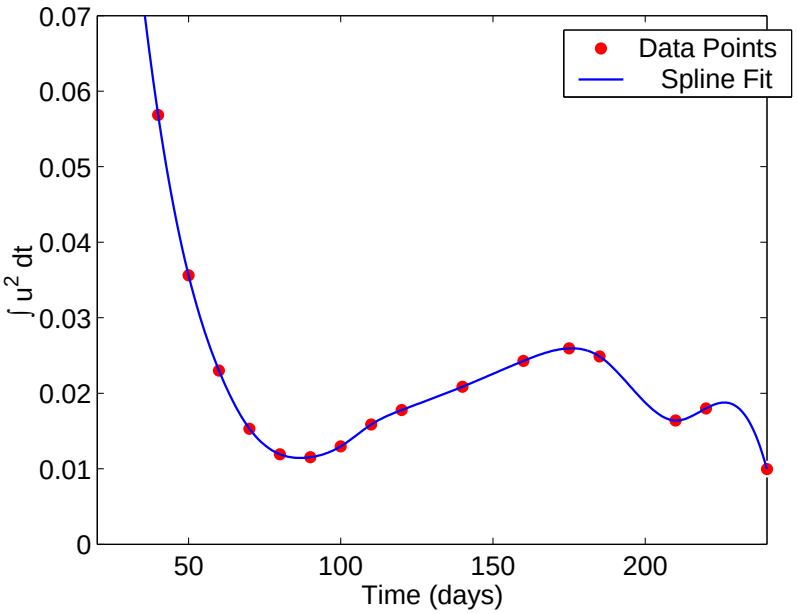

Figure 5.2: Dependence of the optimal quadratic cost function on the time-of-flight for Earth to Halo orbit transfers.

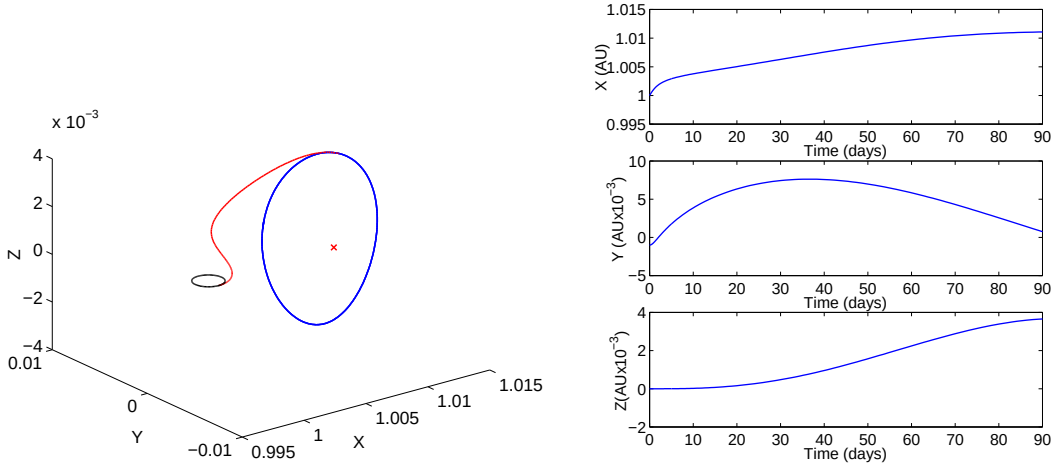

Figure 5.3: The optimal minimum-energy trajectory for the 90-day Earth to Halo transfer. Shown on the left, in red, is the three-dimensional trajectory. Shown on the right are the components of the position.

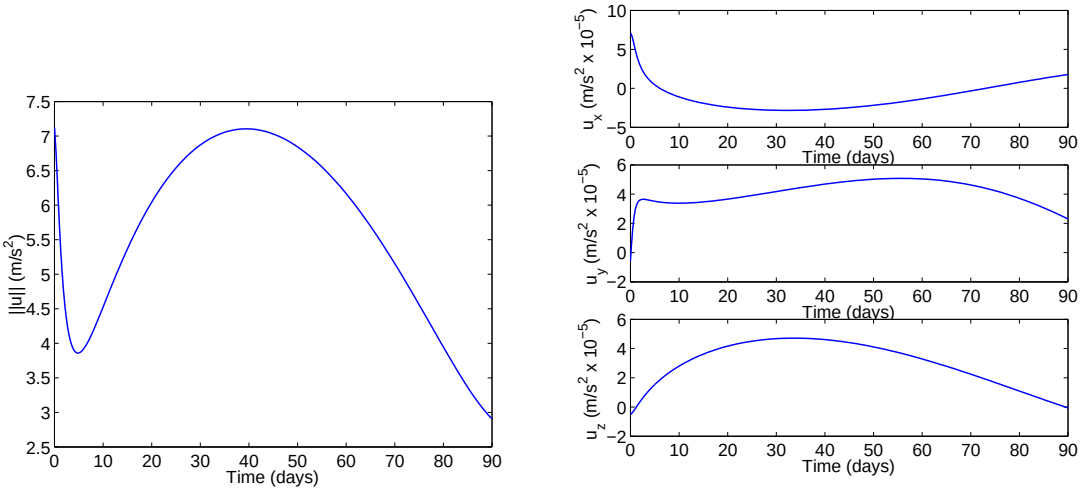

Figure 5.4: The optimal minimum-energy control effort for the 90-day Earth to Halo transfer. The magnitude of the control is shown on the left, while its components are shown on the right.

For the case of transfer from a star LOS to another, the occulter-to-telescope distance, R, of 50,000 km is used. For the time-of-flight, I chose two weeks which is a representative slew time for the mission under study. I assumed the telescope to be on a Halo orbit, and I assume that the first star the occulter-telescope formation looks at is in the direction given by the unit vector $\hat{\mathbf{e}}_\mathbf{0}$ while the second star to be imaged is in direction of the unit vector $\hat{\mathbf{e}}_\mathbf{1}$. I chose $\hat{\mathbf{e}}_\mathbf{0}$ and $\hat{\mathbf{e}}_\mathbf{1}$ such that the angle between them in the order of a typical slew. The exact numerical values used in the example to follow are

$$\hat{\mathbf{e}}_\mathbf{0} = \begin{pmatrix} 6.324555320336759\ 10^{-1} \\ -6.324555320336759\ 10^{-1} \\ 4.472135954999580\ 10^{-1} \end{pmatrix}, \quad \hat{\mathbf{e}}_\mathbf{1} = \begin{pmatrix} 0 \\ 0 \\ 1 \end{pmatrix}, \tag{5.30}$$

such that the angle between the unit vector is 63 degrees. I obtained the star and

end positions the occulters from the unit vectors as

$$\mathbf{r_{occ}} = \mathbf{r_{tel}} + R\,\hat{\mathbf{e}}\,, \tag{5.31}$$

where $\mathbf{r_{occ}}$ and $\mathbf{r_{tel}}$ are the position of the occulter and the telescope in the synodical frame, respectively. I obtained the velocities based on the requirement that the inertial velocities of both the telescope and the occulter be the same,

$$\mathbf{v_{occ}} = \mathbf{v_{tel}} + \omega \times R\,\hat{\mathbf{e}}\,, \tag{5.32}$$

where $\mathbf{v_{occ}}$ and $\mathbf{v_{tel}}$ are the velocity of the occulter and the telescope, respectively, and $\omega = \{0, 0, 1\}^T$ is the angular velocity of the CTRBP. Thus, the numerical values in the normalized synodical units for the BVP algorithm are

$$\mathbf{x_0} = \begin{pmatrix} 1.008708480181499\ 10^{0} \\ 5.219658053604695\ 10^{-3} \\ 1.494719120781122\ 10^{-4} \\ 3.123278717913480\ 10^{-3} \\ 2.077725728577118\ 10^{-3} \\ 6.483432393011172\ 10^{-3} \end{pmatrix}, \quad \mathbf{x_f} = \begin{pmatrix} 1.009397510830226\ 10^{0} \\ 5.341370714348193\ 10^{-3} \\ 1.843136365772625\ 10^{-3} \\ 3.951895067977367\ 10^{-3} \\ -2.937081366176431\ 10^{-3} \\ 5.838803068471303\ 10^{-3} \end{pmatrix}. \tag{5.33}$$

Figure 5.5 shows the optimal trajectory of the occulter relative to the telescope on the Halo orbit. Figure 5.6 shows the optimal control throughout the trajectory.

5.3 Constrained Minimum Energy Optimization

Next, I add an inequality constraint on the control to the minimum energy problem. The magnitude of the control vector, $|\mathbf{u}|$, must be less than a specified limit, u_{max}, such that $|\mathbf{u}| < u_{max}$. The augmented Hamiltonian for the optimal control problem

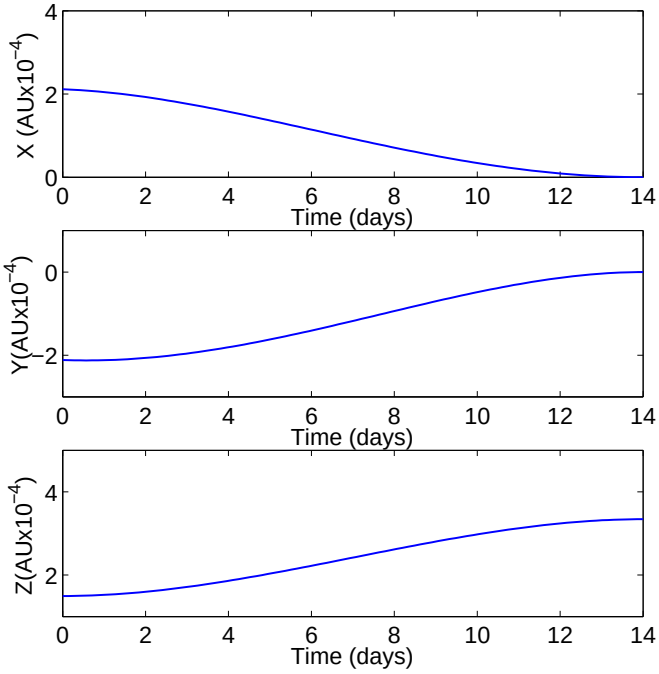

Figure 5.5: The trajectory of the occulter relative to the telescope for an energy-optimal realignment maneuver.

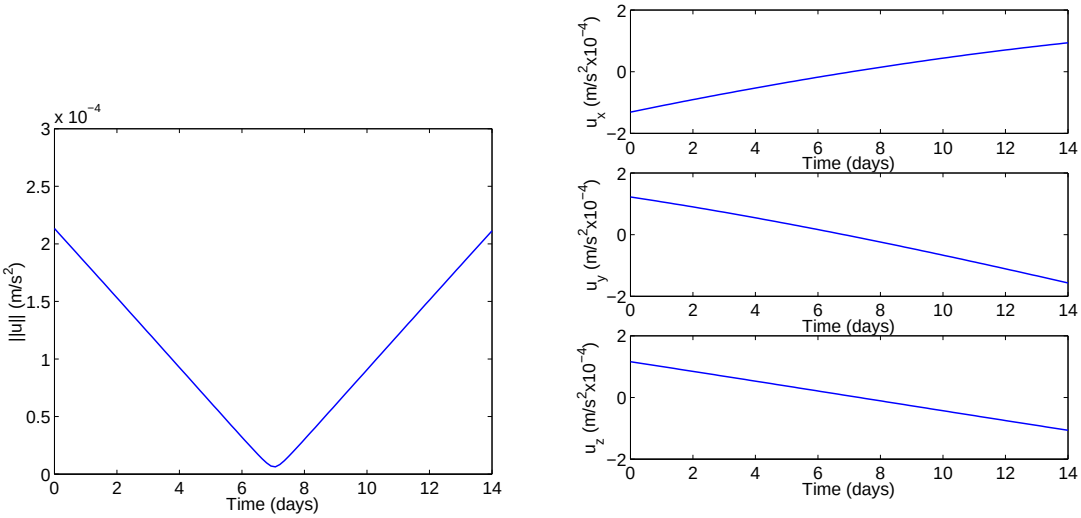

Figure 5.6: The optimal minimum-energy control effort for the realignment maneuver shown in figure 5.5. The magnitude of the control is shown on the left, while its components are shown on the right.

can be written as

$$H_{aug}(t,\mathbf{x},\lambda,\mathbf{u}) = \frac{1}{2}\mathbf{u}\cdot\mathbf{u} + \lambda^T\mathbf{f}(t,\mathbf{x}) + \mathbf{p}^T\mathbf{u} + \mu_{eff}c_{eff}(\mathbf{u}) \begin{cases} \mu_{eff} = 0 \text{ if } c_{eff}(\mathbf{u}) < 0 \\ \mu_{eff} \geqslant 0 \text{ if } c_{eff}(\mathbf{u}) = 0\,, \end{cases} \tag{5.34}$$

where $c_{eff}(\mathbf{u})$ is the inequality constraint function effective on the boundary,

$$c_{eff}(\mathbf{u}) = \mathbf{u}\cdot\mathbf{u} - u_{max}^2 \leqslant 0\,, \tag{5.35}$$

and μ_{eff} is the corresponding Lagrange multiplier.

Since c_{eff} is only a function of $\mathbf{u}$, the adjoint differential equations are not altered. However, the condition for control optimality becomes

$$\mathbf{0} = \frac{\partial H}{\partial \mathbf{u}}^T = \begin{cases} \mathbf{u}+\mathbf{p}, & c_{eff} < 0 \\ \mathbf{u}+\mathbf{p}+2\mu_{eff}\mathbf{u}, & c_{eff} = 0\,. \end{cases} \tag{5.36}$$

Solving the first part of the equation gives $\mathbf{u} = -\mathbf{p}$, as before. The second part asks that the following two equations be satisfied:

$$\mathbf{u} = -\frac{\mathbf{p}}{1+2\mu_{eff}} \quad \text{and} \quad |\mathbf{u}| = u_{max}\,, \tag{5.37}$$

which are solved to give

$$\mathbf{u} = \pm u_{max}\frac{\mathbf{p}}{|\mathbf{p}|}\,. \tag{5.38}$$

In order to decide which sign the control should take, I use the Pontryagin's Minimum Principle (See Stengel for details [62]), which states that the optimal control, $\mathbf{u}^*$, in

the set of feasible controls $\mathcal{U}$ is

$$\mathbf{u}^*(\mathbf{t}) = \arg\left\{\min_{\mathbf{u}(t)\in\mathcal{U}} H(t,\mathbf{x},\mathbf{u},\lambda)\right\} \ . \tag{5.39}$$

Looking at the part of the Hamiltonian with control influence, I obtain

$$\frac{1}{2}\mathbf{u}^*\cdot\mathbf{u}^* + \mathbf{p}^{*T}\mathbf{u}^* \leqslant \frac{1}{2}\mathbf{u}\cdot\mathbf{u} + \mathbf{p}^{*T}\mathbf{u}\,, \tag{5.40}$$

where the superscript $\{^*\}$ denotes the optimal elements. Now it becomes apparent that the correct choice of the sign is minus. This defines the optimal control as

$$\mathbf{u} = \begin{cases} -\mathbf{p} & \text{if } |\mathbf{p}| \leqslant u_{max} \\ -u_{max}\,\frac{\mathbf{p}}{|\mathbf{p}|} & \text{if } |\mathbf{p}| > u_{max}\,. \end{cases} \tag{5.41}$$

Substituting for $\mathbf{u}$ in the Euler Lagrange equations, I obtain a 12-degree ODE in terms of the state and adjoint state only:

$$\begin{aligned} \dot{\mathbf{x}} &= \mathbf{f}(t,\mathbf{x},\lambda) \\ \dot{\lambda} &= -\left(\frac{\partial\mathbf{f}(t,\mathbf{x},\lambda)}{\partial\mathbf{x}}\right)^T\lambda\,, \end{aligned} \tag{5.42}$$

with boundary conditions

$$\begin{pmatrix} \mathbf{x}(t_0) - \mathbf{x_0} \\ \mathbf{x}(t_f) - \mathbf{x_f} \end{pmatrix} = \mathbf{0}\ . \tag{5.43}$$

Considering applications, I first looked at the Earth-to-halo transfer optimization. While solving the constrained optimization problem, I used the same $\mathbf{x_0}$ and $\mathbf{x_f}$ given in equation 5.29 in the last section, and I used the solutions from the last section as the initial guess for the BVP. Figure 5.7 compares the trajectory of the satellite for the

Earth-to-Halo transfer from the bounded control such that $u_{max} = 6.1e-5$. Figure 5.8, on the right, shows the optimal control effort and compares it with the unbounded control case. How the norm of the control changes with maximum allowable control is shown in figure 5.8 on the left. For a given u_{max}, there is no guarantee that a 90 day transfer trajectory from Earth to Halo orbit exists. As seen from the figures 5.8, for $u_{max} < 6e-5$ the control power is not enough to reach the destination within 90 days span.

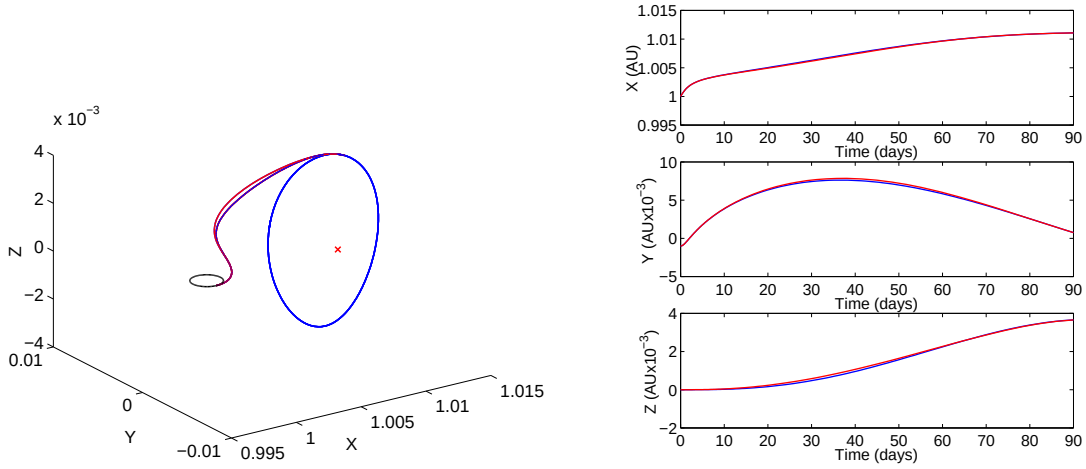

Figure 5.7: The optimal minimum-energy trajectory for the 90-day Earth to Halo transfer with bounded control. In red is the bounded optimal trajectory. The blue unbounded trajectory is also plotted for comparison.

Next, I considered the case of realignment maneuver. While solving the constrained optimization problem, I used the same $\mathbf{x_0}$ and $\mathbf{x_f}$ given in equation 5.33 in the last section, and I used the solutions from the last section as the initial guess for the BVP. Figure 5.9 shows the magnitude and the components of optimal control history throughout the trajectory.

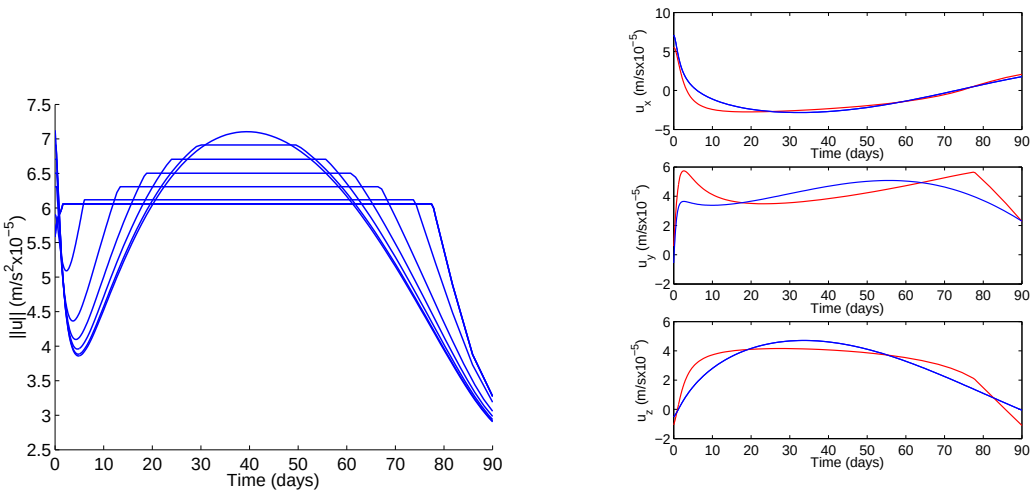

Figure 5.8: The optimal minimum-energy control effort for the 90-day Earth to Halo transfer with varying bounds on control. The effect of the varying bounds on the magnitude of the control effort is show on the left. The components of the control effort are show on the right; red for a bounded case and blue for the unbounded one.

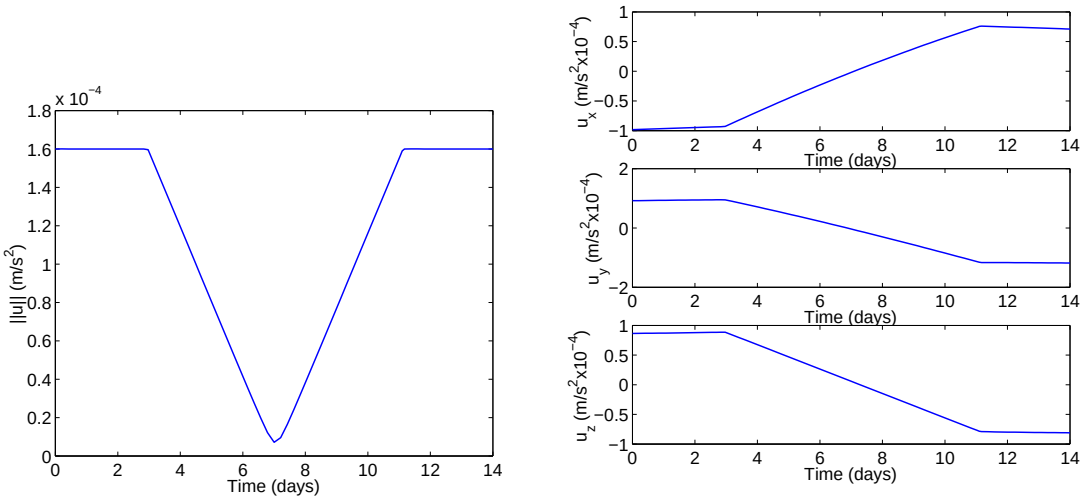

Figure 5.9: An optimal minimum-energy control effort for the realignment maneuver. The magnitude of the control is shown on the left, while its components are shown on the right.

5.4 Free-End Condition Optimization

The third optimization presumes continuous thrust and knowledge of the initial condition and leaves open the end point on the spherical configuration space at t_f. In this case, the initial state of the occulter, $\mathbf{x}(t_0) = \mathbf{x_0}$, is known at $t = t_0$, and I seek to find the target occulter state, $\mathbf{x}(t_f)$, at time t_f, that minimizes the energy cost function. Thus, the end time is fixed while the end position is free to change. Due to the optical requirements that were discussed previously, this final position, $\mathbf{x}(t_f)$, resides on the two-dimensional possible occulter locations at a given final time $t = t_f$. The Lagrangian and the differential equations are the same as before:

$$J = \int_{t_0}^{t_f} \frac{1}{2}\mathbf{u} \cdot \mathbf{u}\, dt\ . \tag{5.44}$$

The same Hamiltonian as before is also used:

$$H = \frac{1}{2}\mathbf{u} \cdot \mathbf{u} + \lambda^T \mathbf{f}(\mathbf{x}) + \mathbf{p}^T \mathbf{u}\,, \tag{5.45}$$

but instead of the six-dimensional equality constant, $\mathbf{x}(t_f) = \mathbf{x_f}$, at the end of the interval, now there are only four conditions. The first of these constraints is that the distance between the occulter and the telescope at the final time must be equal to the predefined radius, R. The other three are that the inertial velocity vector of the occulter and the telescope must be the same in order to be able to lock on a target star. Noting that the inertial velocity is

$$\mathbf{v}^{\Im} = \mathbf{v}^{\Re} + \omega \times \mathbf{r}\,, \tag{5.46}$$

where $\omega = \{0, 0, 1\}^T$, the final time constraint vector becomes

$$\psi(t_f) = \begin{pmatrix} (x(t_f) - x_h(t_f))^2 + (y(t_f) - y_h(t_f))^2 + (z(t_f) - z_h(t_f))^2 - R^2 \\ \dot{x}(t_f) - y(t_f) - (\dot{x}_h(t_f) - y_h(t_f)) \\ \dot{y}(t_f) + x(t_f) - (\dot{y}_h(t_f) + x_h(t_f)) \\ \dot{z}(t_f) - \dot{z}_h(t_f) \end{pmatrix} = 0 \ . \tag{5.47}$$

This four-dimensional condition does not change the differential equation for $\mathbf{x}$ and λ, but the final condition for the adjoint variables becomes

$$\lambda(t_f) = \left(\frac{\partial G(t_f, \mathbf{x_f}, \nu)}{\partial x(t_f)} \right)^T = \begin{pmatrix} \nu_1(x(t_f) - x_h(t_f)) + \nu_3 \\ \nu_1(y(t_f) - y_h(t_f)) - \nu_2 \\ \nu_1(z(t_f) - z_h(t_f) \\ \nu_2 \\ \nu_3 \\ \nu_4 \end{pmatrix} , \tag{5.48}$$

where the components of ν, the constant Lagrange multiplier vector corresponding to the end constraints, are given as $\nu = \{\nu_1, \nu_2, \nu_3, \nu_4\}$. Eliminating the elements of ν, these six equations can be turned into two constraints in term of $\lambda(t_f)$:

$$\psi_{add}(t_f) = \begin{pmatrix} -\lambda_1(t_f) + \lambda_3(t_f)\frac{x(t_f) - x_h(t_f)}{z(t_f) - z_h(t_f)} + \lambda_5 \\ -\lambda_2(t_f) + \lambda_3(t_f)\frac{y(t_f) - y_h(t_f)}{z(t_f) - z_h(t_f)} - \lambda_4 \end{pmatrix} \ . \tag{5.49}$$

With the addition of the four $\psi(t_f)$ constraints given in equation 5.47 on the final time and the six initial conditions, $x(t_0) = x_0$, I obtain the twelve boundary conditions

needed to solve the 12-dimensional BVP given in equation 5.6:

$$\begin{pmatrix} \mathbf{x}(\mathbf{t_0}) - \mathbf{x_0} \\ \psi(t_f) \\ \psi_{add}(t_f) \end{pmatrix} = 0\,. \tag{5.50}$$

I solved this BVP via collocation.

This hypothetical problem was specifically designed for the case of the realignment maneuver. While solving the free-end condition problem, I used the $\mathbf{x_0}$ that is given in equation 5.33, a time-of-flight of two weeks, and an R of 50,000 km, as before. I also used the solutions from the previous sections as the initial guess for the BVP. Figure 5.10 shows the relative trajectory of the occulter with respect to the telescope on the Halo orbit. As can be seen from figure 5.11, the control effort is two magnitudes smaller than in the previous examples of the fixed-end-point optimization cases.

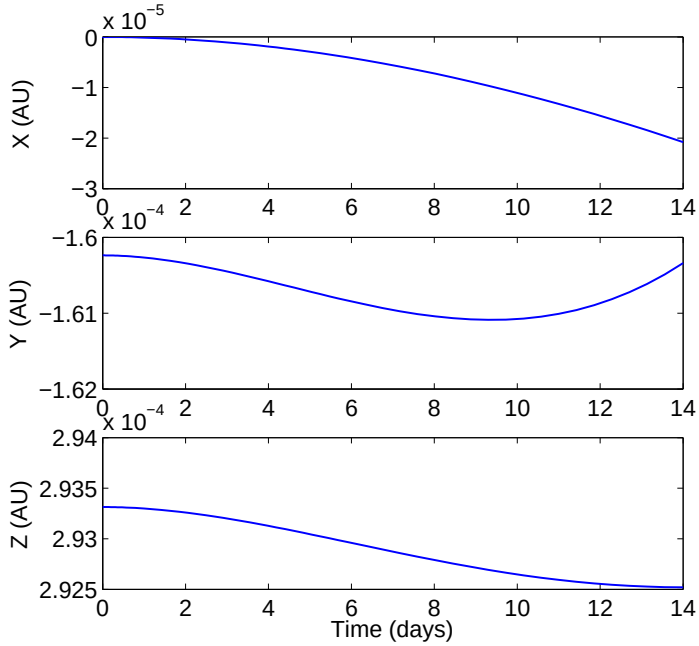

Figure 5.10: An optimal trajectory of the occulter relative to the telescope for an unprescribed end condition realignment maneuver.

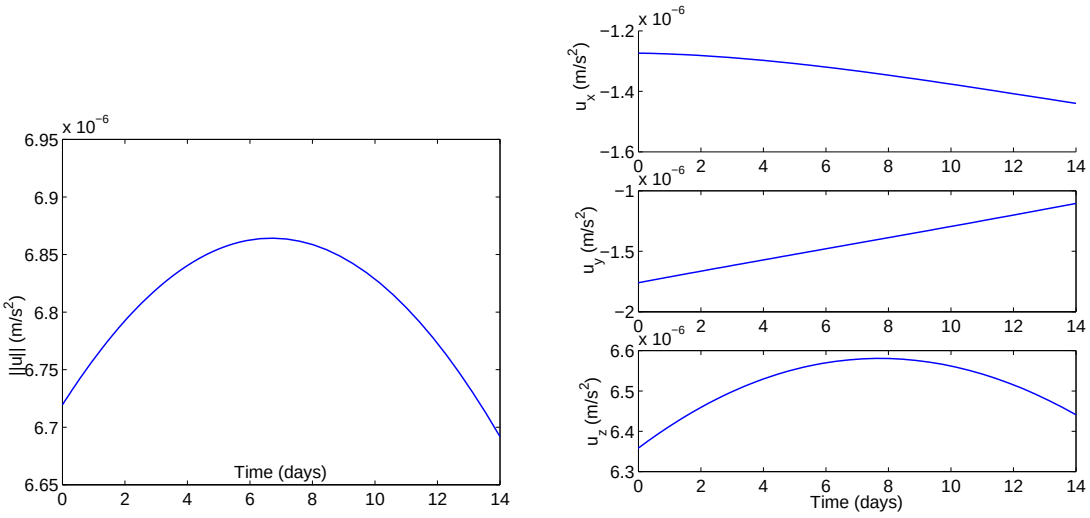

Figure 5.11: The open-ended optimal minimum-energy control effort for the realignment maneuver shown in figure 5.10. The magnitude of the control is shown on the left, while its components are shown on the right.

5.5 Minimum-Time Optimization

I now consider the realignment between two targets in minimum time under a maximum thrust constraint. In this case, I want to go from a point in phase space to another point in the minimum amount of time. The cost function thus becomes

$$J = \int_{t_0}^{t_f} 1 \, dt \, . \tag{5.51}$$

Since the minimum time solution dictates that the maximum control be employed at all times, I simplify the problem by redefining the control:

$$\mathbf{u} = u_{max} \, \hat{\mathbf{u}} \, . \tag{5.52}$$

Now I have a new constraint that needs to be satisfied throughout the trajectory:

$$\hat{\mathbf{u}} \cdot \hat{\mathbf{u}} = 1 \, . \tag{5.53}$$

I include this constraint in the Hamiltonian by augmenting it with additional Lagrange multipliers μ:

$$H = 1 + \lambda^T \mathbf{f}(\mathbf{x}) + u_{max}\mathbf{p}\hat{\mathbf{u}} + \mu(\hat{\mathbf{u}} \cdot \hat{\mathbf{u}} - 1)\,. \tag{5.54}$$

While the augmentation does not affect the adjoint differential equation, the optimality condition becomes

$$0 = \frac{\partial H}{\partial \hat{u}} = u_{max}\mathbf{p} + \mu\hat{\mathbf{u}}\,. \tag{5.55}$$

Thus, the optimal control $\hat{\mathbf{u}}$ can be obtained by solving this equation along with the constraint equation 5.53,

$$\mathbf{u} = \begin{cases} -u_{max}\frac{\mathbf{p}}{|\mathbf{p}|} & \text{if } |\mathbf{p}| \neq 0 \\ \text{undetermined} & \text{if } \mathbf{p} = \mathbf{0}\,. \end{cases} \tag{5.56}$$

Previously, I used the optimality condition and Pontryagin's Minimum Principle to determine $\mathbf{u}^*(t)$ for all time $t \in [t_0,\, t_f]$ in terms of the extremal states, $\mathbf{x}^*$, and adjoint states, λ^*. If, however, there is a time interval $[t_1,\, t_2]$ of finite duration during which this principle provides no information about the optimal control, then the problem is called singular and the interval $[t_1,\, t_2]$ is called the singular interval.

In order to determine whether it is possible to have singular intervals, the case where $\mathbf{p}$ is zero for finite time interval is considered. This condition implies that derivatives of all orders of $\mathbf{p}$ should be zero during that time interval. In other words,

$$\frac{d^k\mathbf{p}}{dt^k} = 0 \quad k{=}1,\, 2,\, \ldots \tag{5.57}$$

Writing the differential equation for $\mathbf{p}$ from the adjoint states ODE,

$$\dot{\mathbf{p}} = \begin{pmatrix} -\lambda_1 + 2p_2 \\ -\lambda_2 - 2p_1 \\ -\lambda_3 \end{pmatrix}, \tag{5.58}$$

we can see that the singularity condition leads to $\lambda = 0$. However, for the open-end-time problem under study there is another boundary condition. The Hamiltonian for the open-end-time problems, where it is not an explicit function of time, is equal to zero at all times (see Stengel [62] and Bryson & Ho [63] for details). Therefore, for the CRTBP where H is not an explicit function of time:

$$H = 0\,. \tag{5.59}$$

For the singular intervals, we know that $\lambda = \mathbf{0}$. Substituting this equality in the Hamiltonian, I obtain $H = 1$, which leads to a contradiction. Thus, there cannot be singular intervals for this minimum-time optimization problem.

Substituting for $\hat{\mathbf{u}}$ in the Euler-Lagrange equations, I obtain a 12-degree ODE in terms of the state and adjoint state only:

$$\begin{aligned} \dot{\mathbf{x}} &= \mathbf{f}(t, \mathbf{x}, \lambda) \\ \dot{\lambda} &= -\left(\frac{\partial \mathbf{f}(\mathbf{x}, \lambda)}{\partial \mathbf{x}}\right)^T \lambda\,, \end{aligned} \tag{5.60}$$

with boundary conditions

$$\begin{pmatrix} H = 0 \\ \mathbf{x}(t_0) - \mathbf{x_0} \\ \mathbf{x}(t_f) - \mathbf{x_f} \end{pmatrix} = \mathbf{0}\,. \tag{5.61}$$

To apply numerical methods to solve this problem, the time boundaries for the BVP must be defined explicitly. However, in this case, the time interval is [0, t_f], where the end time for the BVP, t_f, is an unknown parameter. In order to overcome this problem, I redefine the system on the fixed-time interval [0, 1] by rewriting the equation in terms of a new time variable:

$$\tau = \frac{t}{t_f} \, . \tag{5.62}$$

Introducing t_f as a new state variable, the extended differential equation becomes

$$\begin{aligned} \frac{d\mathbf{x}}{d\tau} &= t_f \, \mathbf{f}(t, \mathbf{x}, \mathbf{u}) \\ \frac{d\lambda}{d\tau} &= -t_f \left(\frac{\partial \mathbf{f}(\mathbf{x}, \lambda)}{\partial \mathbf{x}} \right)^T \lambda \\ \frac{dt_f}{d\tau} &= 0 \, . \end{aligned} \tag{5.63}$$

Now the 13-dimensional BVP can be solved.

I first employed the collocation algorithm to solve the time-optimal transfer from Earth to L2. I solved the problem with a range of maximum-allowable control as shown in figure 5.12. The minimum time-of-flight as a function of maximum control is shown in figure 5.13. Position and control histories for a sample trajectory are shown in figure 5.14.

Next, I looked at the LOS realignment problem. The requirement for the re-alignment is that, at the final time, the occulter must be positioned to look at a pre-specified star with the inertial positional direction, $\hat{\mathbf{e}}$. Recall that, at different times, the position and velocity of the occulter are given as below:

$$\mathbf{r_{occ}} = \mathbf{r_{tel}} + R \, \hat{\mathbf{e}} \tag{5.64}$$

$$\mathbf{v_{occ}} = \mathbf{v_{tel}} + \omega \times R \, \hat{\mathbf{e}} \tag{5.65}$$

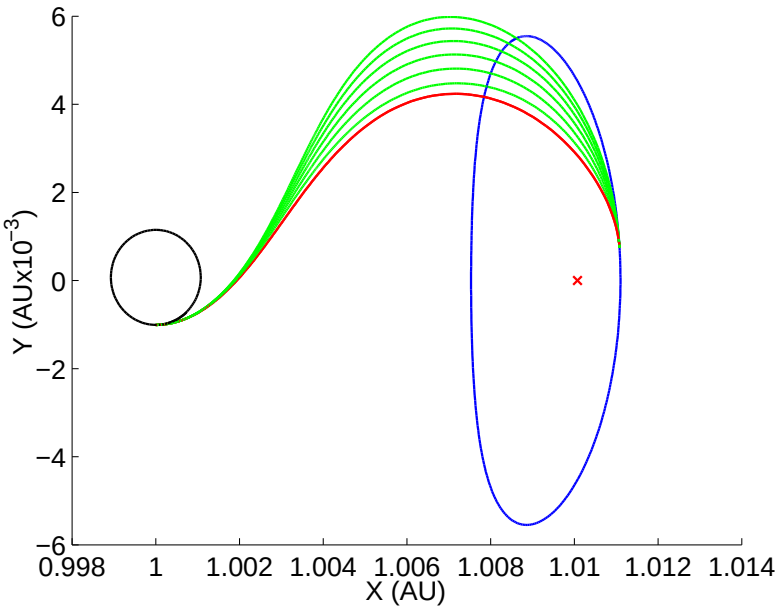

Figure 5.12: A sample of time-optimal trajectories from Earth to Halo projected on the ecliptic plane. For comparison, a 90 day minimum-energy transfer orbit is shown in red.

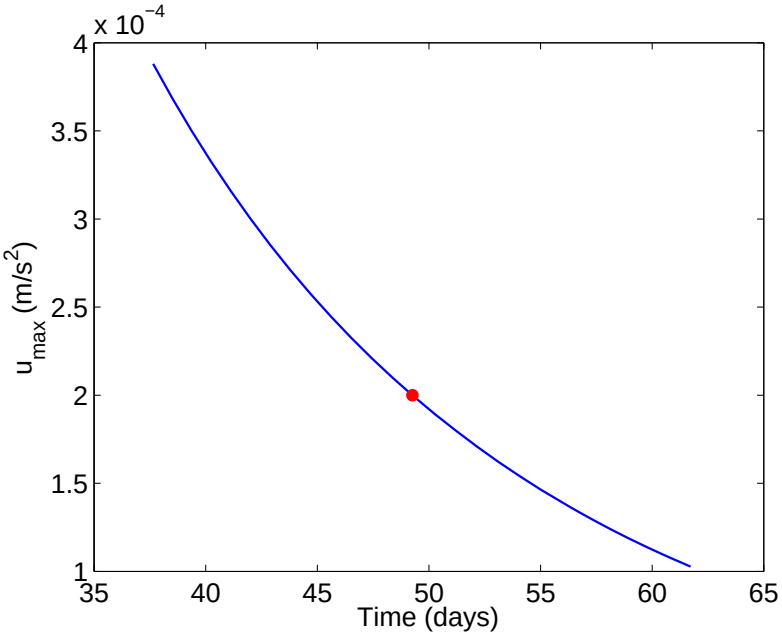

Figure 5.13: The minimum Earth to Halo transfer time for varying maximum allowable control. Red dot shows the SMART-1 spacecraft capability (0.2 mm/s).

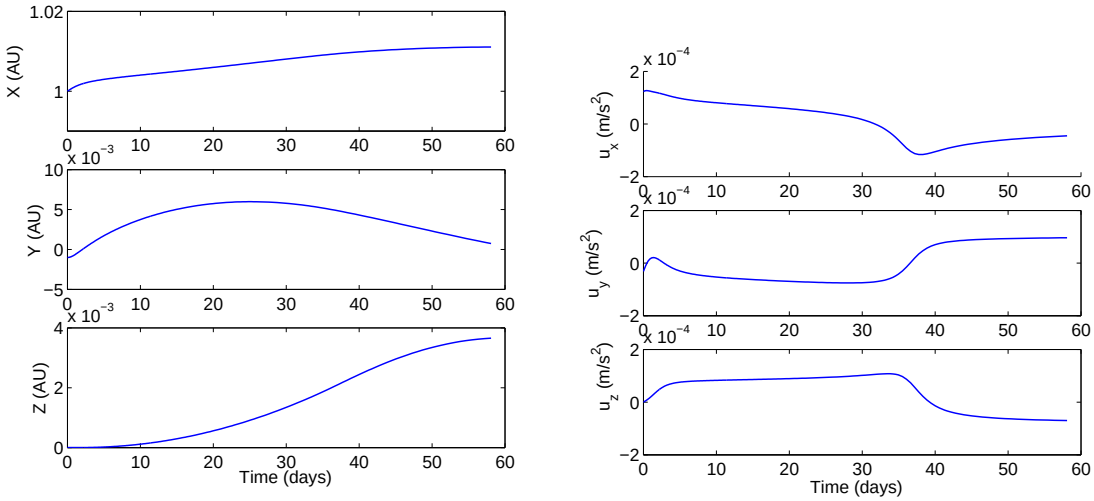

Figure 5.14: Shown on the left is the time-optimal control trajectory for the 57-day Earth to Halo transfer. The components of the control for this trajectory are shown on the right.

Thus, before knowing the time-to-go, the position of the telescope, and, as a consequence, the final position of the occulter, $\mathbf{x_f}$, cannot be specified. This problem can be solved in two ways. The first option is to change the time-independent final time constraint to

$$\psi(t_f) = \begin{pmatrix} \mathbf{r_{occ}} - (\mathbf{r_{tel}} + R\,\hat{\mathbf{e}}) \\ \mathbf{v_{occ}} - (\mathbf{v_{tel}} + \omega \times R\,\hat{\mathbf{e}}) \end{pmatrix} . \tag{5.66}$$

This changes the 13th boundary condition $H(t_f) = 0$ to

$$H(t_f) + \frac{\partial \psi(t_f)}{\partial t} = 0 . \tag{5.67}$$

However, due to the time-dependent nature of the boundary condition, it is difficult to solve this BVP. As a result, I instead used an iterated approach to solving the target-chasing minimum-time problem. In order to find the minimum-time transfer, the following procedure is followed. I first estimated the t_f and then integrated the equations of motion to find the location of the telescope and the star at that

time. From the LOS requirement, I found $\mathbf{x_f}$ and then solved the time-independent version of the problem. After obtaining the minimum time-to-go, $\mathbf{x_f}$ is calculated and the optimization is repeated with the new final position constraint. I continued iteration until the difference between the estimate and the t_f from the optimization was negligible. In this case, two to three iterations were adequate. Figure 5.15 shows the time-optimal trajectories for three scenarios and the control components for one of them.

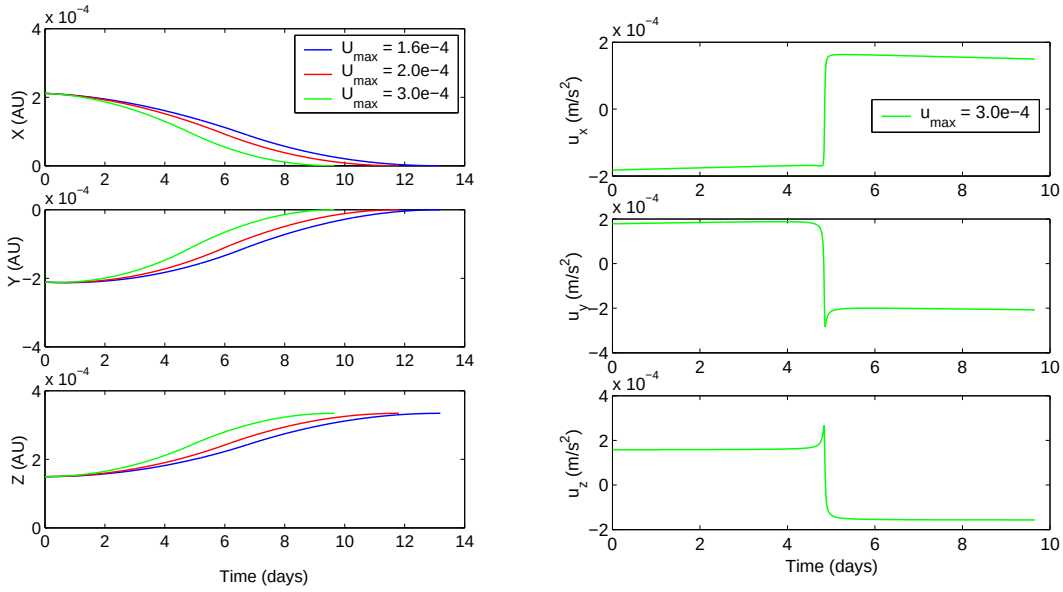

Figure 5.15: On the left is a sample of trajectories of the occulter relative to the telescope for the time-optimal control for different u_{max}. The components of the control for the green trajectory are shown on the right.

5.6 The Minimum-Fuel Optimization

In the fuel-optimal problem, the aim is to find the control history that takes the spacecraft to the predefined final position in a given time t_f while keeping the final mass $m(t_f)$ as high as possible. The mass of a spacecraft at a given time t can be

determined by the relationship

$$m(t) = m_0 - \dot{m}t\,, \tag{5.68}$$

where $\dot{m}$ is the constant propellant flow rate and m_0 is the mass of the spacecraft at the initial time. Assuming that the total change in the mass throughout the trajectory is negligible, Newton's second law of motion can be written as

$$|\mathbf{u}|\, m_0 \;\approx\; \dot{m}\, V_{ex/b}\;, \tag{5.69}$$

and it follows that

$$m(t_f) \;\approx\; m_0 - \frac{t_f\;|\mathbf{u}|}{V_{ex/b}}\;, \tag{5.70}$$

where $V_{ex/b}$ is the velocity of exhaust with respect to the body and $\mathbf{u}$ is the inertial acceleration due to spacecraft propulsion, the control input that has been used throughout this chapter. The velocity of the exhaust depends on the specifications of the spacecraft thruster.

The constant mass approximation is a very good one for the LOS realignment maneuver since such maneuvers take at most a few weeks. For the Earth-Halo transfer case, this assumption is not a very good one, but the more complicated optimization, where the dynamics of the change in mass is included in the dynamical equations, is not considered, since the Earth-Halo transfer is not the main objective of this study.

With this approximation, maximizing final mass is equivalent to minimizing the magnitude of the control throughout the trajectory. For this case, the cost function is

$$J = \int_{t_0}^{t_f} |\mathbf{u}|\; dt\;. \tag{5.71}$$

The Hamiltonian for the control problem becomes

$$H(t, \mathbf{x}, \lambda, \mathbf{u}) = |\mathbf{u}| + \lambda^T \mathbf{f}(t, \mathbf{x}) + \mathbf{p}^T \mathbf{u} \,. \tag{5.72}$$

The Pontryagin's Minimum Principle states that the optimal control is

$$\mathbf{u}^*(\mathbf{t}) = \arg \left\{ \min_{\mathbf{u}(t) \in \mathcal{U}} H(t, \mathbf{x}, \mathbf{u}, \lambda) \right\} \,. \tag{5.73}$$

Looking at the part of the Hamiltonian with control influence, I obtain

$$|\mathbf{u}^*| + \mathbf{p}^{*T} \mathbf{u}^* \leqslant |\mathbf{u}| + \mathbf{p}^{*T} \mathbf{u} \,, \tag{5.74}$$

where the superscript $\{\,^*\,\}$ denotes the optimal elements. Along with the inequality constraint $|\mathbf{u}| < u_{max}$, the optimal control is obtained as

$$\mathbf{u} = \begin{cases} \mathbf{0} & \text{if } |\mathbf{p}| < 1 \\ -u_{max} \frac{\mathbf{p}}{|\mathbf{p}|} & \text{if } |\mathbf{p}| > 1 \\ \text{Undetermined} & \text{if } |\mathbf{p}| = 1 \,. \end{cases} \tag{5.75}$$

It is important to now determine whether the undetermined case leads to singular control. Because it is very difficult to prove or disprove whether singular control exists in the nonlinear case, I therefore look at the linear case.

To prove that no singular control intervals exist for the realignment maneuver, I linearized the differential equations and obtained the linearized ODE as

$$\dot{\mathbf{x}} = A\mathbf{x} + B\mathbf{u} \,. \tag{5.76}$$

In these equations, it can be shown that A is not singular and that the controllability

matrix,

$$\mathcal{C} = [B \; AB \; A^2B \; \ldots \; A^{n-1}B] \, , \tag{5.77}$$

where n is the dimension of the system, is of full rank n. We know that, for a non-singular system with complete controllability, the system does not have singular solutions (see Kirk [68] for details). Thus, the control law for the linearized system does not have singular arcs, and is

$$\mathbf{u} = \begin{cases} \mathbf{0} & \text{if } |\mathbf{p}| < 1 \\ -u_{max} \frac{\mathbf{p}}{|\mathbf{p}|} & \text{if } |\mathbf{p}| \, . \geqslant 1 \, . \end{cases} \tag{5.78}$$

I assume that the linear analysis extends to the nonlinear case and use this control law for the realignment maneuver. Substituting for $\hat{\mathbf{u}}$ in the Euler-Lagrange equations, I obtain a 12-degree ODE in terms of the state and adjoint state only:

$$\begin{aligned} \dot{\mathbf{x}} &= \mathbf{f}(t, \mathbf{x}, \lambda) \\ \dot{\lambda} &= -\left(\frac{\partial \mathbf{f}(\mathbf{x}, \lambda)}{\partial \mathbf{x}} \right)^T \lambda \, , \end{aligned} \tag{5.79}$$

with boundary conditions

$$\begin{pmatrix} \mathbf{x}(t_0) - \mathbf{x_0} \\ \mathbf{x}(t_f) - \mathbf{x_f} \end{pmatrix} = \mathbf{0} \, . \tag{5.80}$$

For the slew from one target to another, I employed a backward shooting approach where I used the solution from the previous section as the initial guess for the adjoint variables at final time $\lambda_\mathbf{f}$. Integrating the 12-dimensional differential equation, I set

the root-finding problem as:

$$\phi(t_0 - t_f, [\mathbf{x_f}; \lambda_\mathbf{f}]) - \mathbf{x_0} = 0\,. \tag{5.81}$$

Successive iteration gives the value of the $\lambda_\mathbf{f}$ in a few iterations. Figure 5.16 shows a sample fuel-optimal trajectory, where the relative trajectory of the occulter with respect to the telescope on the Halo orbit is plotted. The bang-off-bang structure for the $J = \int |u|$ type of optimization can be seen in figure 5.16, where the magnitude and the components of the control effort for the realignment maneuver are shown.

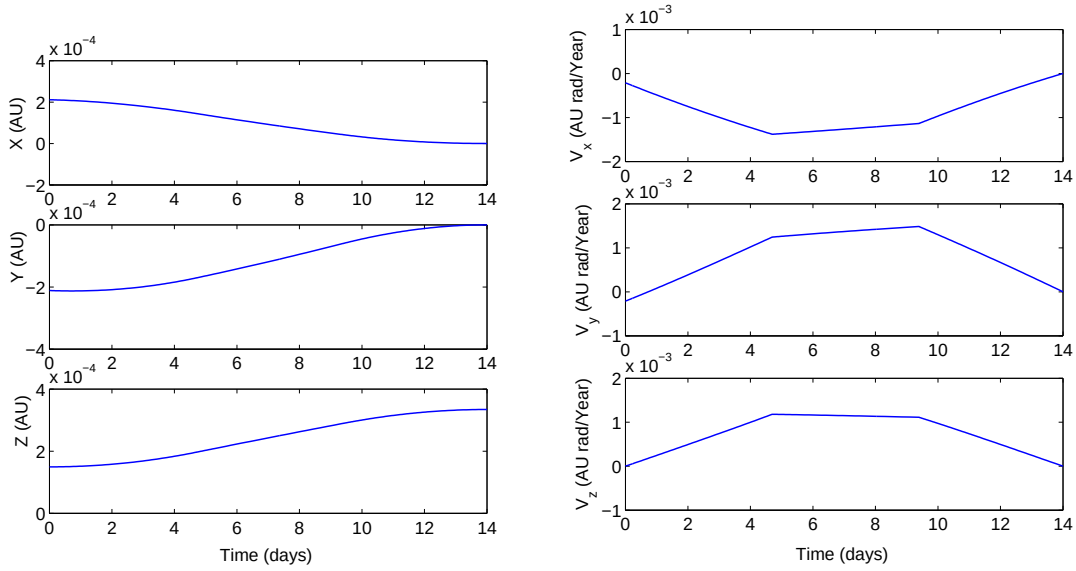

Figure 5.16: The trajectory of the occulter relative to the telescope for a minimum-fuel realignment maneuver.

Although it might be possible to prove or disprove the existence and the form of the singular control law for the Earth to Halo transfer, I did not attempt this analysis and used the direct SQP method for the numerical application where the control does not need to be specified. Collocation algorithms cannot be used for this type of problem since, as discussed before, it assumes smoothness of the state variables. However, since the control is not continuous, it follows that the velocity elements are not smooth. Figure 5.18 shows a sample optimal trajectory with the

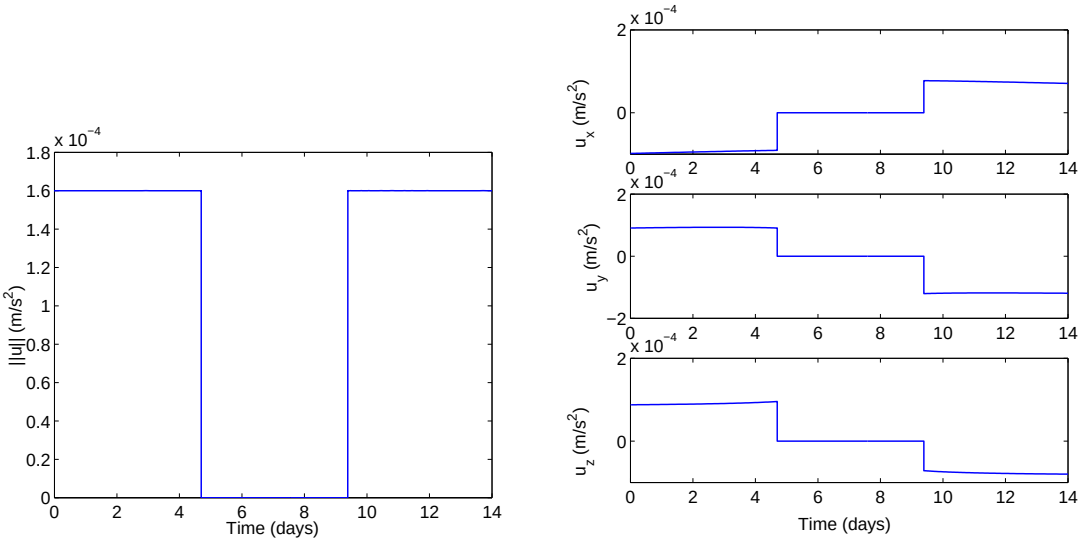

Figure 5.17: The minimum-fuel control effort for the realignment maneuver shown in figure 5.16. The magnitude of the control is shown on the left, while its components are shown on the right.

same boundary conditions that were defined in the previous sections. Figure 5.19 show the optimal control effort used for this trajectory.

5.7 Impulsive Thrust: Minimum-Fuel Optimization

Finally, I looked at the fuel-optimal impulsive control problem. The trajectories that take the occulter from one target star LOS to another with minimum fuel were studied for an impulsive thrusting system. As seen in figure 5.19, for the continuous case, the fuel-optimal solution is a bang-off-bang control. As the upper bound on $|\mathbf{u}|$ is increased, the bang-off-bang nature of the control is retained, with the thrusting phase (bang part) becoming increasingly small. In the limit, we obtain the impulsive optimal control solution where the velocity instantaneously changes at the beginning and at the end of the interval. This corresponds to an impulsive maneuver like the one that would be obtained from an impulsive chemical rocket. In this case, the

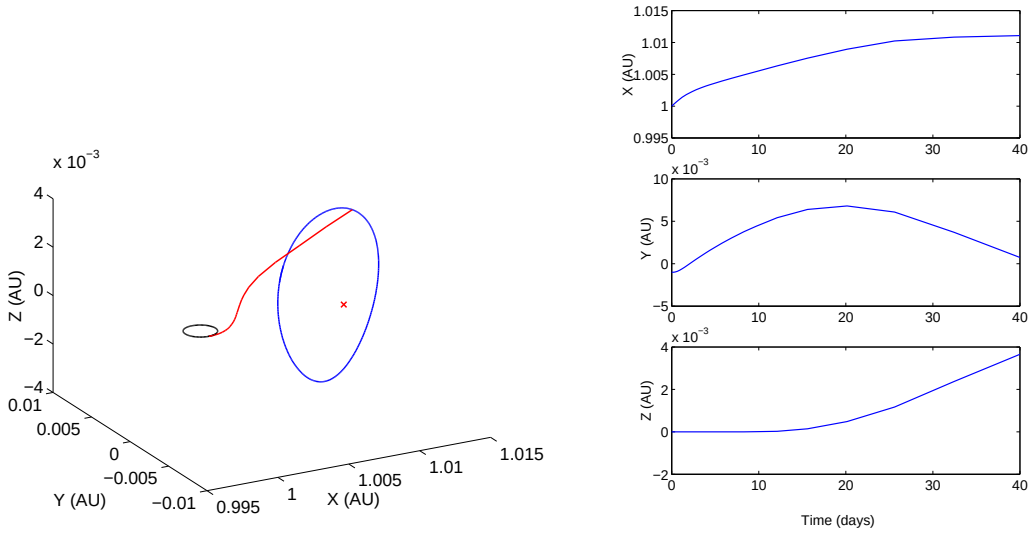

Figure 5.18: The minimum-fuel trajectory for the 90-day Earth to Halo transfer. Shown on the left, in red, is the three-dimensional trajectory. Shown on the right are the components of the position.

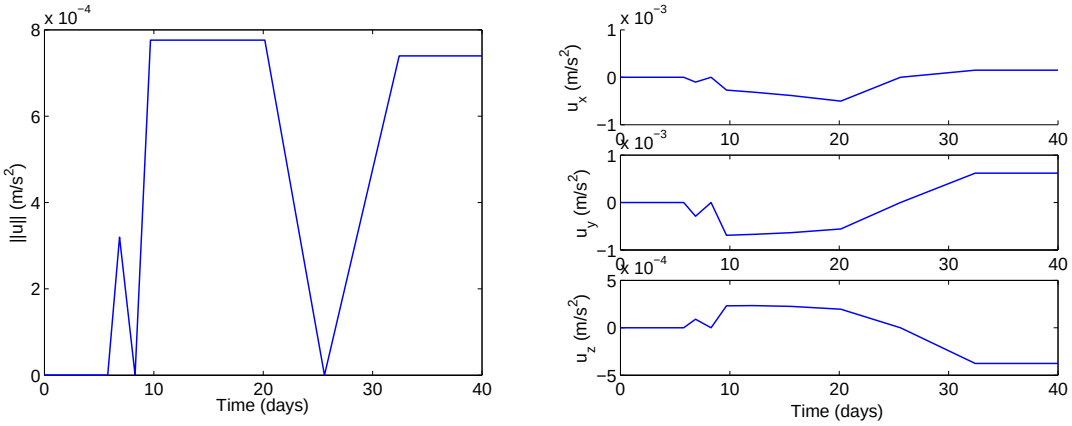

Figure 5.19: The minimum-fuel control effort for the 90-day Earth to Halo transfer. The magnitude of the control is shown on the left, while its components are shown on the right.

control consists of two large Delta-V maneuvers at the beginning and at the end of the trajectory. The control changes the velocity of the occulter while keeping its position constant. Thus, the objective is to find the velocities at the initial time, t_0, and the final time, t_f, given the initial and final positions. The Delta-V will be the difference between the computed velocity and the required velocity for planetary system observation. I write the components of the state vector as $\mathbf{x} = [x, y, z, \dot{x}, \dot{y}, \dot{z}]$. Mathematically, the problem is to solve for the 3 unknown velocities at both boundary points, a total of 6 unknowns, given the 3 known positions at both boundary points. Then, the BVP is defined by

$$\dot{\mathbf{x}} = \mathbf{f}(t, \mathbf{x}) \,, \tag{5.82}$$

with boundary conditions

$$\begin{pmatrix} x(t_0) - x_0 \\ y(t_0) - y_0 \\ z(t_0) - z_0 \\ x(t_f) - x_f \\ y(t_f) - y_f \\ z(t_f) - z_f \end{pmatrix} = \mathbf{0} \,. \tag{5.83}$$

This is a well-posed BVP which was solved by employing a collocation algorithm. Since the control consists of two Delta-V maneuvers at the beginning and at the end of the interval, the control history figures are not plotted.

5.8 Conclusion

In this chapter, the optimal trajectories for the Earth-to-L2 Halo orbit transfers and the realignment of the occulter between target star LOS's were analyzed. Employing

Euler-Lagrange, SQP, and shooting algorithms, I obtained the energy, time, and fuel optimal control for continuous thrusters and the fuel-optimal control for impulsive thrusters. The trajectories for various boundary conditions were solved. These trajectories are used in the next chapter for the global optimization of the space telescopy mission consisting of a telescope and a constellation of occulters.

Chapter 6

Global Optimization of the Mission: The Traveling Salesman Problem

In the previous chapter, the trajectory optimization for star target-to-target maneuvers was conducted, where I found the minimum Delta-V that is needed for the realignment processes. Here, the sequencing and timing of the imaging session is examined in order to globally optimize the full occulter-based telescopy mission.

This chapter aims to arrive at the algorithms that optimize the different mission scenarios from beginning to end, and that reduce the complexities of the various missions to simple graphs, where a side-by-side comparison of the advantages and disadvantages of these missions is possible. This makes possible a trade-off study, using different control strategies, in terms of cost, i.e., the total Delta-V for the mission, and scientific achievement, i.e., the number of planetary systems that are imaged.

In the first section, the results from the previous chapter are combined, and the cost of realignment as a function of mission parameters is obtained.

In the second section, a more detailed overview of the realistic mission conditions and constraints is given. It is explained how the global optimization problem can be reduced to a sorting problem that is similar to the Traveling Salesman Problem (TSP).

In the third section, the well-known Traveling Salesman Problem (TSP) is introduced. The mathematical formulation and numerical solution methods are shown, and the global optimization problem is solved based on a TSP approximation.

In the fourth section, a mathematical model for the realistic mission optimization is produced, which is akin to a Time-Dependent TSP (TDTSP).

In the fifth section, numerical methods to solve the TDTSP are discussed. These numerical methods are applied to various mission concepts with no control limitations.

In the sixth section, a feasibility study of the mission is performed by analyzing possible scenarios with the capabilities of the SMART-1 spacecraft.

Finally, the global optimization for the telescopy mission with multiple occulters is analyzed.

6.1 Realignment Cost Analysis

The optimal solution for point-to-point trajectories was obtained in the last chapter. In this section, I attempt to put these results into context. The important parameters of the system are the time-to-go, the angle between the LOS of the initial and final target stars, and the radius of the formation. In order to better understand how the optimal Delta-V depends on these parameters, I obtain the optimal trajectories using the methods from the last chapter over a wide range of parameters. These results are then averaged to give a fuller understanding of the global problem. In this section, I use only the unconstrained solutions, i.e., minimum-energy and discrete optimizations, to give general results. The case with constrained results (minimum time and minimum fuel) is studied in section 6.6 for specific u_{max}.

As the positions of the target LOS's, I choose equally-spaced points on the sphere of possible occulter locations. I do this by using the method of equal area partitioning of a sphere, which was developed by Leopardi [69]. This allows me to make sure that the whole phase space is covered with minimal computation power, since the phase space is represented by a minimum number of points. These results are then averaged over the parameters of interest.

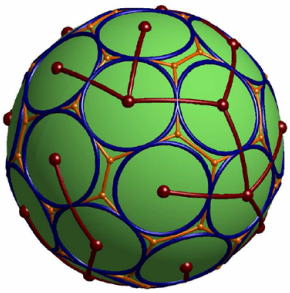

Figure 6.1: Equal partitioning of a unit sphere [69]

Using the optimization method developed above, I find the Delta-V that is needed to go between these targets at 20 equally placed locations in the Halo orbit. In figure 6.2, the Delta-V resulting from these millions of optimizations are averaged for the minimum-energy optimization, giving Delta-V as an approximate function of the radius and the LOS angle for a transfer time of 2 weeks.

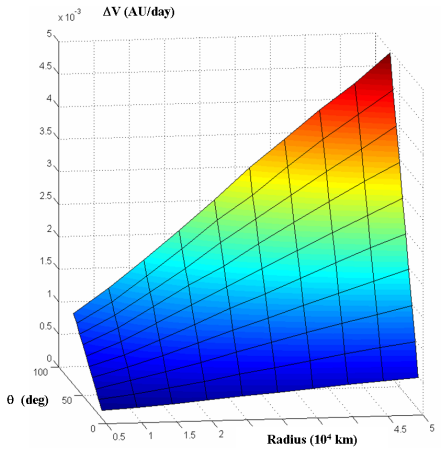

Figure 6.2: The surface of Delta-Vs as a function of distance from the telescope, and the angle between the LOS vectors of consecutively imaged stars for minimum-energy optimization ($\Delta t = 2$ weeks).

In order to make the mission analysis more realistic, the top 100 TPF-C target stars given in [59] were used. I found the Delta-V for the realignment between each target for impulsive maneuvers, as shown in figure 6.3. In the figure, the identification numbers of the stars are sorted in ascending declination.

6.2 Defining the Global Optimization Problem

Now that the relevant optimal trajectories between any two given star-imaging sessions have been found, it is important to examine the sequencing and timing of the imaging sessions, in order to minimize the global cost of the mission. This section gives an overview of the constraints that are associated with an occulter-based telescopy mission. I explain how the global optimization problem can be reduced to a

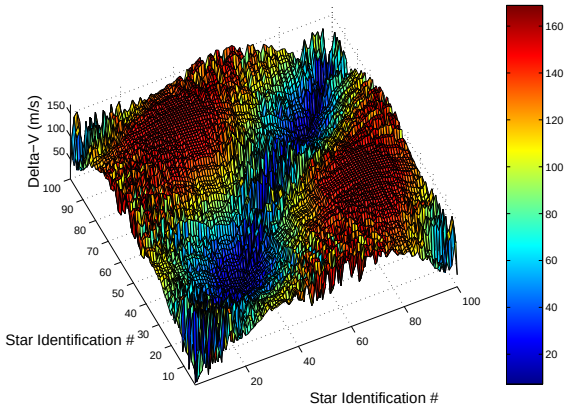

Figure 6.3: The minimum Delta-V for impulsive maneuvers needed to realign the occulter between the Top 100 TPF-C targets (Δt = 2 weeks).

sorting problem that is similar to the TSP.

The reflection of sunlight from the occulter to the telescope interferes with the imaging of the planetary system. This constrains the occulter to be between approximately 45 to 95 degrees from the Sun direction (see figure 6.4).

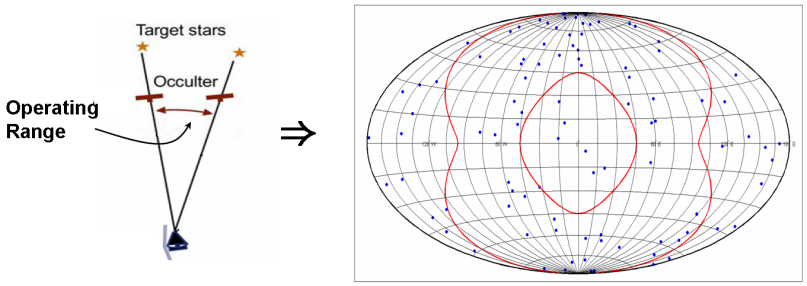

Figure 6.4: The operating range restriction of the occulter is shown on a skymap.

By including the constraints that are imposed by the telescopy requirements, the problem becomes a TDTSP with dynamical constraints (see figure 6.5). The problem reduces to finding the minimum-sum sequence that connects the rows and columns of the TDTSP matrix. The mission requirements also impose other constraints on the sequencing that are not shown in this figure. To ensure that the images of the planetary system of interest do not produce the same results, the minimum time between re-imaging of a target is 6 months. In order to conduct an approximate analysis, I

construct an example Design Reference Mission (DRM) by randomly choosing which stars are to be revisited, and how many times. While it is possible to ensure that there are no planets along the LOS, and to take into account the albedo effect of the Moon, I chose not to consider these minor constraints at this stage of optimization in order to save on computation.

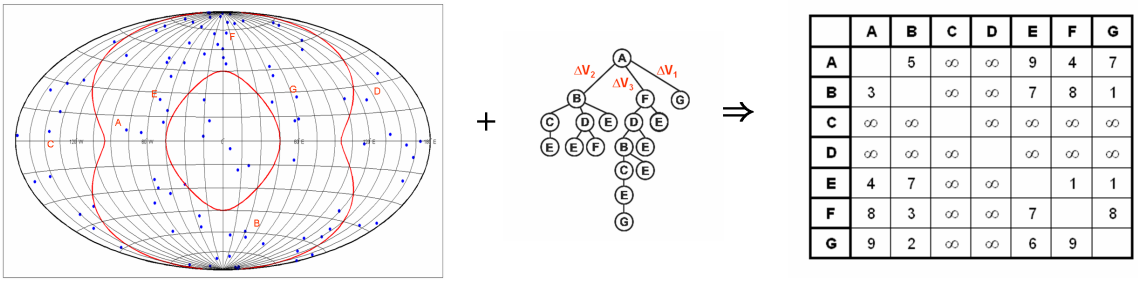

	A	B	C	D	E	F	G
A		5	∞	∞	9	4	7
B	3		∞	∞	7	8	1
C	∞	∞		∞	∞	∞	∞
D	∞	∞	∞		∞	∞	∞
E	4	7	∞	∞		1	1
F	8	3	∞	∞	7		8
G	9	2	∞	∞	6	9	

Figure 6.5: By including the constraints, the global optimization problem is converted to the search for the best ordering of target stars, where the Delta-Vs between the targets are shown on the time-dependent TSP matrix. In the figure, unaccessible zones are shown as ∞.

6.3 The Classical Traveling Salesman Problem

In the classical Traveling Salesman Problem (TSP), a salesman must visit a given number of cities, whose distances from one another are known, by the shortest possible route. The salesman's optimal path, which starts and ends in the same city, must include all cities once and only once.

Mathematically, this problem can be formulated by using a graph. The nodes and the arcs of this graph correspond to the cities and the route between cities, respectively. The TSP then becomes an assignment problem on the graph, where every node has one and only one arc leading towards it and one and only one leading

away from it. This can be expressed by employing the variable

$$x_{ij} = \begin{cases} 1 & \text{if arc(i,j) is in the tour,} \\ 0 & \text{otherwise,} \end{cases} \tag{6.1}$$

for $i = 1, 2, \ldots, n$ and $j = 1, 2, \ldots, n$, and where n is the number of cities, or in our case, stars to visit.

On this graph, the TSP becomes the arc length minimization problem given below:

$$\begin{aligned} \text{Min} \quad & \sum_{i,j} c_{ij}\, x_{ij} & & \\ \text{s. t.} \quad & \sum_{i} x_{ij} = 1 & & \forall\, j \neq i \\ & \sum_{j} x_{ij} = 1 & & \forall\, i \neq j \\ & x_{ij} \in \{0,\, 1\} & & \forall\, i,\, j\,. \end{aligned} \tag{6.2}$$

Here, c_{ij} are the elements of the cost matrix, c. Every element of this matrix represents the distance between two cities.

However, this formulation may not give the desired, single loop that connects all the nodes. Multiple, unconnected loops, or "subtours", may result. To overcome this problem, additional constraints must be added to the formulation. The Miller-Tucker-Zemlin formulation [70], which introduces new variables, u_i for $i = 1, \ldots, n$ for subtour exclusion, is one of the most well-known formulations:

$$\begin{aligned} & u_1 = 1 & & \\ & 2 \leqslant u_i \leqslant n & & \forall\, i \neq 1 \\ & u_i - u_j + 1 \leqslant (n-1)(1 - x_{ij}) & & \forall\, i \neq 1,\ \forall\, j \neq 1\,. \end{aligned} \tag{6.3}$$

The constraint formulation given in equation 6.3 is satisfied when the position of the node i in the tour is u_i.

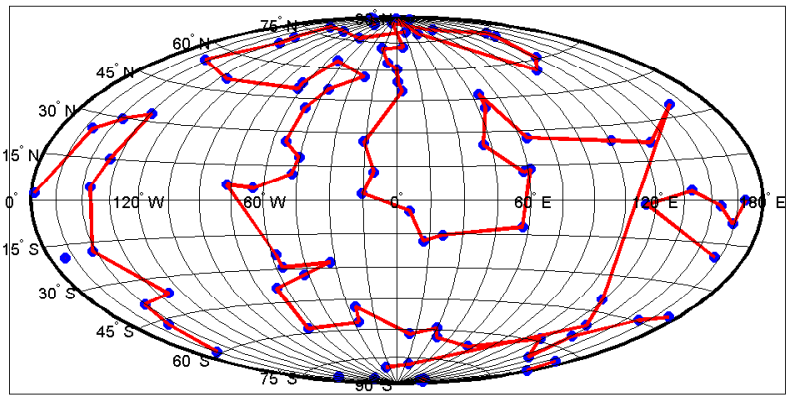

Figure 6.6: Travelling salesman solution to the top 100 TPF-C targets shown on a skymap.

While there exist exact solution methods for the TSP, such as dynamic programming, the cutting-plane method, and branch-and-bound methods, the computation time is proportional to the exponent of the number of cities. For those who are interested in exact solutions of the TSP, CONCORDE is the current state-of-the-art software [71].

When the exact optimal solution is not necessary, heuristic methods can be used, which quickly construct good, feasible solutions with high probability. These methods can find solutions for large problems consisting of millions of cities in a moderate time span, while only deviating 2-3% from the optimal solution (see Gutin and Punnen for details [72]).

Since this dissertation focuses on the analysis of the mission concept, exact solutions are not necessary at this stage. In figure 6.6, a sub-optimal solution for the TSP problem for the top 100 TPF-C targets is given. The solution was obtained using the simulated annealing method. The numerical implementation of this heuristic method is discussed in section 6.5.

6.4 Mathematical Formulation of the Global Optimization Problem

In this section, the mathematical formulation for the realignment problem is obtained, starting from the classical TSP formulation. There are four major differences between the classical TSP and the realignment problem. First, the cost matrix in our case is time dependent due to the motion of the telescope on the Halo orbit, the change in the star directions relative to the telescope, and the evolution of the exclusion zone. Second, additional constraints must be satisfied. Third, the occulter may visit some of the star targets more than once. And finally, the occulter does not have to visit all the possible star targets.

I formulate the travelling occulter problem given the following parameters: the total number of observations, N_{tot}, the identification number of the stars that can be imaged more than once, i_r, and the slew time between imaging sessions, Δt. For the sake of simplicity, I assumed that the maximum number of visits to any given star was two. The results can easily be extended to the case with more than two visits. The formulation of the problem is set such that the multiple occulter case is obtained with minimal modification of this formulation, as seen in section 6.7.

6.4.1 Cost function

First, let us define the cost function for the problem with only a single measurement for each star. The time interval between each observation, Δt, is assumed to be constant in order to simplify the problem. Then, t_i, the time when the ith target is being imaged, becomes $\Delta t\, u_i$, which is only a function of how many observations were conducted before the current target. Thus, the cost matrix that is to be minimized

can be expressed as:

$$\text{Min} \quad \sum_{i,j} c(i,j,u_i)\; x_{ij}\,. \tag{6.4}$$

In this formulation, $c(i,j,u_i)$ is a three-dimensional matrix at each time instance given with u_i, which can be precomputed.

At each time interval, the constraints, such as the stars which are non-imageable due to their location relative to the Sun, are calculated. For the stars that cannot be observed at that time, the $c(i,j,u_i)$ is set to infinity.

The sequence after the maximum visit number should not matter in the total cost computation. In order to ensure that it is excluded, the matrix elements of $c(i,j,u_i)$ for all u_i greater than the user-specified maximum number of total observations, N_{tot}, are set to zero.

$$c(i,j,u_i) = 0 \quad \text{for} \quad u_i \geqslant N_{tot} + 1 \tag{6.5}$$

Thus, the algorithm only minimizes cost for the Delta-V budget up to this value and does not take into account the remaining nodes.

6.4.2 Including the revisits into the formulation

In this section, a method to include the option of revisiting sample stars with identification numbers i_r is introduced into the formulation. As stated, I assume that the maximum number of imaging of a given star is two. Higher numbers can easily be introduced into the formulation without loss of generality.

First, I double the number of nodes such that each star now corresponds to two nodes, one for the first visit and the other for the second visit. i and j are redefined to be double the size to $i = 1, 2, \ldots, 2\,n$ and $j = 1, 2, \ldots, 2\,n$, where n is the number

stars. In this notation, elements of i and j from 1 through n represent a first visit of a target star with the identification number i or j. The elements from $n+1$ through $2\,n$ represent a second visit of a target star with the identification number $i-n$ or $j-n$. Correspondingly, I redefine the cost matrix to be double the size:

$$c(i,j,u_i) := \begin{pmatrix} c(i,j,u_i) & c(i,j,u_i) \\ c(i,j,u_i) & c(i,j,u_i) \end{pmatrix} . \tag{6.6}$$

If a star with identification number k is not allowed to be revisited, the cost for a second visit is set to infinity (or a very large number):

$$c(k+n,:,:) = \infty\,, \quad c(:,k+n,:) = \infty\,. \tag{6.7}$$

This formulation enables me to keep the TSP formulation for the x_{ij}:

$$\begin{aligned} \sum_i x_{ij} &= 1 && \forall\ j \neq i \\ \sum_j x_{ij} &= 1 && \forall\ i \neq j \\ x_{ij} &\in \{0,\,1\} && \forall\ i,\,j\,. \end{aligned} \tag{6.8}$$

The revisits, if they happen, should be after a certain amount of time. For a given star with identification number i and position in the sequence u_i, its revisit partner with position u_{i+n} should be separated by a minimum distance

$$u_i + N_{revisit} \leqslant u_{i+n}\,, \tag{6.9}$$

where n is the number of stars of interest and $N_{revisit}$ is the minimum re-imaging interval. These constraints ensure that the revisit only happens after a certain amount of time has passed. Since the time between each observation is assumed to be constant,

$t_i = \Delta t\, u_i$ is only a function of how many observations were conducted before. For example, for a realignment maneuver of two weeks, and a minimum allowable revisit time of six months, $N_{revisit} = 12$.

6.4.3 Full Formulation

The full formulation for the mathematical model can thus be written as:

$$
\begin{aligned}
\text{Min} \quad & \sum_{i,j} c(i,j,u_i)\, x_{ij} & & \\
\text{s. t.} \quad & \sum_{i} x_{ij} = 1 & & \forall\, j \neq i \\
& \sum_{j} x_{ij} = 1 & & \forall\, i \neq j \\
& u_1 = 1 & & \\
& 2 \leqslant u_i \leqslant 2n & & \forall\, i \neq 1 \\
& u_i - u_j + 1 \leqslant (2n-1)(1 - x_{ij}) & & \forall\, i \neq 1,\ \forall\, j \neq 1 \\
& u_i + N_{revisit} \leqslant u_{i+n} & & \forall\, i \\
& x_{ij} \in \{0,\, 1\} & & \forall\, i,\ \ j\,, \qquad (6.10)
\end{aligned}
$$

where c is a precalculated three-dimensional matrix. For the minimum-fuel problem, the elements of c are the Delta-V calculated in the previous sections. Without loss of generality, u_1 is set to one, which can be changed for different starting stars.

For the minimum-time optimization problem, the elements of the c matrix are the time-to-go between each target. In this case, the time spent between each realignment is no longer a constant. The cost and the constraints that are associated with the arc $i - j$ are now dependent on time t_i at position u_i.

The time at a given arc can be expressed as the sum of all the costs, or the

time-to-go, before that node:

$$t_1 = 0$$
$$t_k = \sum_{i,j} c(i,j,t_i)\, x_{ij} \quad \forall\, i \text{ s.t. } u_i = 1,\ldots,k-1 \quad \text{and} \quad \forall\, j \text{ s.t. } u_j = 2,\ldots,k \quad (6.11)$$

Here, the indices of the stars which have already been visited must first be identified from the elements of u. Then, the total time is calculated by summing all the previous time intervals. The cost function c is a continuous function of time, since the observable stars change with time while the time is dependent upon all the previous observations. This formulation is a much more complicated nonlinear programming problem.

6.5 Numerical Methods Employed for Solving the Global Optimization Problem

As discussed before, I do not implement the exact solution methods for the optimization problem. In line with the scope of this dissertation, which is the analysis of the mission concept, I use heuristic methods, which deviate only a few percent from the optimal solution, and quickly construct good, feasible solutions with high probability.

While solving the classical TSP, I implemented the tabu search [73], ant colony optimization [74], cross-entropy [75], and simulated annealing methods [76] to familiarize myself with the heuristic methods. They all performed well.

The ant colony optimization and cross-entropy methods employ a swarm of candidate solutions. These methods are not suitable for our problem, because of the existence of a high level of constraints. As far as the cross-entropy method is concerned, one infeasible solution in a group would bring the statistical average of the group up, but trying to impose the constraints on the elements is against the spirit

of the swarms of trials and averaging. As for the ant colony optimization, it is not apparent how the constraint can be imposed that prevents the same star from being revisited before a certain amount of time.

I chose to use simulated annealing rather than a tabu search, since, due to the constraints, the optimal solution and initial feed might be in separated parts of the search space, and random motion given in simulated annealing might be of use to get out of local minima.

Next, I explain the implementation of simulated annealing for the problem at hand.

6.5.1 Simulated annealing

Developed by Kirkpatrick et al. [76], simulated annealing is a global optimization method suitable for problems with a large search space. The method is inspired by the way crystalline structures are formed in the thermal annealing process, such as the production of high-strength steel.

The analogy between the physical annealing process and the numerical optimization is such that the temperature change is akin to the time spent in the optimization, and the energy level is analogous to the cost function to be minimized. Similarly to the physics of atoms under the annealing process, simulated annealing generates random solutions in the neighborhood of the old one. Initially, when the temperature is high (the initial stages of optimization), random moves which lead to higher energy (higher cost) levels are allowed frequently, but as the system cools down (optimization time increases), the tendency to allow moves which increase the energy is reduced. The algorithm becomes more like a downhill search method.

Algorithm Pseudo-Code

Below is the pseudo-code for the simulated annealing algorithm used in the global optimization problem.

```
input: X0, Tmin, kappa
    energy = cost(X0);
    X = X0;
    while{ T > Tmin
        X_new = neighbor(X);
        energy_new = cost(X);
        delta = energy - energy_new;
        if (delta > 0) or (exp(delta/T) > random())
            X = X_new;
            energy = energy_new;
            T = T*kappa;
        end }
output: X, energy
```

Here, X is a vector which contains the visiting sequence of each star (and visiting partners, if they exist). Temperature is represented by T, the freezing temperature by Tmin and the cooling constant by kappa. Three functions are used in the algorithm; random() is a uniform-distribution random number generator in the interval (0, 1); cost is the cost function for a given visiting sequence; and neighbor is a function which generates random visiting strings in the neighborhood of X.

For the constants in the algorithm, a cooling constant of $\sim$0.99 and initial temperatures in the range of 10-40 degrees gave good results. I set the freezing temperature to be one degree.

As for the functions, I used the cost function defined in the previous sections. This cost function can be rewritten in terms of X, the visiting sequence vector, as

$$\min \sum_{k} c(X(k), X(k+1), k)\,. \tag{6.12}$$

For the neighbor function, I considered different options . The choice of the neighbor function is of critical importance for the success of the simulated annealing process. This is discussed in more detail in the next section.

Choosing the neighbor function

The neighbor function is an operator that converts one tour into another by using exchanges or moves of the sequence vector. This function defines an associated neighborhood for each tour that can be obtained with a single function operation. Incremental improvements in the cost function are obtained by continually moving from one neighbor to a better one, with a lower cost. This is done by repeated use of the neighbor function. Finally, the optimal solution is obtained when there are no better neighbors left. The 2-Opt operation is the most famous and tested of the simple neighbor operator functions. The 2-Opt operator removes two edges and replaces these with two different edges that reconnect the fragments in the reverse order. The illustration of this operation is shown in figure 6.7.

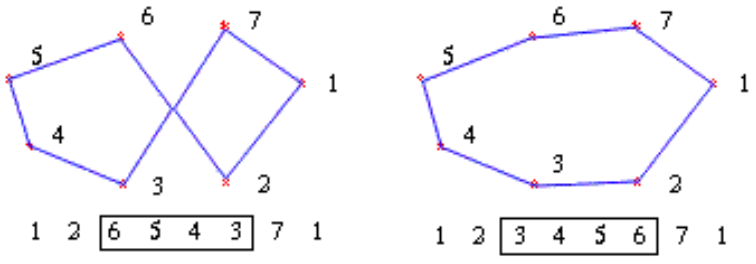

Figure 6.7: Illustration of the 2-Opt move [77].

2-Opt was the first method of choice, but it failed to give good results. Due

to the high number of constraints involved in our problem, a constraint was broken almost every time when a part of the sequence was reversed. I decided not to use this operator.

Consider that, as the simulated annealing proceeds, the energy of the state will be lower than that of a random state. Thus, if the neighbor function results in arbitrary states, these moves will all be rejected after a few steps. Therefore, in simulated annealing, the neighbor function should be chosen such that the neighbors and the current tour have similar energy levels. As a result, I opted for an operation where I swapped the two consecutive stars, swap (X(k), X(k+1)), rather than arbitrary stars.

Additionally, if the operator does not obey the constraints by default, many fruitless trials result. I avoided this by choosing the initial guess to satisfy all the constraints, and by making sure that all the neighbor perpetration satisfy the constraint. When swapping the stars in consecutive positions, I checked whether the swap operation leads to a minimum distance between the pair partners, a star and its revisit partner, of less than $N_{revisit}$. If so, the swap is not performed and another random k is chosen to swap (X(k), X(k+1)). This ensures that, as long as the initial sequence obeys the minimum separation between pairs of less than $N_{revisit}$, the neighbor will also obey this constraint. By not breaking any constraints, the algorithm is able to move through the neighborhood quickly.

However, the neighbor function should be able to reach every possible state of the system, and the swapping that is described above may not ensure this property, because it is done in pairs. To overcome this problem, I used three more operators that enlarge the neighborhood sufficiently to avoid getting stuck in local minima. These are the following operators:

1. Swap random star pairs: Two random pairs, $\{i, i+n\}$ and $\{j, j+n\}$, two stars and their revisit partners, are swapped, swap (X($\{u_i$,$u_{i+n}\}$), X($\{u_j$,$u_{j+n}\}$)).

2. Mutate random star pairs (1): Two random pairs, $\{i, i+n\}$ and $\{j, j+n\}$,

are mutated such that the locations of i and j are swapped. If the resultant sequence gives rise to a minimum distance between the pairs that is less than $N_{revisit}$, the swap is not performed and another random pair is chosen.

3. Mutate random star pairs (2): Two random pairs, $\{i, i+n\}$ and $\{j, j+n\}$, are mutated such that the location of stars $i+n$ and $j+n$ are swapped. If the resultant sequence gives rise to a minimum distance between the pairs that is less than $N_{revisit}$, the swap is not performed and another random pair is chosen.

I used these operators less frequently than the consecutive pair swaps, for a total of 10% of the time for each operator as opposed to 70% for the swapping of the consecutive pairs, in order to allow a fast and efficient local search.

6.5.2 Branching for time-optimal case

In the time-optimal case, the fact that the cost function cannot be obtained beforehand complicates the employment of the annealing method. More importantly, the constraints are no longer known beforehand, and instead change with each neighbor operator. As a result, I used a branching algorithm, where the constraints are dealt with as they arise.

Here, all the possible moves from a given initial star location are considered. Each move is the first element of a possible visiting sequence. From all these sequences, all the possible second elements are considered, and the algorithm proceeds in this manner. This leads to an exponential amount of possible sequences to be tried and stored, which is not practical. Thus, after every stage, an elimination of some of the sequences is necessary. There are many possible approaches to this selection. While the most obvious approach is to eliminate the sequences with the highest cost, these high-cost sequences may in the later stages lead to better results, and thus a diversification, as in the simulated annealing case, can be used. I experimented with

some diversification methods, which did not lead to better results. As a result, I used only the criterion of cost.

When, in the end, the sequence length reaches the total imaging sessions, the list element with the lowest cost is taken as the optimal solution. Unfortunately, this algorithm will lead to local minima, but the solution of the full problem is prohibitively difficult to obtain. The advantage of this algorithm is that the constraints of Sun avoidance, minimum revisit time, and no revisit after two visits, are satisfied in the final solution with minimal computational effort.

6.5.3 Results

The global optimal solutions for a few representative cases are shown in this section. I use only the unconstrained solutions, i.e., the minimum-energy and discrete optimizations, in order to give general results. The case with constrained results (minimum time and minimum fuel) is studied in section 6.6 for specific u_{max}.

A sample solution to the global optimization problem with no revisits and 75 imaging sessions is shown in figure 6.8, where the minimum-energy control law was used.

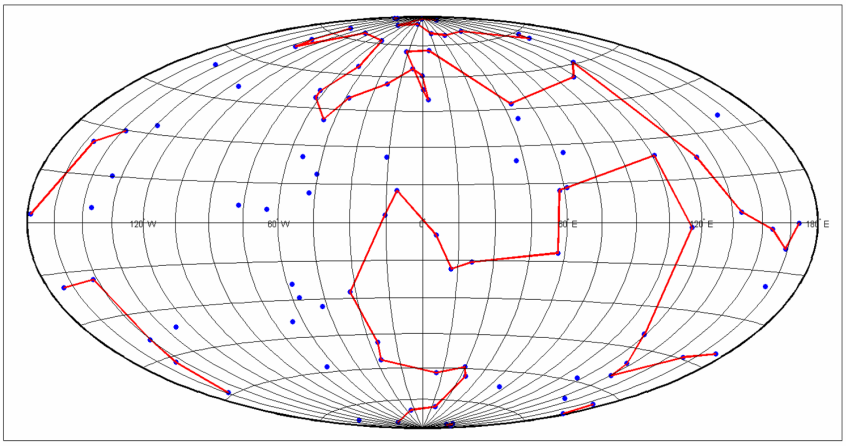

Figure 6.8: The global optimal solution to the single occulter case, with 75 imaging sessions of the Top 100 TPF-C stars, and 2 weeks' flight time between targets and no revisits.

Figure 6.9 shows a sample solution to the global optimization problem for 110 imaging sessions with maximum two visits, where the 50 stars that can be revisited with minimum 6 months' delay were chosen at random, and discrete optimal control was used.

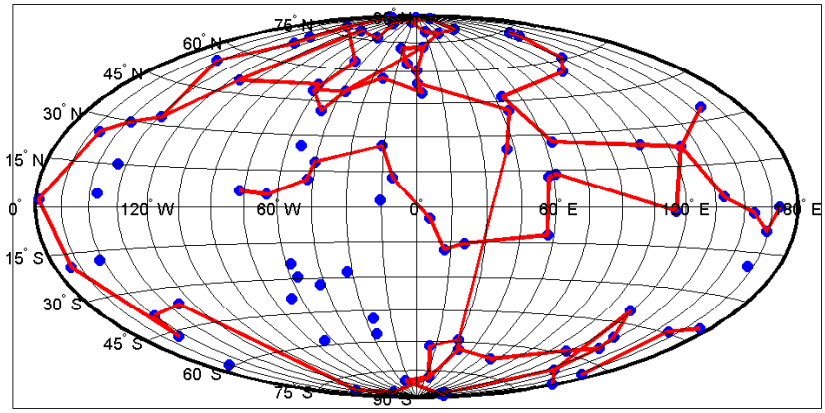

Figure 6.9: The global optimal solution for 110 imaging sessions of the top 100 TPF-C stars, for the single occulter, with 2 weeks' flight time between targets and 50 randomly chosen stars that can be visited twice.

The algorithms developed so far enable us to find the total minimal-cost requirement for a given mission. Figure 6.10 shows the averaged Delta-V obtained for the TPF-C top 100 stars for minimum-energy optimization, where the 50 stars that can be revisited with minimum 6 months' delay were chosen at random. The global optimal solutions for the optimal control for impulsive case with the same requirements are shown in figure 6.11. As seen from these figures, the case that is energy optimal requires more Delta-V than the impulsive maneuver case. This is due to the fact that energy-optimal control minimizes the square of the control effort rather than the control, i.e., the Delta-V, effort, while the impulsive maneuver is the limit that the minimum-fuel trajectories reach as the bound of the maximum acceleration, u_{max}, is increased to infinity. Since the impulsive maneuver uses unbounded control as opposed to the minimum-fuel solutions, the Delta-V requirement will be lower. Thus, the Delta-V for impulsive solutions can be thought of as the lower bound for a given

mission scenario, making it smaller than both minimum-fuel with bounded control input and minimum-energy control.

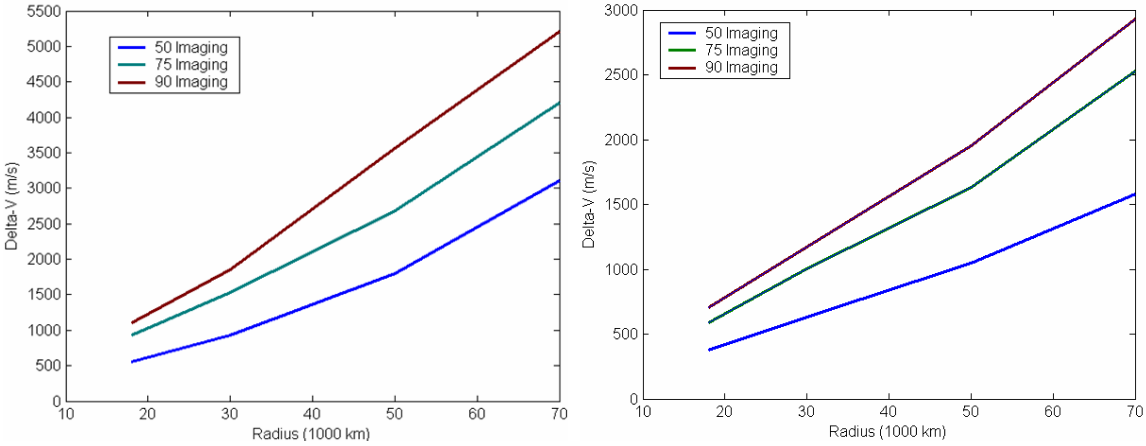

Figure 6.10: The global Delta-V curves for the single occulter mission with energy-optimal control (Left: $\Delta t = 1$ week, Right: $\Delta t = 2$ weeks).

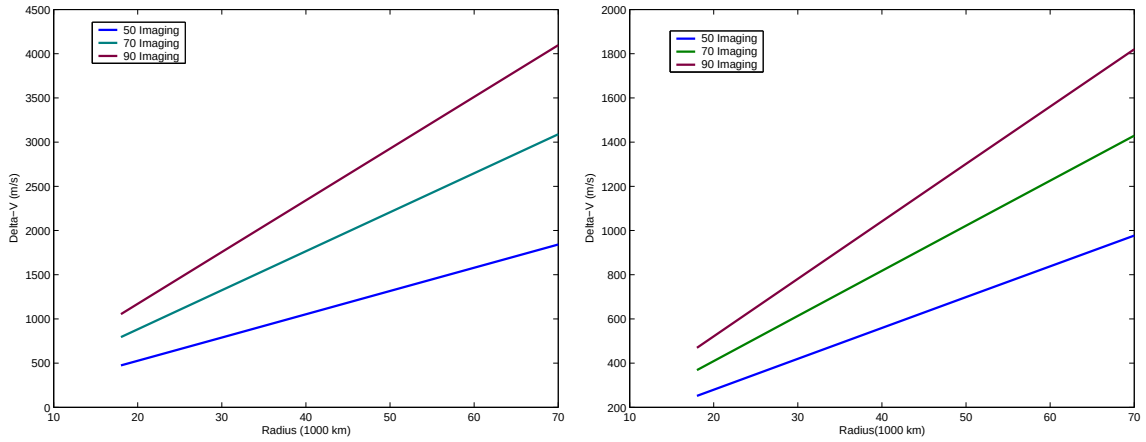

Figure 6.11: The global minimum Delta-V curves for the single occulter mission with impulsive control (Left: $\Delta t = 1$ week, Right: $\Delta t = 2$ weeks).

In order to understand the thrust capability that is needed for a given spacecraft, it is important to know the maximum thrust and acceleration it has to perform in flight. Table 6.1 shows that the maximum acceleration needed for energy-optimal control increases as the radius of the formation does. Here, the thrust is obtained by multiplying the acceleration requirements with the mass of the SMART-1 spacecraft that is discussed in the next section.

Table 6.1: Maximum thrust needed for the minimum-energy control effort solutions with a Δt of 2 weeks, obtained in figure 6.10.

Radius	Max Thrust
18,000 km	18 mN ($\sim$ 0.05 mm/s^2)
30,000 km	31 mN ($\sim$ 0.10 mm/s^2)
50,000 km	52 mN ($\sim$ 0.15 mm/s^2)
70,000 km	70 mN ($\sim$ 0.2 mm/s^2)

6.6 Performance of SMART-1 as an Occulter

For a concrete understanding of the feasibility of the mission, the performance of a sample spacecraft, SMART-1, as an occulter is analyzed. Designed by ESA to test continuous solar-powered ion thrusters, SMART-1 successfully left the gravitational field of Earth and reached the mission objective of impacting the Moon [78]. SMART-1 was chosen for a feasibility test because its solar-powered Hall-effect thrusters may be good candidates for the occulter-based telescopy mission under study. For this feasibility study, I used the top 100 TPF-C targets and the exact specifications of the SMART-1 spacecraft, given in table 6.2.

Table 6.2: Specifications of the SMART-1 spacecraft

Maximum Thrust	68 mN
Mass Ratio	0.83
Propellant Mass	80 kg
Total Delta-V	3600 m/s
Isp	1640 s
Maximum Acceleration	0.2 mm/s^2
Full Thrust Life Time	210 days

First, the minimum realignment time between targets was obtained. An example minimum-time surface is shown in figure 6.12.

The minimum-time charts were employed to find the targets which can be reached within a given time span. Then, minimum-fuel trajectories were obtained for these feasible targets. An example minimum-fuel surface is shown in figure 6.13. For the

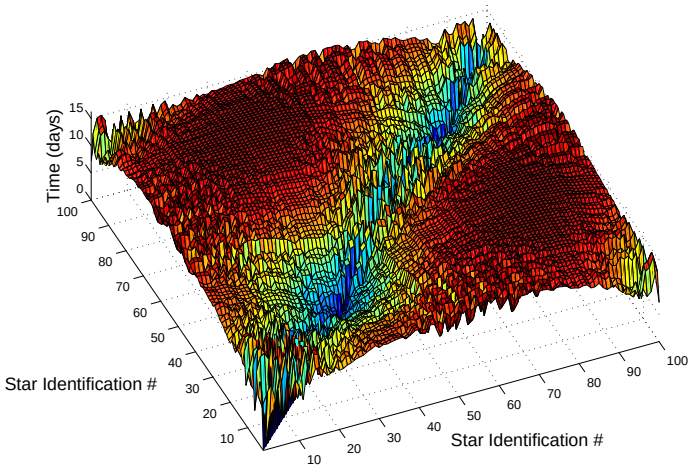

Figure 6.12: Minimum time-to-realign between top 100 TPF-C targets with SMART-1 capibilities (R=50,000 km).

sake of reasonable display, the unreachable targets are shown with a Delta-V of zero as opposed to infinity. Thus, the two regions in the lower left and upper right corners, shown in dark blue, represent targets which cannot be reached within 2 weeks.

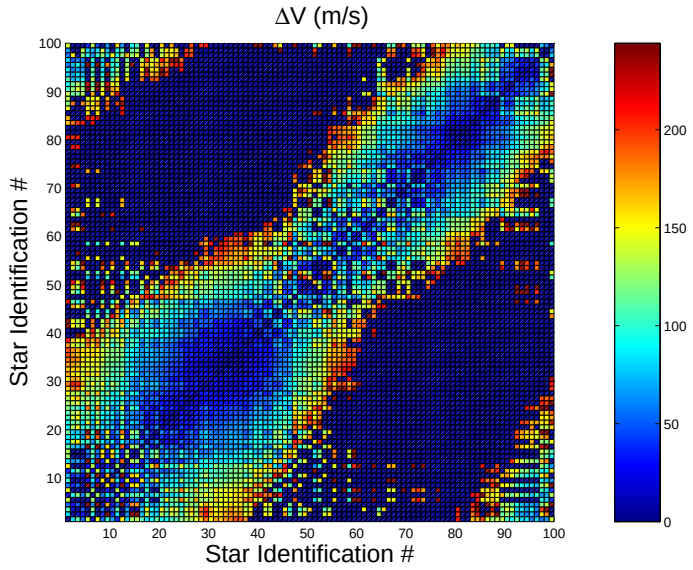

Figure 6.13: Delta-V to realignment between top 100 TPF-C targets with SMART-1 capibilities (R=50,000 km and Δt=2 weeks).

Now, I look at a feasibility study, where the mission is constrained to use the SMART-1 spacecraft with all its limitations, including the fuel on board and maxi-

mum thrust. I assume that the spacecraft continues imaging until the fuel is depleted. Figure 6.14 shows the results that would be obtained if a minimum-fuel strategy were employed. Since the fuel on board is limited, a more spendthrift fast slew approach, where the time between the imaging sessions is decreased, leads to a decrease in the total number of observations. The last data points at 20,000 km for 1 week and 70,000 km for 2 weeks are very restrictive, since they give very few options for consecutive targets. As a result, they do not provide the flexibility that is needed in a real-life mission.

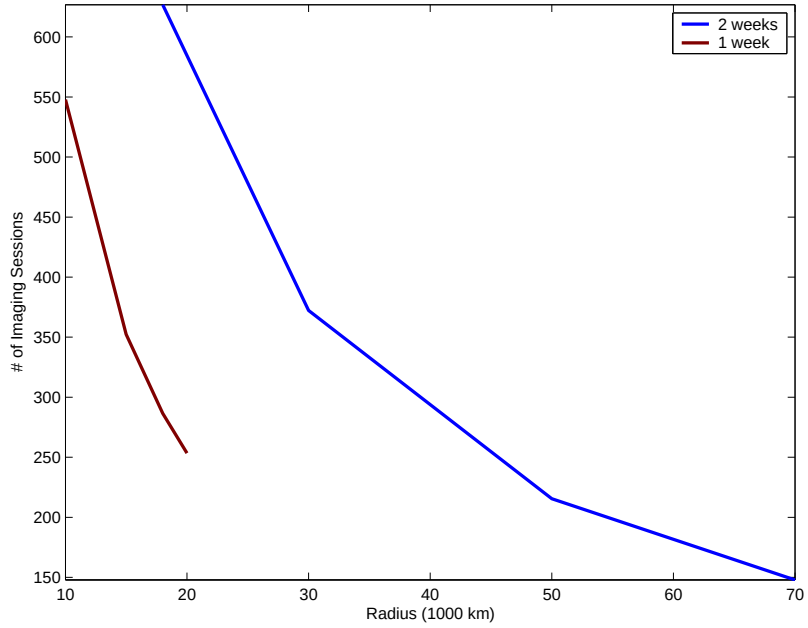

Figure 6.14: The total number of imaging sessions versus the radius, for the fuel-optimal control case (with SMART-1 capabilities).

Figure 6.15 shows the results that would be obtained if a minimum-time transfer strategy were employed. This figure shows that, as the radius of the formation increases, the total number of imaging sessions decreases. When this is compared with figure 6.14, it is apparent that the minimum-time strategy trades off the speed of observations against the total number of observations.

Even though the results from figures 6.14 and 6.15 should be treated as the optimistic upper bounds for the number of possible imaging sessions, it is apparent that,

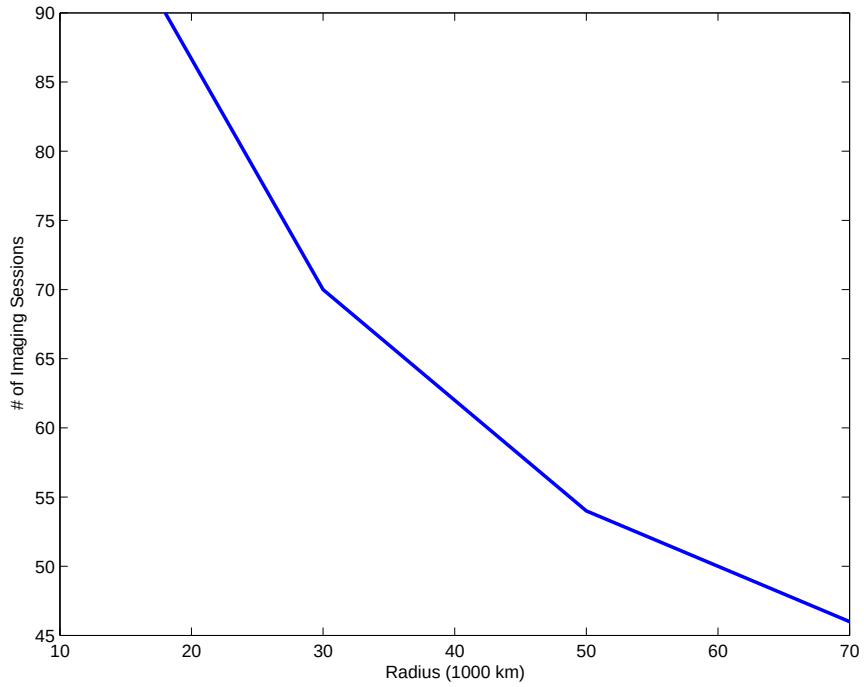

Figure 6.15: The total number of imaging sessions versus the radius, for the time-optimal control case (with SMART-1 capabilities).

notwithstanding the difficulties, the mission is within reach of the current technology. The Delta-V requirements for the occulter are reasonable. With the next generation of thrusters, it should be possible to maneuver the approximately 60-meter diameter occulter to do sufficient imaging to be able to find Earth-like planets.

6.7 Multiple Occulters

Having solved the single occulter problem, I study the best configuration of the constellation consisting of multiple occulters. The use of multiple occulters has several advantages [79]. First, as the number of occulters increases, so does the target observation rate. Second, the mass of each occulter can be reduced with a multiple occulter approach. Third, the lifetime of the mission can be increased. Finally, the redundancy in the system design would guard against the loss of the whole mission in case of a failure in one of the occulters.

I consider two approaches to the multiple occulter formation, in the first, the occulters are placed on fuel-free Quasi-Halo orbits around the telescope's Halo orbit. This method is discussed in the first section. In the other approach, the global optimization problem is formulated as in the single occulter case, and it is solved using simulated annealing. This method is explored in the later sections and results are shown. The single and the multiple occulter approaches are compared in light of these results.

6.7.1 Multiple Occulters on Quasi-Halo Orbits

First, I consider the approach where multiple occulters are placed on Quasi-Halo orbits around the base Halo orbit. The optimal placement problem then becomes an optimization of the $3 \times N$ parameters that uniquely define N Quasi-Halo orbits, namely the size and the two-phase angles (R, θ_1, θ_2) of all the occulters, such that, in the absence of any control, the occulters' trajectories come close to intersecting the maximum number of star LOS within a given time span. This is achieved by first choosing points in the (R, θ_1, θ_2) space that define the Quasi-Halos found in the second section, and then integrating these forward in time (See Figure 6.16). The relative motion of these orbits with respect to the base Halo orbit is transformed to inertial coordinates; an easily reachable region, such as +5, -5 degrees from the path, is then defined; and the number of targets that would be enclosed in this region is found. The $3 \times N$ parameters that give the highest number of targets in the union are taken to be the best initial guess for the formation.

These ideas were implemented by Princeton mechanical and aerospace engineering student Azuka Chikwendu in his undergraduate thesis [80]. Looking at spacecraft placed on multiple Quasi-Halo orbits, he showed that the two-occulter mission decreases the Delta-V drastically, while the addition of a third occulter is of less value for the mission. As an example from his work, the best set of three quasi-halo orbits

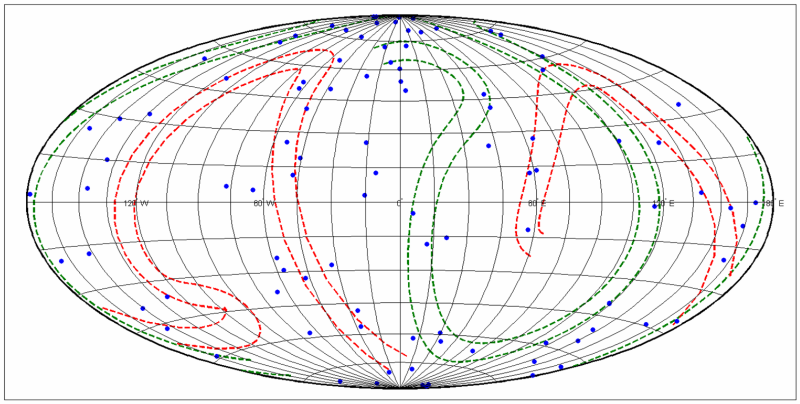

Figure 6.16: Skyplot of the areas of the sky which are easily accessible by two different Quasi-Halo orbits.

with 70,000 km radius around the halo orbit is shown in figure 6.17, which plots the star coverage that would be achieved by these orbits for half of the five-year mission.

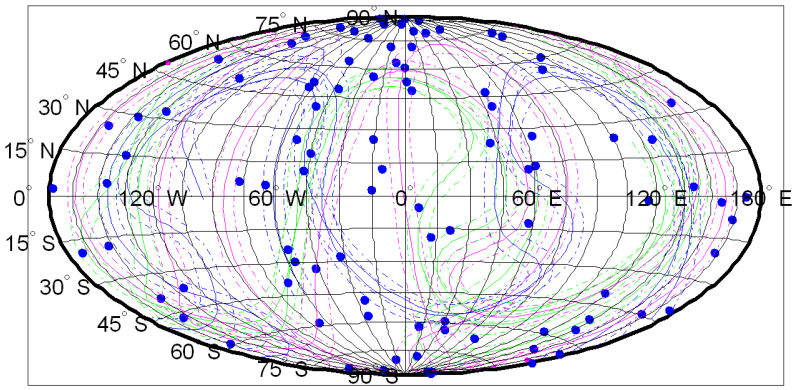

Figure 6.17: Ideal three-occulter mission, shown for 5 orbital periods, with 5 degree range indicated [80].

6.7.2 Global Optimization with Constraints

In this section, the global optimization problem is formulated as in the single occulter case, and it is solved using simulated annealing.

Mathematical Model

The full formulation for the mathematical model for the case with two occulters, maximum two visits and no revisit of the same star with the same occulter, can be written as:

$$
\begin{aligned}
\text{Min} \quad & \sum_{i,j} c(i,j,u_i)\, x_{ij} + c(i,j,v_i)\, y_{ij} \\
\text{s. t.} \quad & \sum_{i} x_{ij} = 1, \quad \sum_{i} y_{ij} = 1 && \forall\, j \neq i \\
& \sum_{j} x_{ij} = 1, \quad \sum_{j} y_{ij} = 1 && \forall\, i \neq j \\
& x_{ij} \in \{0,\, 1\}, \quad y_{ij} \in \{0,\, 1\} && \forall\, i,\ j \\
& u_1 = 1, \quad v_1 = 1 \\
& 2 \leqslant u_i \leqslant n, \quad 2 \leqslant v_i \leqslant n && \forall\, i \neq 1 \\
& u_i - u_j + 1 \leqslant (n-1)(1 - x_{ij}), \quad v_i - v_j + 1 \leqslant (n-1)(1 - y_{ij}) && \forall\, i \neq 1,\ j \neq 1 \\
& N_{revisit} \leqslant abs(v_i - u_i) && \forall\, i\,, \qquad (6.13)
\end{aligned}
$$

where x_{ij} and y_{ij} are 1 if arc(i,j) is in the tour of the first and second occulter, respectively, and u_i and v_i are the positions of the ith target in the first and second occulters tour. The cost matrix, c, is the same as in the single occulter case. Without loss of generality, u_1 and v_1 can be set to different starting target stars. The more complicated case, where the same occulter is allowed to image the same star more than once, is not included in this dissertation.

Numerical Method: Simulated Annealing

I proceed as in the single occulter case, using simulated annealing to this time solve the two-occulter global optimization. The results can be easily extended for formations with more than two occulters.

First, I define X, the vector which contains the visiting sequence of each star, as well as the visiting partner, if they exist. However, this time, X includes the sequence for two occulters. The odd elements of X refer to the identification number of the star that is being imaged at that time by the first occulter, and the even elements refer to that of the second occulter. The time interval between each imaging is fixed. The telescope first images star X(1) using the first occulter. After time Δt, it images star X(2) using the second occulter, and then, after Δt, it images star X(3) using the first occulter, and so on.

For the constants in the algorithm, a cooling constant of ∼0.99-0.999 and an initial temperature of approximately 100 degrees gave good results. I set the freezing temperature to be one degree.

I used the same three-dimensional cost matrix, c, as is in the single occulter simulated annealing algorithm. As for the functions, since even and odd elements of X, the visiting sequence vector, define different occulters, the cost for the total mission is the summation of the cost for each occulter. This can be expressed as

$$\min \sum_{k} c(X(k), X(k+2), k)\,. \tag{6.14}$$

Here, for summation over odd values of i, the cost associated with the first occulter is obtained, while for summation over even values of i, the cost associated with the second occulter is found.

I used the same neighbor function as in the single occulter case. The random swap and mutations are kept the same, with the single difference that the swapping of the consecutive imaging sessions is now equivalent to swap(X(k), X(k+2)) instead of swap(X(k), X(k+1)).

Results

I applied the simulated annealing method to the multiple occulter case. Figure 6.18 shows the optimal solution trajectory for a mission scenario consisting of two occulters with 20,000 km radius separation from the telescope, and where no revisiting is allowed with 1 week flight time.

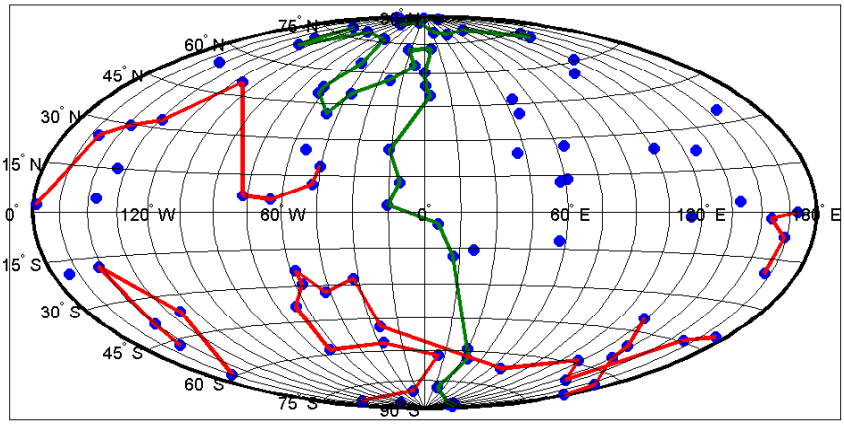

Figure 6.18: The global optimal solution to the two-occulter formation, for 80 imaging sessions of the top 100 TPF-C stars, with Δt of 1 week and no revisiting.

In the simulated annealing process, as in the formation of crystals, the optimal solution is obtained slowly by random moves. Figure 6.19 shows how the annealing process is performed. As the temperature is decreased slowly, Delta-V decreases, and the optimal solution is obtained.

The global optimal solution to a two-occulter formation is shown in figure 6.20. The occulters are placed at 20,000 km radius separation from the telescope, and they perform 110 imaging sessions of the top 100 TPF-C stars, in a 1-week flight time between targets (each occulter takes 2 weeks to move from a target to another target but the Δt between imaging sessions for the telescope is 1 week) and randomly chosen revisitable stars. For comparison, the single-occulter global optimal solution for the same scenario with 2 weeks' flight time is given in figure 6.9.

However, in order to obtain the same scientific achievement in a given mission

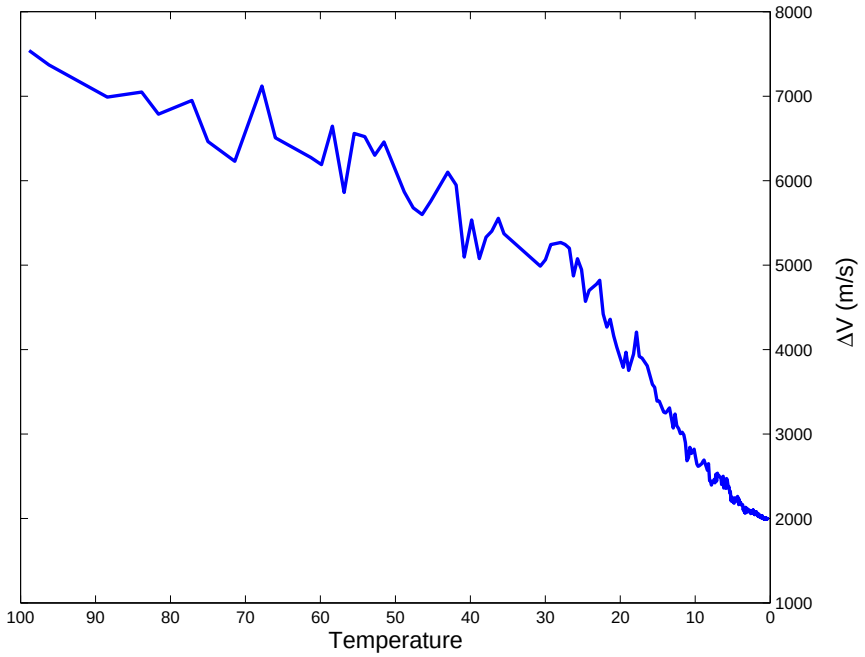

Figure 6.19: The change in Delta-V as the temperature decreases in the simulated annealing, for the optimization shown in figure 6.20.

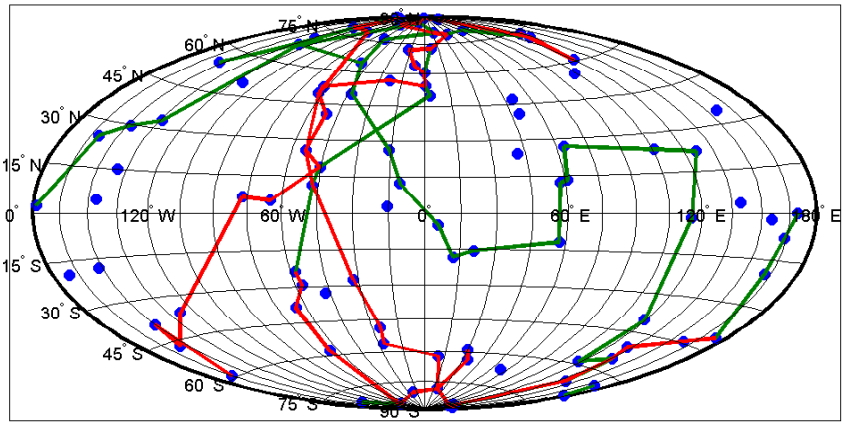

Figure 6.20: The global optimal solution to the two-occulter formation, for 110 imaging sessions of the top 100 TPF-C stars, with Δt of 1 week and 50 randomly chosen revisitable stars.

lifetime, a single-occulter mission must reduce the Δt to 1 week to make up for the lack of a second occulter. The single-occulter mission for this specific case has a Delta-V cost of 3800 m/s, while the two-occulter mission has a Delta-V requirement of 2000 m/s. This reduction in Delta-V due to the use of multiple spacecraft becomes roughly equivalent to the reduction in Delta-V that would be achieved if the flight time of

a single spacecraft mission were doubled. This is roughly equivalent to halving the Delta-V cost; the fact that the occulters can take twice as long for the slews reduces the Delta-V cost by half. Since this holds true generally, for all cases, I do not provide further charts of the global optimal solution for the multiple occulter case.

Conclusion

As discussed previously, there are advantages to using multiple spacecraft. Compared with the single-occulter case, only half the Delta-V is needed to obtain the same scientific achievement, which means that the occulters can carry roughly half the fuel on board. In the case of the continuous thruster, the thruster system can also be scaled down. For solar-powered thrusters, the size of the solar panel for each spacecraft can be reduced by one fourth. Also, the cost of a spacecraft is markedly lower when it is mass produced than when it is a unique unit. Finally, the redundancy in the system design is a good risk management strategy against the loss of the whole mission in case of a failure in one of the occulters. Given these advantages, the option of using multiple occulters must be studied thoroughly when possible mission designs for an occulter-based telescopy mission are considered.

Chapter 7

Conclusion

A methodology to find the optimal configuration of satellite formations consisting of a telescope and multiple occulters around Sun-Earth L2 Halo orbits was outlined. The dynamics around L2 was examined with a focus on the Quasi-Halo orbits which are of interest for occulter placement. A new fully numerical method which employs multiple Poincaré sections to find quasi-periodic orbits around L2 was developed. Trajectory optimization of the occulter motion between imaging sessions of different stars was performed. The global optimization problem was solved for missions consisting of a telescope and a single occulter employing heuristic methods. Then, these results are extended to perform the global optimization for the multiple-occulter formation. This dissertation introduced a baseline optimal mission design for the occulter-based imaging mission, and enables a trade-off study comparing different occulter-based approaches with one another as well as with their alternatives.

Bibliography

[1] http://planetquest.jpl.nasa.gov/TPF/tpf_index.cfm, 2008. TPF website.

[2] Robert J. Vanderbei, David N. Spergel, and N. Jeremy Kasdin. Circularly symmetric apodization via starshaped masks. *Astrophysical Journal*, 599:686, 2003.

[3] Robert J. Vanderbei, David N. Spergel, and N. Jeremy Kasdin. Spiderweb masks for high-contrast imaging. *Astrophysical Journal*, 590:593, 2003.

[4] D. G. Koch, W. Borucki, E. Dunham, J. Geary, R. Gilliland, J. Jenkins, D. Latham, E. Bachtell, D. Berry, W. Deininger, R. Duren, T. N. Gautier, L. Gillis, D. Mayer, C. D. Miller, D. Shafer, C. K. Sobeck, C. Stewart, and M. Weiss. Overview and status of the Kepler Mission. In J. C. Mather, editor, *Optical, Infrared, and Millimeter Space Telescopes. Edited by Mather, John C. Proceedings of the SPIE, Volume 5487, pp. 1491-1500 (2004).*, volume 5487 of *Presented at the Society of Photo-Optical Instrumentation Engineers (SPIE) Conference*, pages 1491–1500, October 2004.

[5] R. Goullioud, J. H. Catanzarite, F. G. Dekens, M. Shao, and J. C. Marr, IV. Overview of the SIM PlanetQuest Light (SIM-Lite) mission concept. *ArXiv e-prints*, 807, July 2008.

[6] http://www.kepler.arc.nasa.gov/PageMill_Resources/Disc_sp.gif, 2007. NASA Kepler Mission Website.

[7] M. Mayor and D. Queloz. A Jupiter-Mass Companion to a Solar-Type Star. *Nature*, 378:355–+, November 1995.

[8] N. J. Woolf, P. S. Smith, W. A. Traub, and K. W. Jucks. The Spectrum of Earthshine: A Pale Blue Dot Observed from the Ground. *Astrophysical Journal*, 574:430–433, Jul 2002.

[9] W. Cash, J. Kasdin, S. Seager, and J. Arenberg. Direct studies of exo-planets with the New Worlds Observer. In H. A. MacEwen, editor, *UV/Optical/IR Space Telescopes: Innovative Technologies and Concepts II. Edited by MacEwen, Howard A. Proceedings of the SPIE, Volume 5899, pp. 274-285 (2005).*, volume 5899 of *Presented at the Society of Photo-Optical Instrumentation Engineers (SPIE) Conference*, pages 274–285, August 2005.

[10] W. Cash, E. Schindhelm, J. Arenberg, R. Polidan, S. Kilston, and C. Noecker. The New Worlds Observer: using occulters to directly observe planets. In *Space Telescopes and Instrumentation I: Optical, Infrared, and Millimeter. Edited by Mather, John C.; MacEwen, Howard A.; de Graauw, Mattheus W. M.. Proceedings of the SPIE, Volume 6265, pp. 62651V (2006).*, volume 6265 of *Presented at the Society of Photo-Optical Instrumentation Engineers (SPIE) Conference*, Jul 2006.

[11] D. J. Des Marais, M. O. Harwit, K. W. Jucks, J. F. Kasting, D. N. C. Lin, J. I. Lunine, J. Schneider, S. Seager, W. A. Traub, and N. J. Woolf. Remote Sensing of Planetary Properties and Biosignatures on Extrasolar Terrestrial Planets. *Astrobiology*, 2:153–181, June 2002.

[12] Bernard Lyot. La couronne solaire étudiée en dehors des éclipses. *C. R. Hebd. Seances Acad. Sci.*, 191:834–837, 1930.

[13] http://planetquest.jpl.nasa.gov/TPF/tpf_index.cfm, 2008. NASA Terrestrial Planet Finder Website.

[14] A. Give'on, N. J. Kasdin, R. J. Vanderbei, and Y. Avitzour. High-frequency folding and optimal phase conjugation for high-contrast adaptive optics. In D. Bonaccini Calia, B. L. Ellerbroek, and R. Ragazzoni, editors, *Advancements in Adaptive Optics. Edited by Domenico B. Calia, Brent L. Ellerbroek, and Roberto Ragazzoni. Proceedings of the SPIE, Volume 5490, pp. 1438-1449 (2004).*, volume 5490 of *Presented at the Society of Photo-Optical Instrumentation Engineers (SPIE) Conference*, pages 1438–1449, October 2004.

[15] L. Pueyo and J. Kasdin. Performance Study Of Integrated Coronograph-adaptive Optics Designs. In *Bulletin of the American Astronomical Society*, volume 38 of *Bulletin of the American Astronomical Society*, pages 788–+, December 2007.

[16] W. Cash. Detection of earth-like planets around nearby stars using a petal shaped occulter. *Nature*, (442):51–53, July 2006.

[17] R.W. Farquhar. A Halo–Orbit Lunar Station. *Astronautics and Aeronautics*, 10(6):59–63, 1972.

[18] R.W. Farquhar, D.P. Muhonen, C. Newman, and H. Heuberger. The First Libration Point Satellite. Mission Overview and Flight History. In *AAS/AIAA Astrodynamics Specialist Conference*, 1979.

[19] R.W. Farquhar and D.W. Dunham. Libration–Point Staging Concepts for Earth–Mars Transportation. Technical Report M002, NASA, 1986.

[20] R.W. Farquhar and D.W. Dunham. Use of Libration–Point Orbits for Space Observatories. In *Observatories in Earth Orbits and Beyond, Ed by Y. Kondo, Kluwer Academic Publishers*, pages 391–395, 1990.

[21] R.B. Bate, D.D. Mueller, and J.E. White. *Fundamentals of Astrodynamics*. Dover Publications, 1971.

[22] R.H. Battin. *An Introduction to the Mathematics and Methods of Astrodynamics*. AIAA Education Series, 1987.

[23] H. Goldstein, C. Poole, and J. Safko. *Classical Mechanics*. Addison Wesley, 3 edition, 2001.

[24] V. Szebehely. *Theory of Orbits: The Restricted Problem of the Three Bodies*. Academic Press, New York, 1967.

[25] G. Gómez, W. S. Koon, M. W. Lo, J. E. Marsden, J. Masdemont, and S. D. Ross. Connecting orbits and invariant manifolds in the spatial restricted three-body problem. *Nonlinearity*, 17:1571–1606, September 2004.

[26] http://upload.wikimedia.org/wikipedia/commons/b/b8/Lagrange_very_massive.svg, 2008. Lagrange Point Figure.

[27] D.L. Richardson. Analytical Construction of Periodic Orbits About the Collinear Points. *Celestial Mechanics*, 22(3):241–253, 1980.

[28] W.S. Koon, M.W. Lo, J.E. Marsden, and S.D. Ross. Heteroclinic Connections Between Periodic Orbits and Resonance Transitions in Celestial Mechanics. *Chaos*, 10(2):427–469, 2000.

[29] W. S. Koon, M.W. Lo, J.E. Marsden, and S.D. Ross. The genesis trajectory and heteroclinic connections. *AAS*, 103(3):2327–2343, 1999. AAS 99-451.

[30] J.L. Bell et al. Genesis Trajectory Design. *Advances in the Astronautical Sciences*, 103:1525–1537, 2000.

[31] R.W. Farquhar. Lunar Communications with Libration–Point Satellites. *Journal of Spacecraft and Rockets*, 4(10):1383–1384, 1967.

[32] R.W. Farquhar. Station–Keeping in the Vicinity of Collinear Libration Points with an Application to a Lunar Communications Problem. In *Space Flight Mechanics, Science and Technology Series*, volume 11, pages 519–535. American Astronautical Society, New York, 1967.

[33] R.W. Farquhar. Future Missions for Libration–Point Satellites. *Astronautics & Aeronautics*, 7(5):52–56, 1969.

[34] G. Gómez, J. Llibre, R. Martínez, and C. Simó. *Dynamics and Mission Design Near Libration Point Orbits – Volume 2: Fundamentals: The Case of Triangular Libration Points*. World Scientific, 2000.

[35] À. Jorba and J. Masdemont. Dynamics in the center manifold of the collinear points of the restricted three body problem. *Physica D Nonlinear Phenomena*, 132:189–213, July 1999.

[36] À. Jorba and J.J. Masdemont. Dynamics in the Center Manifold of the Restricted Three–Body Problem. *Physica D*, 132:189–213, 1999.

[37] K.C. Howell. Three Dimensional Periodic Halo Orbits. *Celestial Mechanics*, 32(1):53–72, 1984.

[38] J. R. Cash and M. H. Wright. Implementation issues in solving nonlinear equations for two-point boundary value problems. *Computing*, 55:17–37, 1990.

[39] J. R. Cash and M. H. Wright. A deferred correction method for nonlinear two-point boundary value problems: Implementation and numerical evaluation. *SIAM J. Sci. Stat. Comput.*, 12:971–989, 1991.

[40] U. Ascher, J. Christiansen, and R. D. Russell. Collocation Software for Boundary-Value ODEs. *ACM Trans. Math Software*, 7:209–222, 1981.

[41] U. Ascher, R. M. M. Mattheij, and R. D. Russell. *Numerical Solution of Boundary Value Problems for Ordinary Differential Equations*. Prentice-Hall, Englewood Cliffs, NJ, 1988.

[42] Jacek Kierzenka and Lawrence F. Shampine. A bvp solver based on residual control and the maltab pse. *ACM Trans. Math. Softw.*, 27(3):299–316, 2001.

[43] Milton Abramowitz and Irene A. Stegun. *Handbook of Mathematical Functions with Formulas, Graphs, and Mathematical Tables*. Dover, New York, ninth dover printing, tenth gpo printing edition, 1964.

[44] J. Guckenheimer and P. Holmes. *Nonlinear Oscillations, Dynamical Systems, and Bifurcations of Vector Fields*. Springer-Verlag, New York, 1983.

[45] E. T. Campbell. *Bifurcations from Families of Periodic Solutions in the Circular Restricted Problem with Application to Trajectory Design*. PhD thesis, Purdue University, August 1999.

[46] G. Gómez, J.J. Masdemont, and C. Simó. Quasihalo Orbits Associated with Libration Points. *Journal of The Astronautical Sciences*, 46(2):1–42, 1999.

[47] À. Jorba and J. Villanueva. Numerical Computation of Normal Forms Around Some Periodic Orbits of the Restricted Three Body Problem. *Physica D*, 114:197–229, 1998.

[48] R. M. M. Mattheij and G. W. M. Staarink. An efficient algorithm for solving general linear two-point bvp. *SIAM J. Sci. Stat. Comp.*, 5:87–14, 1984.

[49] E. Kolemen, N. J. Kasdin, and P. Gurfil. Quasi-Periodic Orbits of the Restricted Three-Body Problem Made Easy. In *New Trends in Astrodynamics and Applications III*, volume 886 of *American Institute of Physics Conference Series*, pages 68–77, Feb 2007.

[50] I. G. Kevrekidis, R. Aris, L. D. Schmidt, and S. Pelikan. Numerical computations of invariant circles of maps. *Physica D*, 16:243–251, 1985.

[51] http://en.wikibooks.org/wiki/Image:Polar_coordinates_integration_region.svg, 2008. Integration in Polar Coordinates Figure.

[52] Marc-Antoine Parseval des Chênes. Mémoire sur les séries et sur l'intgration complète d'une équation aux differences partielle linéaire du second ordre, à coefficiens constans. *Mémoires présentés à lInstitut des Sciences, Lettres et Arts, par divers savans, et lus dans ses assemblées. Sciences, mathmatiques et physiques.*, 1:638–648, 1806.

[53] J. R. Dormand and P. J. Prince. High order embedded runge-kutta formulae. *J. Comp. Appl. Math.*, 7(1):67–75, 1981.

[54] C. Runge. Über empirische funktionen und die interpolation zwischen äquidistanten ordinaten. *Zeitschrift für Mathematik und Physik*, 46:224–243, 1901.

[55] G. Gómez and J. M. Mondelo. The dynamics around the collinear equilibrium points of the rtbp. *Physica D*, 157(4):283–321, October 2001.

[56] J. M. Mondelo. *Contribution to the Study of Fourier Methods for Quasi-Periodic Functions and the Vicinity of the Collinear Libration Points*. PhD thesis, Universitat de Barcelona, Departament de Matemàtica Aplicada i Anàlisi, 2001.

[57] E.M. Standish. Jpl planetary and lunar ephemerides, de405/le405. *JPL IOM*, 312.F-98-048, 1998.

[58] E.M. Standish Jr. Orientation of the jpl ephemerides, de200/le200, to the dynamical equinox of j 2000. *Astron. Astrophys.*, 114:297–302, 1982.

[59] http://sco.stsci.edu/roses/index.php, 2007. Top 100 TPF-C Targets.

[60] M. A. C. Perryman, L. Lindegren, J. Kovalevsky, E. Hoeg, U. Bastian, P. L. Bernacca, M. Crézé, F. Donati, M. Grenon, F. van Leeuwen, H. van der Marel, F. Mignard, C. A. Murray, R. S. Le Poole, H. Schrijver, C. Turon, F. Arenou, M. Froeschlé, and C. S. Petersen. The HIPPARCOS Catalogue. *Astronomy and Astrophysics*, 323:L49–L52, July 1997.

[61] G. H. Kaplan, J. A. Hughes, P. K. Seidelmann, C. A. Smith, and B. D. Yallop. Mean and apparent place computations in the new IAU system. III - Apparent, topocentric, and astrometric places of planets and stars. *Astronomical Journal*, 97:1197–1210, April 1989.

[62] R. F. Stengel. *Optimal Control and Estimation*. Dover, New York, 1994.

[63] A. E. Bryson and Y. C. Ho. *Applied Optimal Control*. Hemisphere Publishing Corp., New York, 1975.

[64] J. T. Betts. *Practical Methods for Optimal Control using Nonlinear Programming*. SIAM, Philadelphia, 2001.

[65] Margaret H. Wright Philip E. Gill, Walter Murray. *Practical Optimization*. Academic Press, 1982.

[66] A. Wächter and L. T. Biegler. Line search filter methods for nonlinear programming: Motivation and global convergence. *SIAM Journal on Optimization*, 16(1):1–31, 2005.

[67] http://www.mathworks.com/support/tech-notes/1600/1605.html, 2008. Online manual for MATLAB's mex function.

[68] Donald E. Kirk. *Optimal Control Theory: An Introduction*. Prentice-Hall, Englewood Cliffs, NJ, 1970.

[69] Paul Leopardi. A partition of the unit sphere into regions of equal area and small diameter. *Electronic Transactions on Numerical Analysis*, 25:309–327, 2006.

[70] C. E. Miller, A. W. Tucker, and R. A. Zemlin. Integer programming formulation of traveling salesman problems. *Journal of the ACM*, 7(4):326–329, Oct 1960.

[71] http://www.tsp.gatech.edu/concorde.html, 2008. Concorde TSP Solver.

[72] G. Gutin and A. P. Punnen, editors. *Travelling Salesman Problem and Its Variations*, volume 12 of *Combinatorial Optimization*. Kluwer Academic Publishers, New York, 2002.

[73] F. Glover and M. Laguna. *Tabu Search*. Kluwer Academic Publishers, Norwell, MA, 1997.

[74] Marco Dorigo and Luca Maria Gambardella. Ant colony system: A cooperative learning approach to the traveling salesman problem. *IEEE Transactions on Evolutionary Computation*, 1:53–66, 1997.

[75] P. T. De Boer, D. P. Kroese, S. Mannor, and R. Y. Rubinstein. A tutorial on the cross-entropy method. *Annals of Operations Research*, 134, 2004.

[76] S. Kirkpatrick, C. D. Gelatt, and M. P. Vecchi. Optimization by simulated annealing. *Science*, 220(4598):671–680, May 1983.

[77] http://upload.wikimedia.org/wikipedia/commons/8/85/Rundtur.GIF, 2008. 2-opt procedure.

[78] http://www.esa.int/SPECIALS/SMART-1, 2008. The official SMART-1 website.

[79] I. Jordan, H. Hart, A. Schultz, G. Starkman, C. Copi, and R. Lyon. The advantages of multiple coronagraphic vehicles in occulter missions. In *Space 2003 Conference Proc.*, Sep 2003. AIAA-2003-6300, ISBN 1-56347-647-9.

[80] Azuka Chikwendu. Optimization of multiple occulter mission in quasi-halo orbit. Princeton University, Undergraduate Thesis, 2007.